ABSTRACT

Title of Dissertation:	DEEP LEARNING-REINFORCED ENGINEERING OF ISLETS WITH MICRO AND NANO BIOMATERIALS FOR TYPE 1 DIABETES TREATMENT Alisa Melody White, Doctor of Philosophy, 2023
Dissertation directed by:	Professor Dr. Xiaoming He, Fischell Department of Bioengineering

An estimated 1.6 million Americans live with type 1 diabetes (**T1D**). The most common treatment method involves daily blood glucose monitoring and insulin injections, which can negatively impact quality of life and lead to severe health complications. Whole pancreatic transplantation, a more permanent treatment option, entails invasive surgery with associated risks and a high morbidity rate. Furthermore, lifelong immunosuppressant use, which can be detrimental to health, is necessary for transplant recipients. Islet transplantation has emerged as a promising alternative for T1D treatment, offering a less invasive approach, though it still requires the use of immunosuppressants to prevent graft rejection. Encapsulation of islets in biomaterials has shown potential for mitigating immune responses post-transplantation while facilitating islet survival and insulin production. However, despite its promise, this

method faces several challenges. First, a significant issue is the generation of numerous empty microcapsules during islet encapsulation, which requires an efficient method for their removal due to the limited space for the transplanted islets in patients. Second, microcapsules are typically suspended in an oil phase after generation with microfluidic devices, whereas they must be transferred into an aqueous solution for further culture or transplantation, posing technical difficulties. Third, conventional microcapsules do not provide a tissue-like environment for islets which is detrimental to islet health, and microcapsule design flaws can result in a lack of insulin production and islet cell death due to post-transplantation immune response. Furthermore, islets experience hypoxia and increased amounts of reactive oxygen species post-isolation and transplantation, resulting in islet death. This work focuses on addressing the challenges mentioned above by enhancing islet encapsulation methods through a deep learning-based on-chip detection and sorting system, enabling the creation of highly pure samples of islet-laden core-shell hydrogel microcapsules that mimic the structure and microenvironment of the pancreas. We also investigate the use of nanoparticles to encapsulate hydrophobic antioxidants for improving their delivery into islet cells to enhance islet viability after isolation and hypoxic stress. We address critical challenges in islet transplantation by investigating deep learning-enabled selective extraction, core-shell hydrogel microencapsulation, and nanoparticle-mediated antioxidant delivery. This novel multiscale biomaterials-engineering strategy has great potential for future clinical translation, contributing to the advancement of type 1 diabetes treatment.

DEEP LEARNING-REINFORCED ENGINEERING OF ISLETS WITH MICRO AND NANO BIOMATERIALS FOR TYPE 1 DIABETES TREATMENT

by

Alisa Melody White

Dissertation submitted to the Faculty of the Graduate School of the
University of Maryland, College Park, in partial fulfillment
of the requirements for the degree of
Doctor of Philosophy
2023

Advisory Committee:
Professor Xiaoming He, Chair
Professor Jonathan S. Bromberg
Associate Professor Huang Chiao Huang
Professor Yang Tao
Professor Shaik Rahaman

Dedication

To my mother, Myra Lynn Austin

Acknowledgements

First, I would like to thank my advisor, Professor Xiaoming He, for his mentorship and all the opportunities and guidance he has provided me over these years.

I want to thank all the current and former members of the Multiscale Biomaterials and Engineering Laboratory for their help and support. I would specifically like to thank Dr. Yuntian Zhang, Dr. Wenquan Ou, Dr. Jiangsheng Xu, and Dr. Elyahb Allie Kwizera for their guidance and for giving me so much invaluable knowledge.

I want to thank the members of my proposal and dissertation committees, Dr. Jonathan Bromberg, Dr. Huang Chiao Huang, Dr. John Fisher, Dr. Yang Tao, and Dr. Shaik Rahaman, for their help and advice.

Finally, I would like to thank my family and friends for all their unwavering support. I could have never completed this work without you.

I also must give special acknowledgment to my mother, Cynthia White, for believing in me and encouraging me at every step.

Table of Contents

List of Tables

List of Figures

Statement of Contributions

This dissertation is the cumulative doctoral research of the present author and collaborators performed in the University of Maryland's Multiscale Biomaterials Engineering Laboratory under the guidance of the principal investigator, Professor Xiaoming He. Professor He contributed to the present author's work through conception of ideas, design and troubleshooting of experiments, review of figures, analysis and interpretation of data, editing of draft manuscripts, and finalization of manuscripts. Below is a statement of contributions from the author and other collaborators.

Chapter 1: This chapter is an introduction written by the present author.

Chapter 2: This chapter was reprinted (adapted) with permission from: White, A. M., James G. Shamul, Jiangsheng Xu, Samantha Stewart, Jonathan S. Bromberg, and Xiaoming He. "Engineering Strategies to Improve Islet Transplantation for Type 1 Diabetes Therapy". ACS Biomaterials Science & Engineering 2020; 6: 2543-2562. Copyright 2020. ACS Biomaterials Science & Engineering. The present author created all the figures and wrote and edited the draft manuscript with inputs from all other co-authors.

Chapter 3: This chapter was reprinted (adapted) with permission from: White, A. M.*, Zhang, Y.*, Shamul, J.G., Xu, J., Kwizera, E.A., Jiang, B., and He, X. "Deep learning-enabled label-free on-chip detection and selective extraction of cell aggregate-laden

hydrogel microcapsules". Small 2021; 2100491. Copyright 2021. Small (equal contribution*). Dr. Yuntian Zhang wrote the codes for image processing, model training, and the microcontroller. Dr. Zhang made the experimental setup schematic in Figure 3.1B. Dr. Zhang quantified the image acquisition speed of the cell phone camera and performed the speed comparison studies between backend structures in Figure 3.3B and Figure 3.3C, respectively. The present author performed all other experiments and created all other figures. Dr. Zhang and the present author contributed to the draft manuscript writing and editing with input from all other co-authors.

Chapter 4: Dr. Wenquan Ou assisted with IVIS imaging in Figure 4.6C and animal work performed in Figure 4.7. Dr. Ou assisted with staining and flow cytometry studies in Figure 4.7F and Figure 4.7G. Dr. Vikas Saxena provided islet isolation training in Professor Jonathan Bromberg's lab. The present author performed all experiments, created all figures, and wrote and edited the draft chapter with input from Dr. Ou's and Ms. Samantha Stewart's.

Chapter 5: Samantha Kraus fabricated and characterized bilirubin nanoparticles and cultured cells contributing to data collected for Figure 5.1, Figure 5.2, and Table 5.1. Wenquan Ou took the TEM images in Figure 5.1B. Ana Fisk fabricated bilirubin and curcumin nanoparticles and contributed data collected for Table 5.2 and Figure 5.3. Dr. Vikas Saxena provided islet isolation training in Professor Jonathan Bromberg's lab. The present author performed all other experiments, created all figures, and wrote and edited the draft chapter.

Chapters 6 and 7: The preset author wrote and edited these chapters on conclusions and future directions.

This research is supported by the National Institute of Health (**NIH**) grant (R01EB023632) through the National Institute of Biomedical Imaging and Bioengineering (**NIBIB**) and the NIH Fellowship grant (F31DK131905) through the National Institute of Diabetes and Digestive and Kidney Diseases (**NIDDK**).

Chapter 1 : Introduction

Over 1.6 million Americans are estimated to have type 1 diabetes (**T1D**) [1,2]. T1D is a chronic autoimmune disorder in which the immune system attacks insulin-producing beta cells located in pancreatic islets[3]. The most widely used method for T1D treatment requires blood glucose level monitoring and periodic insulin injections[4]. However, patient insulin levels can fluctuate significantly with this approach, which may cause hyperglycemia that can result in organ damage. This is worsened by poor patient compliance with periodic insulin injections[5,6].

Whole pancreatic transplantation is a more permanent alternative method but requires a major surgical procedure, and patients must be placed on immunosuppressants for the rest of their lives, which can be highly detrimental to health by increasing risk of infection and potential malignant diseases[7,8]. This procedure has also been shown to have surgical complications leading to increased morbidity compared with other treatment methods[9]. More recently, pancreatic islet transplantation has been explored as an attractive option for the treatment of T1D, due to the potential of glucose-responsive insulin release without the need for insulin injection for months or years[5,6]. However, immunosuppressant treatment is still required to prevent immune rejection of the transplanted exogenous islets. Encapsulating islets in alginate hydrogel microcapsules before implantation may mitigate damage to islets by the host immune response[10-13].

Current methods for islet microencapsulation almost always produce many empty microcapsules without an islet. Due to the limited space available for housing

the transplants in vivo, a sample of highly pure islet-laden hydrogel microcapsules is desired[14,15]. Since the islets should be transplanted without any labeling, manual separation of the cell-laden microcapsules from the empty ones has been done in the past. In addition, islet-laden microcapsules produced using microfluidics are suspended in an oil-based solution which can be detrimental for cell health[16,17]. This lengthy manual procedure of removing empty microcapsules and oil may compromise the survival of islets in the microcapsules before implantation in vivo. Contemporary islet microencapsulation methods also still result in post-transplantation immune response, immune cell infiltration, and fibrosis, leading to cell death and decreased insulin secretion[18-20]. This can be caused by improper islet encapsulation and islets protruding from microcapsules[11]. Finally, post-transplantation hypoxia can result in the death of up to 70% of islets[21,22].

The **objective** of this thesis work is to address the aforementioned major challenges to islet transplantation by developing efficient methods to obtain high purity samples of islet-laden core-shell hydrogel microcapsules with low immunogenicity, and to minimize hypoxia-induced damage to islets for treating T1D via sustained glucose-responsive release of insulin. This was investigated through microfluidic encapsulation and deep learning-based label-free on-chip selective extraction of islet-laden core-shell hydrogel microcapsules and nanoparticle-mediated delivery of antioxidants to improve islet viability post-transplantation.

We **hypothesized** that the deep learning-based label-free detection and dielectrophoresis (**DEP**)-based selective extraction can be used to sort cell aggregate/tissue-laden microcapsules out of empty ones, which can then be applied to

efficiently produce high purity islet-laden core-shell hydrogel microcapsules samples. Furthermore, we **hypothesized** that core-shell hydrogel microcapsules fabricated using a non-planar microfluidic device can improve transplantation outcomes in a syngenetic diabetic mouse model compared to conventional alginate microcapsules. We also **hypothesized** that nanoparticles can enhance uptake of hydrophobic nanoparticles into islets, leading to improved islet viability after isolation and hypoxic incubation.

This dissertation consists of a total of seven chapters. **Chapter 1** serves as an introduction and offers a summary of the research. **Chapter 2** provides background information on islet transplantation and insights into the field's current state.

Chapter 3 explores the development of an on-chip, label-free, deep learning-based selective extraction method for creating a highly pure sample of cell aggregate-laden homogeneous alginate microcapsules. Different deep learning structures are tested, and the optimal system for extraction is determined. The deep-learned model is trained using images of cell aggregate-laden and empty microcapsules, resulting in a system with real-time highly efficient sorting of aggregate-laden microcapsules from empty microcapsules and a highly pure microcapsule sample. A schematic illustration of the system can be seen in **Figure 1.1A**.

In **Chapter 4,** a non-planar microfluidic device that fabricates core-shell hydrogel microcapsules with label-free deep learning-based sorting is developed and optimized. Islets encapsulated in core-shell hydrogel microcapsules are evaluated in vitro for viability and glucose-responsive insulin production and in vivo using a diabetic mouse model, comparing them to conventional homogeneous alginate

microcapsules. A schematic illustration of the process of islet isolation, encapsulation, and syngeneic transplantation in a diabetic mouse model can be seen in **Figure 1.1B**.

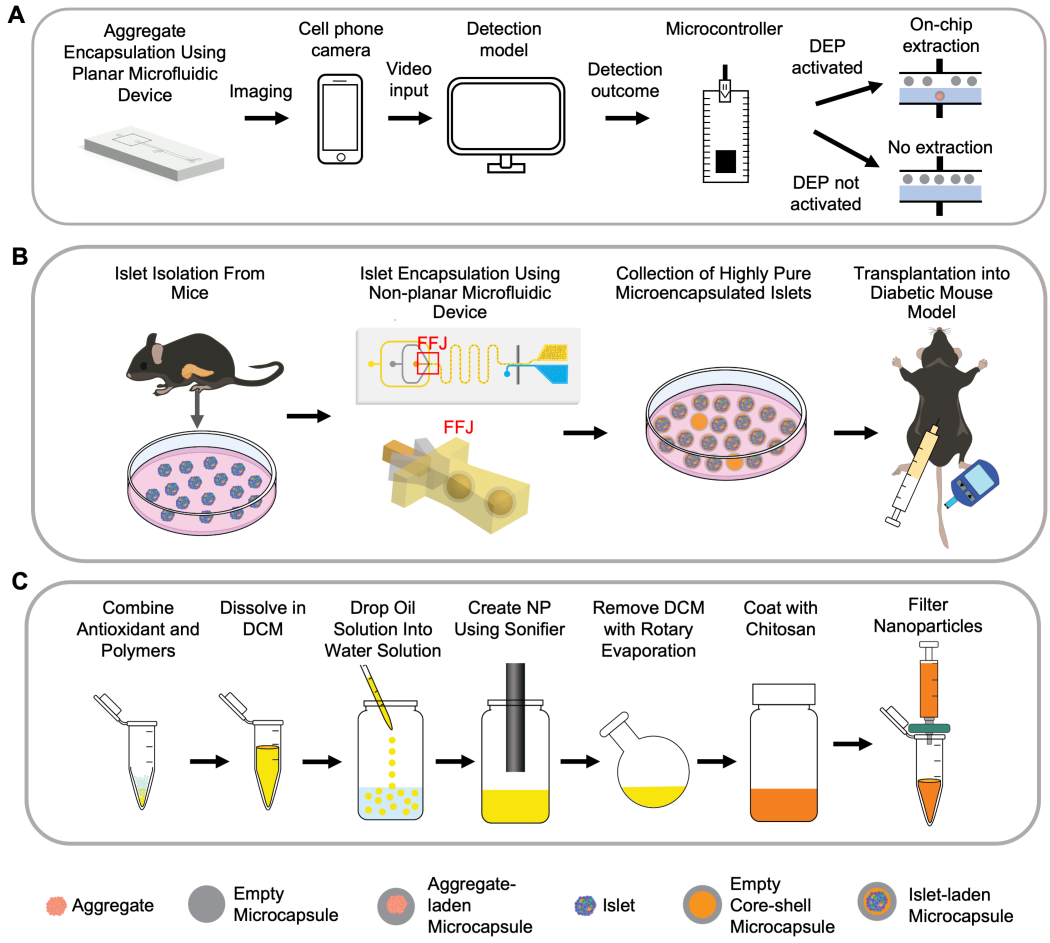

Figure 1.1. Schematic Illustrations of the Research Performed in Chapters 3 to 5. (**A**) Schematic illustration of deep learning-based system for on-chip extraction of aggregate-laden microcapsules. Aggerates are encapsulated in a homogeneous alginate microcapsule using a planar microfluidic device. The detection region is then imaged using a cell phone camera, which reads into the computer where the deep learning model is running. The model determines if the microcapsule in the detection region contains an aggregate and then sends that information to the microcontroller, turning on the switch if there is an aggregate preset in the microcapsule or staying off if there is no aggregate present. Adapted from White et al.[17] (**B**) Schematic illustration of islet encapsulation in core-shell hydrogel microcapsules using a non-planar microfluidic device, followed by transplantation into a diabetic mouse model. Islets are first isolated from C57BL/6 mice and encapsulated using a non-planar microfluidic device. Microcapsules are formed at the flow focusing junction (**FFJ**) of the device and are then sorted on-chip using the deep learning detection system in **A**. Islets are then transplanted into the intraperitoneal cavity of diabetic C57BL/6 mice using a syringe

and a needle, and mouse blood glucose levels are monitored over time. (**C**) Schematic illustration of antioxidant nanoparticle synthesis using a single emulsion method and chitosan coating. First, antioxidants and polymers are combined and dissolved in dichloromethane (**DCM**). They are then dropped into an aqueous-based polyvinyl alcohol solution and emulsified using a sonifier. DCM is removed through rotary evaporation, and nanoparticles are coated overnight with a chitosan solution and filtered.

Chapter 5 examines the development of antioxidant-laden nanoparticles to increase hydrophobic antioxidant uptake and protect islet viability after isolation and hypoxic incubation. Poly(lactic-co-glycolic acid) (**PLGA**), Pluronic F-127 (**PF-127**), and chitosan are used to synthesize antioxidant-laden nanoparticles. These nanoparticles are optimized and characterized for size, charge, and antioxidant release over time. Uptake into cells and islets, as well as protective effects on islets after hypoxia, are quantified. A schematic illustration of nanoparticle synthesis can be seen in **Figure 1.1C**.

Chapter 6 provides conclusions for the research in this dissertation, and **Chapter 7** discusses potential avenues for future studies.

Chapter 2 : Background*

2.1 Overview

Type 1 diabetes mellitus affects over 1.6 million Americans and 20 million people worldwide[1,2]. Type 1 diabetes is an autoimmune disorder where the body's adaptive immune system attacks insulin-producing beta cells located in pancreatic islets[3]. T cells eventually kill a large percentage of the body's beta cells, which means that blood glucose levels will fall outside of healthy ranges without medical intervention. The most common type 1 diabetes treatment method today is monitoring of blood glucose followed by insulin injections when levels are too high. However, insulin injections are time-consuming and patient compliance can waver, which can cause potentially fatal hypoglycemic peaks. Years of hyperglycemia due to lack of insulin can lead to organ damage[5]. Pancreatic transplantation is another treatment method, but it requires a major surgical procedure, and the patient must then be placed on immunosuppressant drugs for the rest of their lives to prevent organ rejection, which is detrimental to health[7]. Transplantation of pancreatic islets is another method that has been widely studied in recent years. This method is less invasive, has shown promising results in animals and clinical trials, and can lead to a great improvement in quality of life for type 1 diabetes patients. Unfortunately, immunosuppressants are still necessary to prevent rejection of islets if they are non-autologous or not engineered with immune protection. In addition, a fibrous capsule may form around nonprotected islets without

* Reprinted (adapted) with permission from White, A. M., James G. Shamul, Jiangsheng Xu, Samantha Stewart, Jonathan S. Bromberg, and Xiaoming He. "Engineering Strategies to Improve Islet Transplantation for Type 1 Diabetes Therapy". ACS Biomaterials Science & Engineering 2020; 6: 2543-2562. Copyright 2020. American Chemical Society.

immunosuppressants, keeping insulin from being secreted and nutrients from being absorbed[23]. The need for immunosuppressive drugs can be eliminated by encapsulating islets in biocompatible materials. These biocompatible materials allow small molecules like insulin to diffuse out of the islets and oxygen and nutrients to diffuse in but block larger immune cells and antibodies from entering[24,25]. Islets are sourced from deceased donors, so a high yield of viable islets after transplantation is essential. Problems still facing encapsulated islet survival include immune rejection, death due to lack of nutrients, and death due to post-transplantation hypoxia. Survival after transplantation can be increased by improving the encapsulation technologies.

2.2 Diabetes background

Islets are clusters of cells located in the pancreas that are responsible for endocrine functions. These clusters contain multiple cell types including alpha cells, beta cells, delta cells, epsilon cells, pancreatic polypeptide (**PP**) cells, and a capillary network[26]. Alpha cells are responsible for releasing glucagon when blood sugar levels are too low. Beta cells are responsible for secreting insulin when blood glucose levels are too high. Epsilon cells produce ghrelin, which causes hunger, and PP cells secrete somatostatin which regulates alpha and beta cells[27]. Islets are located throughout the pancreas and vary in shape, size, and density[28]. Each person has about one million islets in their pancreas. The pancreas also contains glands with acinar cells and ductal cells, which are responsible for exocrine function. The exocrine tissue in the pancreas is all connected to the pancreatic duct[29].

Type 1 diabetes is an autoimmune disease in which the body's immune system attacks its beta cells, causing deterioration over time until they no longer function[3]. This

disease can start in early childhood and progresses throughout life. Type 2 diabetes is usually acquired later in life and can be the result of both genetic and environmental factors. In type 2 diabetes, beta cells still function well, but other cells no longer accept glucose, resulting in dangerous spikes in blood sugar levels[29]. People administer insulin in various ways to reduce their blood glucose levels. Standard treatment methods for diabetes consist of constant blood glucose level monitoring accompanied by insulin injections or insulin pumps that need to be constantly worn.

Transplantation for type 1 diabetes treatment is a widely researched area. Transplantation can eliminate the need for the patient to constantly monitor and administer insulin. One method of treating type 1 diabetes is a full pancreatic transplantation from a deceased donor. This is a major surgical procedure, and patients must be put on immunosuppressant drugs for the rest of their lives to avoid immunorejection[23]. These drugs can have extremely detrimental health effects including increased infection susceptibility, organ damage, and even cancer, greatly lowering quality of life. Another transplantation approach involves the use of pancreatic islets. Islets, instead of the entire pancreas, are harvested from donors and transplanted into patients to regulate the body's glucose levels. Since insulin-producing cells represent only 2− 3% of the cells in the pancreas, it is appealing to only transplant the necessary tissue (e.g., islets) containing the insulin producing cells[30]. This method is also much less invasive than whole pancreas transplantation because islets are implanted into the liver through the portal vein[23]. Studies have shown that for encapsulated islet transplantation, approximately 10,000 islet equivalents (**IEQ**, an islet with equal mass to the average islet of 150 μm in diameter) per kilogram of body weight

are required in order to provide sufficient insulin dose[31]. Patients that receive an islet transplantation must still be put on immunosuppression so that the implanted islets are not rejected. Although whole pancreas transplantation has a higher overall success rate for long-term euglycemia, it is also associated with a higher morbidity rate than islet transplantations[9].

Encapsulating islets in a biocompatible material can overcome the possible immunogenicity of the tissue, potentially eliminating the need for patients to take immunosuppressants and improving their overall quality of life. Due to the lower surgical and post-surgical risks of islet transplantation, the potential for increased islet survival, and long-term insulin production through improvements in encapsulation technologies, transplantation of encapsulated islets has recently become an appealing area of study.

2.3 Graft transplantation

There are various types of tissue grafts used in transplantation for diabetes treatment: allografts, autografts, and xenografts. Allografts involve transplantation from the same species and are the most common type of pancreatic transplantations[32]. Autografts involve regrafting tissue from the same person[33]. In the context of islet transplantation, this involves removing the pancreas, digesting the exocrine tissue to remove the islets, and reimplanting encapsulated islets to prevent further damage by the immune system. Xenograft transplantation involves transplanting tissue from one species into another. Autograft transplantations will have a minimal immune response but involve organ removal, which can add surgical complication[10]. Since allograft transplantation is between the same species, the immune response will be less pervasive

than xenotransplantation but worse than using autografts. Xenograft transplantation will have the largest immune response but, in the case of islet transplantation means an increased number of islets available for transplantation.

The most popular xenograft used in clinical trials is isolated porcine islets. Xenotransplantation of porcine islets is a popular area of research as there are a limited number of human islet donors available[34]. Pig insulin is very similar to human insulin, differing only by one amino acid, which makes pigs a very appealing islet source. Although xenograft transplantation raises concerns about immunorejection, pig islets can be encapsulated in a biocompatible material to isolate them from the host immune system and avoid rejection[35]. There has been some concern that transplanting islets from pigs into humans would cause the transfer of retroviruses, but studies have shown successful islet transplantation with high amounts of insulin release and no sign of virus transmission[36]. In vivo porcine xenotransplants have been shown to result in sustained patient normoglycemia in clinical trials as well[37,38].

2.4 Clinical trials

Clinical trials on whole pancreas transplantation were first reported in the 1960s[39], but with high morbidity and mortality rates[40]. Eventually, these outcomes improved, especially when simultaneous pancreas and kidney (**SPK**) transplantation was performed in uremic diabetic patients[41]. The first islet transplantation was performed in 1974[42], but this procedure did not produce successful outcomes until the Edmonton protocol for islet isolation was developed[7,43]. Since then, there have been two major transplantation types for diabetes treatments, whole pancreas and islet-only, which have greatly improved outcomes over recent years. Whole pancreas

transplantation helps patients to become insulin-independent but often results in complications leading to morbidity and even mortality[44]. Islet-only transplantation, on the other hand, involves a much less invasive procedure and rarely results in morbidity or mortality but has not consistently maintained insulin-independence over a long period of time[41].

One study compared clinical SPK with simultaneous islet and kidney (**SIK**) transplantation and found that post-transplantation groups had over a 90% improvement rate of hypoglycemia[45]. After 5 years, insulin independence in the SPK group was 73.6% and it was 9.3% for the SIK group. The study also concluded that whole pancreas transplantations had significantly more complications. Another study compared clinical transplantation outcomes between pancreas transplantation alone (**PTA**) and islet transplantation alone (**ITA**)[41]. This study found that ITA patients had a 90% insulin independence at 1 year, and 70% insulin independence at 3 years whereas PTA patients had 93% insulin independence at 1 year, and 64% insulin independence at 3 years. Though two islet transplantations were needed for ITA patients, PTA patients had longer hospitalization times and more complications. Although there is still a disparity between long-term insulin independence after whole pancreas transplantation and islet only transplantation, the lower risk of postsurgical complications makes islet transplantation a very appealing area of investigation.

In recent years, due to advances in islet isolation procedures and encapsulation technologies, the outcome of islet transplantation has improved. There are many islet transplantation clinical trials in which patients achieved normoglycemia for extended periods. Placing nonencapsulated islets in the portal vein of the liver is the most

common transplant type examined in clinical trials, but there are many problems with this method. In one study, seven patients with type 1 diabetes were implanted with islets isolated from human donors. Over 15 months of monitoring, patients were able to maintain normoglycemia after a total implantation of ~11,000 IEQs per kilogram body weight[46]. However, since the islets were not encapsulated, the patients also had to take immunosuppressants to prevent tissue rejection. To allow patients to forego immunosuppressants while preventing the rejection of islets, especially when performing xenotransplantation, clinical trials then moved toward using encapsulated islets. In one study, a patient was implanted with a macrodevice consisting of an oxygenated chamber made of alginate and a poly membrane material containing human islets. The patient was able to maintain glucose response for 10 months with no immunosuppression and no indication of graft rejection[31]. This improvement over previous studies may be attributed to increased oxygenation causing increased cell survival.

Xenotransplantation of encapsulated porcine islets has also been explored in multiple clinical trials with varying levels of success. One clinical trial involving a collagen-covered islet encapsulation device resulted in six out of twelve patients being able to decrease their insulin requirements for four years. These devices contained porcine islets combined with Sertoli cells to provide islet protection and were transplanted subcutaneously into patients that were not administered with immunosuppressant drugs[35].

In another long-term study, alginate-encapsulated porcine islets were transplanted into a patient without the use of immunosuppressants. The patient's blood glucose

levels returned to pretransplant amounts after 49 weeks, however, the encapsulated islets were removed and tested after 9.5 years and were still alive, producing small amounts of insulin[38]. The patients in these studies were not administered with immunosuppressive drugs, but insulin production did not persist long enough to be feasible for treatments on a larger scale. In general, encapsulation technologies need to be improved to achieve sustained, long-term insulin release. Several clinical trials involving encapsulated islets are currently in progress but have not achieved consistent responsive insulin production for long enough periods to be a feasible standard of treatment for type 1 diabetes. There is a great deal of ongoing research to improve transplantation methods, specifically in improving the ways the islets are encapsulated. Improved technology for islet transplantation including the work in the proposal will hopefully result in easily implantable encapsulated islets with long-term glucose responsiveness that can treat type 1 diabetes without the need for immunosuppression or insulin supplementation.

2.5 Encapsulation

Various types of biocompatible encapsulation methods have been researched for islets. The encapsulation and transplantation of islets is also known as a bioartificial pancreas (**BAP**)[47]. Both larger encapsulation devices known as macrodevices (**Figure 2.1A**)[48] and smaller encapsulation devices known as microdevices (**Figure 2.1B**) have been designed and studied. In addition, islets have been encapsulated in conformal coatings for their protection (**Figure 2.1C**). The materials with which the devices are made and the way in which they are encapsulated also can contribute to the success of the devices in vivo.

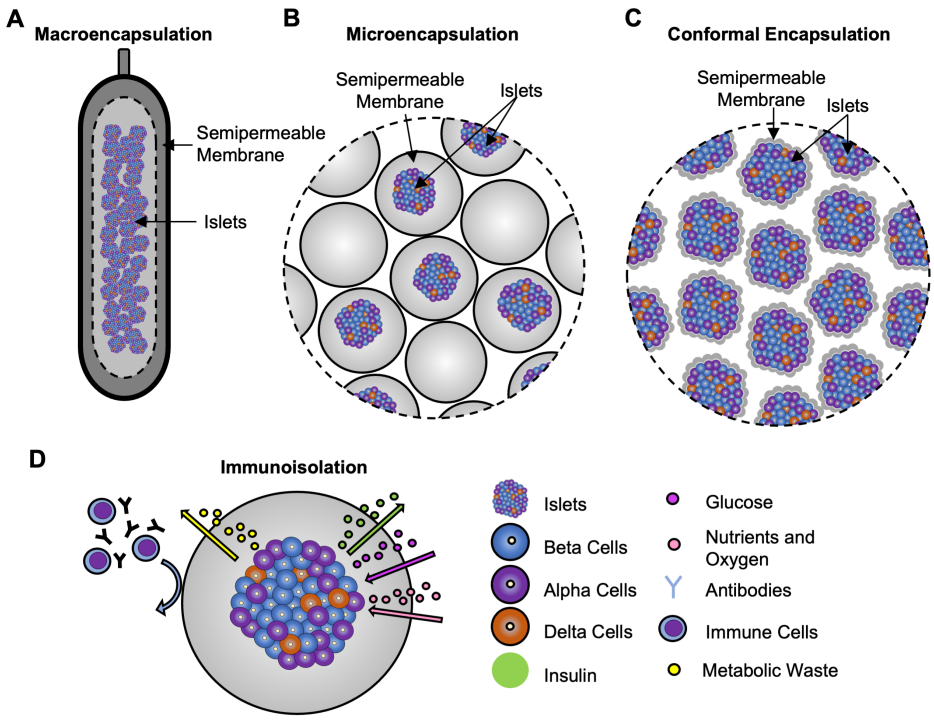

Figure 2.1. Schematic illustration of different types of islet encapsulation. (**A**) Macroencapsulation devices contain a large number of islets and are usually implanted subcutaneously. The TheraCyte device (sketched) is an example of a macroencapsulation device[49]. A few macroencapsulation devices can hold the number of islets necessary for implantation. These devices are on the centimeter scale. (**B**) Microencapsulated islets. Microcapsules are usually between 300 and 1000 μm. Islets are encapsulated in a semipermeable microcapsule, which is most often alginate-based. There are only one to two islets per capsule and 10,000 islets per kg body weight are necessary to maintain normoglycemia (i.e., a large number of microcapsules need to be implanted into the body). (**C**) Conformally coated islets. Islets are encapsulated in a semipermeable coating that is usually less than 50 μm thick. (**D**) Semipermeable membranes in the aforementioned approaches have pores of an optimal submicron size to allow the diffusion of insulin and metabolic waste out of the device, while permitting gas exchange, nutrient intake, and keep out of immune cells and large immune factors (e.g., immunoglobulin G or IgG). Adapted from White et al.[50]

2.5.1. Materials

A great deal of research has been conducted on various materials that can be used to encapsulate islets. The purpose of encapsulating islets is to prevent or minimize immune reaction. The pores of the materials must be an optimal size to allow for

nutrient exchange but prevent elicitation of an immune response (**Figure 2.1D**). Since immune cells have a diameter between ~6 and 10 μm, devices with pores in the submicron range should prevent immune cell infiltration[51]. Organic metabolites have diameters between 0.05 and 1 nm and globular proteins have diameters between 2 and 10 nm, pore sizes should be up to 10 nm to allow for the diffusion of small molecules and macromolecules, such as oxygen, nutrients, and growth factors. Using a maximum pore size of 10 nm also prevents immune cell infiltration into microcapsules[52,53]. Alginate was the first material used for microencapsulation and remains the most popular[54].

Alginate is currently the most commonly used material for islets encapsulation because it can be formulated to be biocompatible and nondegradable with adjustable stiffness and has appropriate pore sizes to prevent immune cell infiltration[19]. The pore sizes of alginate can also be adjusted based on the alginate composition[55,56]. Alginate is a natural biomaterial that is derived from brown seaweed. It is also recognized by the FDA as safe, making it desirable for use[57]. Alginate can form a hydrogel through ionic cross-linking using a divalent cation such as Ca^{2+} and Ba^{2+}. Alginate consists of β-D-mannuronic acid (M) and α-L-guluronic acid (G) as blocks of M, G, or MG[58]. Changing the ratios of these monomers will change the properties of the alginate. It has been found that increasing the number of G blocks causes an increased stiffness because G is responsible for the cross-linking with divalent cations. Purifying alginate has also been shown to decrease immune reaction during islet transplantation, this can be attributed to a higher content of G post-purification, which decreases the amount of microcapsule breakage as well as the removal of toxins or impurities[59]. Some research

has also shown that the block structure of M and G affects binding, which can be useful when tuning stiffnesses of alginate gel for minimizing immune response and determining the appropriate porosity[60]. Barium cross-linking has been shown to create strong gel, but since barium can be toxic, calcium is used more for gelling alginate due to a fear of barium leakage[61,62]. Alginate modification is a popular method of improving various aspects of transplantation[63,64].

In vivo studies have demonstrated the durability of alginate microcapsules without significant degradation up to five years. One study found alginate microcapsules remained intact without rupture and degradation for 90 days after transplantation into the IP cavity of rats[65]. Other studies found that microcapsules remained intact for over 2 months in the IP cavity of canines and a year after transplantation into mice[66-68]. In clinical trials of alginate encapsulated islet transplantation, intact alginate microcapsules were observed in patients over a year after transplantation and over five years post-transplantation[69,70].

The most prevalent methods include gelling through light-based cross-linking, thermally induced cross-linking, and ion-based cross-linking. However, thermal and photo cross-linking methods are disadvantageous, as they might harm the cells. Polyethylene glycol (**PEG**) is another material that is often used for islet encapsulation due to biocompatibility, tunable properties, and gelation ability using cross-linking and photopolymerization[71-75].

Using components found in the ECM in the encapsulation materials has also been shown to improve biocompatibility. Collagen type IV is found in the ECM surrounding islets in the pancreas and has been shown to enhance islet survival[76]. In

one study, human islets were encapsulated in an alginate/collagen IV mixture with laminin sequences of either RGD, LRE, or PDSGR[77]. In vitro co-culture with cytokines showed overall decreases in danger-associated molecular pattern release and decreased apoptotic cell death, indicating protection against toxicity of cytokines. Insulin secretion has also been shown to be affected by the ECM. When islets were encapsulated in PEG gels containing collagen type IV and laminin, islet secretion of insulin increased[78]. ECM from porcine pancreases was used to create microcapsules where porcine pancreases were decellularized and the liquified ECM was collected[79]. The liquified ECM was combined with alginate and microcapsules were created by using a needle and droplet spray and gelling with calcium chloride. In the work of Fukuda et al., a gel scaffold was used to individually coat beta cells with fibronectin and gelatin to mimic the ECM using a layer-by-layer coating technique. The coated cells were then fabricated into spheroids of ∼300 μm in diameter. These dense spheroids had higher insulin release than the control spheroids in vitro, and higher insulin release in vivo[80].

2.5.2. Types of Encapsulation

Macrodevices and microcapsules are the most widely used encapsulation methods in clinical islet transplantation trials. Microdevices fall in the micron to millimeter scale and usually encapsulate one or two islets per device (**Figure 2.1A**). Macrodevices range from millimeters to centimeters in size and can encapsulate thousands of islets per device (**Figure 2.1B**). Conformal encapsulation of islets in a coating layer that is not much thicker than islets themselves are recently being explored to protect islets, leading to increased diffusion (**Figure 2.1C**)[81].

2.5.3 Microencapsulation

Microcapsules are the most researched type of encapsulation for islet transplantation. Islet encapsulation was first described by Lim and Sun where rat islets were placed in an alginate hydrogel, and microcapsules were created using a syringe drop method and gelled using calcium chloride[82]. While this remains the most popular type of microencapsulation, but there have been many improvements in encapsulation methods and materials. Microcapsules contain one to a few islets inside the spherical hydrogel. The microcapsules, usually ranging from over 300 to 1000 μm. The biomaterials used have pores that are large enough to allow small molecule diffusion yet small enough to prevent immune cells from infiltrating, as seen in **Figure 2.1D**. The biomaterials surround the islet to minimize immune response, while still allowing a large surface area of the islets to be exposed with a limited amount of space between the islet and the surrounding tissue, which makes the diffusion of small molecules much faster. Microencapsulation of islets also allows for other material modifications that can aid in cell survival and prevention of immune response. The major drawback of this method is the lack of direct vascularization between the islets and the surrounding tissues, due to the surrounding biomaterial. Islet encapsulation methods are varied but also paramount for successful application. In general, islet-laden hydrogel microcapsule drops are formed then stabilized via gelling. In the first paper describing the microencapsulation of islets, microcapsules were formed using a syringe pump technique[82]. Sodium alginate solution containing islets was pushed through a syringe to form droplets, which were deposited into a calcium chloride solution for gelling. Methods for generating microcapsules have greatly improved since then.

2.5.4. Droplet generation

Droplet generators are most commonly used for creating droplets. There are various types of droplet generation including air shearing, electrostatic droplet formation, and acoustic vibrations[83]. A droplet generator is comprised of a needle or syringe to hold an aqueous solution, a nozzle, and a gelling bath as seen in **Figure 2.2**. The aqueous solution flows out of the nozzle, eventually forming a drop which freely falls after extrusion into a gelling solution (**Figure 2.2A**). These droplets usually range from 100−1000 μm and can contain varying numbers of islets. The nonhomogeneous sizes and islet number per microcapsule, in addition to the formation of empty microcapsules, are major drawbacks of this method. However, the size of the microcapsules can be adjusted by changing the nozzle size and the speed at which the solution is flowing. More advanced droplet generators have been developed to control the microcapsule size and decrease the size dispersity in the same batch.

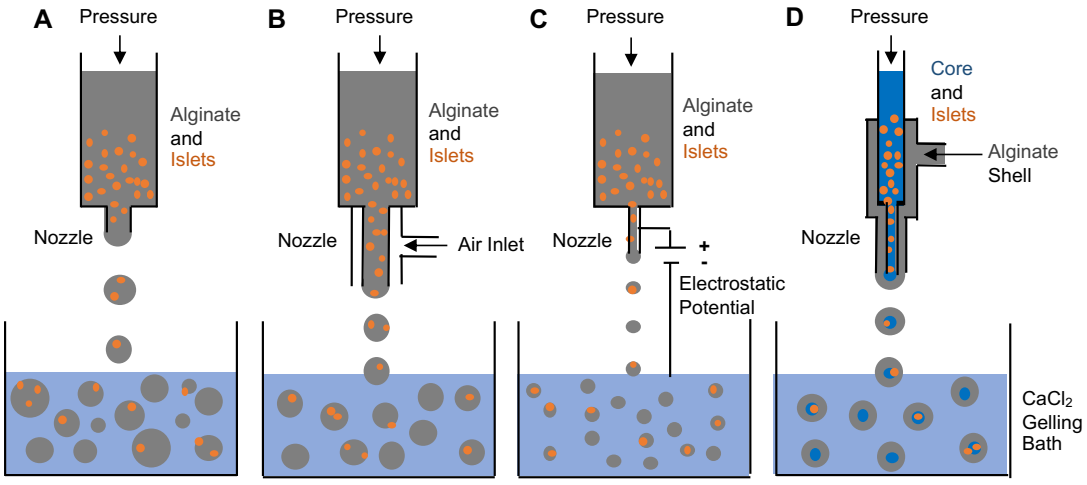

Figure 2.2. Schematic illustration of the different types of droplet generators. (**A**) Basic droplet generator. The generator contains an aqueous solution of alginate suspended with islets. Microcapsules are formed by pushing the solution suspended

with islets through a nozzle and dropping the resultant droplets into a gelling bath with an aqueous solution of divalent cations (often calcium chloride). Droplet size can be tuned by adjusting the size of the nozzle, but it is still difficult to control and can result in a large range of microcapsule sizes. (**B**) Air droplet generator. Coaxial airflow is used to control the size of the microcapsules for producing microcapsules with increased homogeneity in size. (**C**) Electrostatic droplet generator. Applying an electrostatic potential between the nozzle and the gelling solution helps to create smaller and more homogeneous (in size) microcapsules. (**D**) Coaxial droplet generator. This generator consists of a core channel containing islets suspended in a biocompatible core fluid surrounded by a coaxial channel of alginate solution. It produces core−shell microcapsules with islets in the core and alginate in the shell. Core−shell microcapsules decrease immunogenicity because islets are localized in the center of the microcapsule with no direct exposure to the in vivo environment. The core−shell design also allows for the use of various core fluids (e.g., collagen) besides sodium alginate solution, which may help to improve islet survival. Adapted from White et al.[50]

Air droplet generators use coaxial airflow to create microcapsules via surface tension. In the case of islet encapsulation, islets are mixed into an alginate solution which is then contained in an air droplet generator (**Figure 2.2B**). Air droplet generators have demonstrated improved microcapsule formation in multiple studies[84,85]. Electrostatic droplets are generated via an electrostatic potential between the tip of the nozzle and hydrogel solution (**Figure 2.2C**). This method has been shown to decrease microcapsule sizes and increase microcapsules uniformity. One study used a method called electrohydrodynamic jetting (**EHDJ**) in which a high-voltage electric field was applied between the gelling solution and the jetting needle. No negative effects on cell proliferation were detected[86]. Electrostatic droplet generation has also been used for islet encapsulation[87,88]. Another group employed a nozzle method to create a "conformal coating" around islets to reduce the microcapsule sizes[89]. The method was performed using a microfluidic chamber coaxial jetting system with oil and aqueous phases. Coatings with thicknesses between 10 and 50 μm were achieved but did not readily protect islets from immune cells[90].

The majority of studies that used the droplet generator method for microcapsule extrusion utilized only one material such as alginate to contain the islets. One major drawback of this method is that the islets may become partially exposed to the external physiological environment. This can trigger immune reaction, defeating the purpose of encapsulation. To prevent islet exposure to the external environment, a core−shell microcapsule design can be used (**Figure 2.2D**). In the core−shell encapsulation, two different materials can be used in the core and shell, respectively. This is performed by using a coaxial flow of an aqueous solution, usually of alginate, to surround an islet-laden core fluid[83]. Ma et al. used electro-jetting to generate islet-laden core−shell microcapsules. An in vivo evaluation of core−shell versus solid microcapsules revealed that core−shell microcapsules had less fouling and maintained normoglycemia in mice for a longer period than solid microcapsules[88].

2.5.5. Microfluidic cell encapsulation

Cell encapsulation using microfluidic devices has become popular in recent years due to the wide availability of photolithography and 3D printing for creating masters or molds. Photolithography-based mold creation involves applying a photoresist to a silicon wafer to create a master mold. The master mold is then used repeatedly to generate PDMS-based microfluidic devices by soft lithography[91]. Microfluidic devices are very tunable and can be adjusted to create different types of flow paths for various functions. Microcapsules are formed at fluid shearing junctions such as T-junctions (**Figure 2.3A**) and flow focusing junctions (**Figure 2.3B**)[92]. Once the microcapsules are created, they are gelled using divalent ions or ultraviolet (**UV**) light exposure. Alginate is the most popular material to use for microfluidic cell

encapsulation because it is easily cross-linked using calcium chloride. PEG is another material commonly used to create microcapsules because it can be photo-cross-linked as the microcapsules flow through the device channels. Microfluidics has also been used for islet encapsulation. Using microfluidics to encapsulate islets increases the control of microcapsule size and uniformity. Smaller microcapsules can be produced compared to nozzle-based droplet generating methods which have much less control over size[93,94].

Core−shell microcapsules can also be created using microfluidics (**Figure 2.3C**) and have been used to encapsulate different cell types[95]. After the cell-laden core and shell fluid streams meet in the device, they flow into a flow focusing junction with another shearing fluid. To improve microcapsule formation, these devices are sometimes designed to be non-planar[96]. Typically, the heights of the channels vary with the core channel being the shortest so that the shell fluid can completely encapsulate the core. Multiple studies show the advantages of using a core−shell method for cell encapsulation[14,97]. This microfluidic core−shell method could easily be applied to islet encapsulation which can result in improved cell survival through adjusting the core material[96]. Islets also have less chance of protruding out of the side of the microcapsule due to the shell, mitigating immune response[88].

Due to the infinite number of designs you can make on microfluidic devices, there are innumerable ways to optimize the encapsulation process. One facet that has been explored recently is the scaling-up of microcapsule production. In one study, a microfluidic device with eight outlets demonstrated increased rates of islet encapsulation compared to other methods[98]. For transplantation in clinical trials,

humans need about 10,000 IEQs per kilogram of body weight. The rate of islet encapsulation is also important for maintaining the viability of the islets. While islets are being encapsulated, the already encapsulated islets will either have to be cultured or preserved in the wait time. This is very inconvenient and can lead to islet death. Methods that use multiple needles or channels could increase the number of islets encapsulated in a reduced period of time to allow for scale-up, without increasing the flow rate or shear stress on islets.

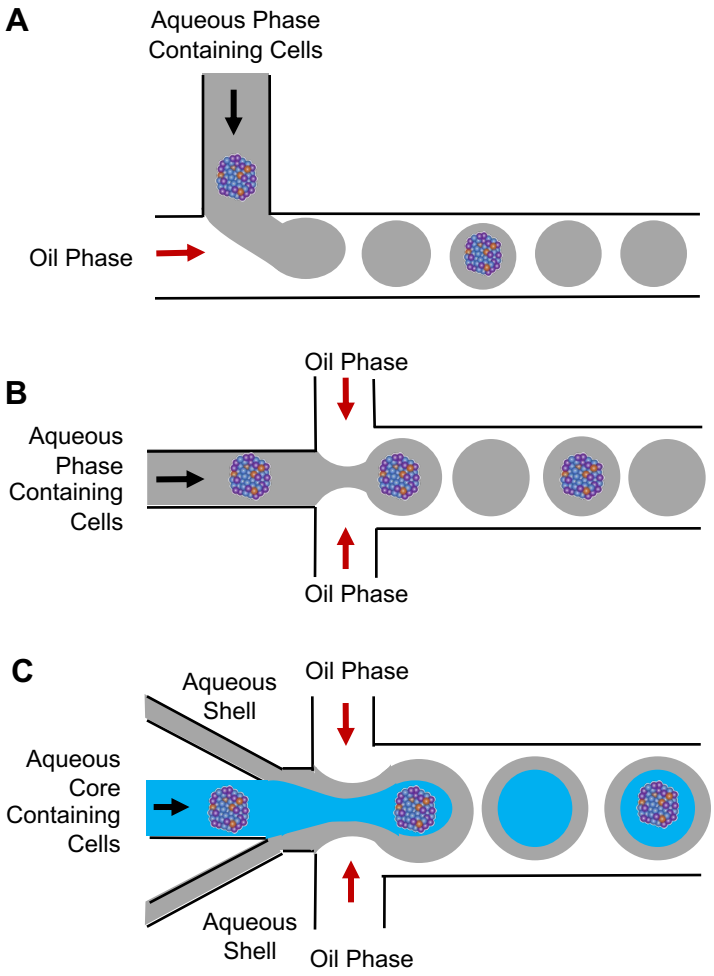

Figure 2.3. Microfluidic encapsulation of islets. (**A**) T junction-based microfluidic mechanism for microcapsule generation to encapsulate islets. The immiscible oil flow

is used to shear the aqueous flow suspended with islets into droplets which are further cross-linked into hydrogel for islet encapsulation. (**B**) Flow focusing-based microcapsule generation with a similar mechanism to the T junction-based approach. (**C**) Core−shell flow focusing-based microcapsule generation. Two (core and shell) aqueous flows are used for generating core−shell microcapsules with islets being encapsulated in the core. The core−shell design prevents direct contact between islets and the surrounding environment and allows the use of different biomaterials for the core and shell, which may improve islet survival and function. Adapted from White et al. [50]

2.5.6. Microcapsule purity and sorting

The purity of microcapsules has not been discussed in current literature in detail. When encapsulating islets, many of the generated microcapsules contain no cells due to the low density of islets used in the aqueous fluid. This large number of empty microcapsules make downstream processing difficult, and in particular, are undesired for cell/tissue transplantation for which the space available in vivo for housing the transplants is very limited[14,15]. In order to remove empty microcapsules, sorting is needed. This can be done manually or by moving all the microcapsules to another device for sorting, which is tedious and may cause sample loss, contamination, and/or, cell damage[99,100]. Separating islet-laden and empty microcapsules by hand is extremely difficult, and on-chip microcapsule sorting could fix this problem[96]. On-chip microcapsule sorting using dielectrophoresis is a label-free sorting method that may be applied for islet encapsulation[15,16].

Another challenge is that oil is not favorable for cell viability[14,95,101,102]. Therefore, an effective method for selective extraction of cell-laden microcapsules from oil into an isotonic aqueous phase timely on-chip can be very important to maintain the cell quality for use in clinical settings. Several methods have been reported for extraction of microcapsules from oil into an aqueous phase based on the size and/or

natural hydrophilicity of the microcapsule surface[103-107]. However, these studies have not explored selective extraction of cell-laden microcapsules. Several studies reported optical detection of cell-laden microcapsules to selectively extract them[108,109]. However, these methods require either fluorescently labeling the cells or squeezing the cell-laden constructs. The former may negate the utility of the cell-laden microcapsules for cell-based medicine while the latter may damage the cell-laden hydrogel microcapsules permanently. More recently, a label-free method was demonstrated for on-chip selective extraction of cell aggregate-laden microcapsules from oil into an aqueous solution using an optical sensor and dielectrophoresis (**DEP**)[16]. However, the purity is low: only ~30% of the extracted microcapsules are cell-laden. In addition, cell aggregates less than ~80 μm in diameter are not detectable with the optical sensor-based method.

2.5.7. Deep learning-based on-chip sorting

With the development of high capacity graphical processing units (**GPUs**) and availability of big data, deep learning has risen to prominence as an accessible tool for many fields in recent years, especially in the field of image processing[110-116]. Deep learning is a type of machine learning that uses neural networks (nodes connected by varying weights) to make predictions based on the input data[117]. Supervised learning is a type of deep learning in which a program can be used to classify different objects that are input into the system, by first "learning" from pre-labeled objects that are used to train the program[118]. Object classification can be very useful for biomedical applications, and deep learning can be used to detect subtle features in images, which may surpass human performance[110,111]. More recently, deep learning has been used to

detect live and dead cells, as well as different types of cells[119,120]. However, nearly all prior studies have been focused on analyzing static images offline. Two studies have used machine learning to identify and separate droplets containing cells from droplets without cells on microfluidic devices in real-time, but these studies require complex imaging setups with special photodetectors, do not result in high purity and efficiency in sorting, and/or do not create hydrogel microcapsules for further processing[121,122]. One study has examined sorting hydrogel microcapsules (containing no cells/tissues) of different sizes by deep learning[123]. The capability of deep learning in real-time detecting cell/tissue-laden hydrogel microcapsules for their label-free on-chip selective extraction has not been explored so far.

2.5.8. Macroencapsulation

Macrodevices are usually in millimeters to centimeters in size, allowing for multiple islet encapsulation. Their large size makes macrodevices easily tunable, as membrane size, thickness, and pore size can all be precisely adjusted. One device has the potential to hold the large number of islets necessary for diabetes treatment[49]. However, the thickness of the device makes small molecule exchange difficult, which can lead to cell death and decreased insulin release. Because many islets are enclosed in one device, the surface area available for small molecule exchange is reduced. Additionally, some macrodevices are made of materials that have been shown to increase the immune response and fibrotic build-up[124]. Since limited oxygen transport is a major flaw of large devices, many macrodevice designs focus on increasing the amount of oxygen that reaches the islets, or to increase vascularization[49,125-127].

Increasing nutrient and insulin diffusion through adjustment of material pore size is also a largely studied area[128].

2.5.9. Conformal encapsulation

Recently, research has been performed to create conformal coating of islets, which involve very thin layers of materials coated onto the islets or using other methods to create a coating that is very similar to the actual size of the islets. This allows for increased diffusion across the biomaterial membrane, while still minimizing immune reaction (**Figure 2.1C**)[81].

2.5.10. Islet co-encapsulation

Encapsulating islets with other cells has been shown to decrease the body's immune response, reduce pericapsular fibrotic overgrowth (**PFO**), improve islet survival, improve graft revascularization, and increase insulin production. Mesenchymal stem cells (**MSCs**) have immune-evasive properties and can improve tolerance to transplanted tissue, and have been shown to increase insulin production[129-132].

2.6 Islet isolation and transplantation

2.6.1. Islet Isolation

To ensure successful and long-lasting transplantation, it is vital to start with healthy islets. The most popular way to isolate islets is through a perfusion process. Most human islet isolation protocols follow the Edmonton Protocol for Islet Transplantation[43]. Islets are separated by digesting away the exocrine tissue, often

utilizing the Ricordi Chamber (**Figure 2.4A**)[133]. Adding the digestion solution through the pancreatic duct allows spreading throughout the exocrine tissue while leaving the islets intact. Collagenase-based digestion enzymes that are most often used for pancreatic digestion include Liberase MTF, Collagenase IV, and Collagenase XI among others[134]. The enzyme selection is also species dependent[135,136]. Following digestion, islets are separated from other digested tissue using gradient separation. Ficoll-based gradients are most typically used[137].

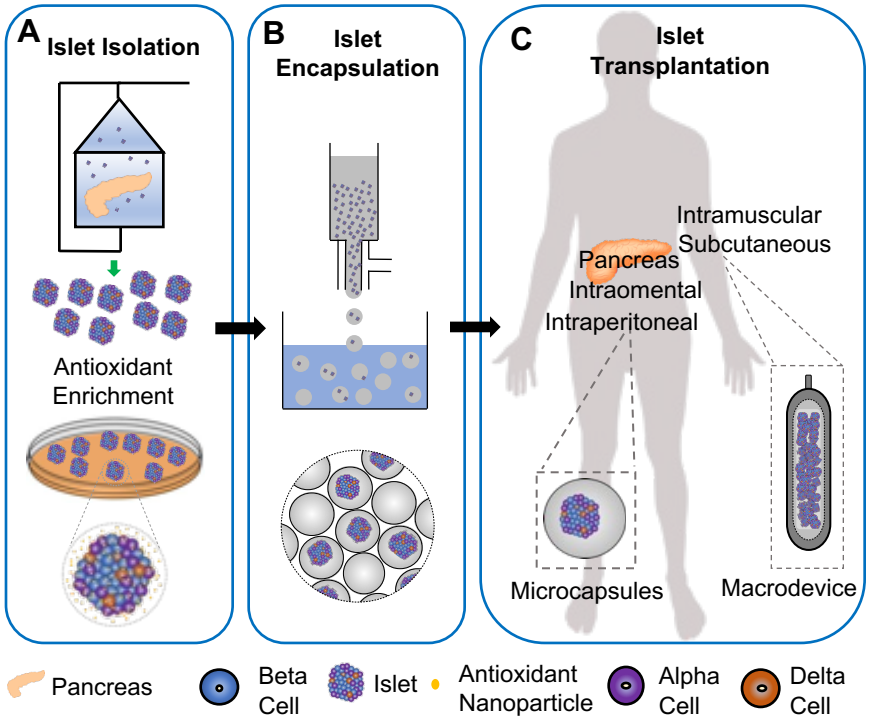

Figure 2.4. Schematic illustration of islet isolation, encapsulation, and transplantation process for human transplantation. (**A**) Islets can be isolated from a deceased donor's pancreas via various digestion and separation procedures. A popular method of islet tissue separation is using a Ricordi Chamber (top). Administration of antioxidants can help to improve islet survival after isolation and during culture. Nanoparticles can be used to facilitate the delivery of antioxidants (bottom). (**B**) Islet encapsulation can be performed using many methods (see **Figures 2.2 and 2.3**), the most common being microencapsulation in alginate using a droplet generator (top). (**C**) Islet implantation sites. Various types of encapsulations are made for different transplantation sites. Macrodevices, such as the TheraCyte device, are commonly implanted subcutaneously (right). Microcapsules are typically implanted in the

peritoneal cavity (left). Other popular implantation sites include the omentum pouch and intramuscular implantations. Adapted from White et al.[50]

Ficoll-400 solutions of varying densities are layered on top of one another, and after centrifugation, the islets will localize to one layer of the Ficoll. The islets can then be collected and washed. Other types of gradients that have been utilized to improve separation include bovine serum albumin and Histopaque [138,139]. A major limitation of using Ficoll and many other separation gradients is that they are toxic to the islets after long exposure, so the process must be performed quickly[140]. Moreover, islets can get lost during separation, and even after separation the extracted islets might still contain small amounts of exocrine tissues. The exocrine tissues must be manually removed by hand which can lead to contamination. The islet isolation process must be further optimized to be less cytotoxic and more efficient.

Once islets are isolated, it is best to transplant them as soon as possible. It is beneficial to culture or cryopreserve isolated islets in vitro to maintain their viability/function before encapsulation. After isolation, the capillary network in islets is severed without blood supply. This can make it difficult to get nutrients and oxygen into the islet core of large islets and they may develop necrotic cores. As will be discussed in following sections, many methods can help prevent islet core necrosis post-isolation.

2.6.2. Transplantation Areas

Traditionally, nonencapsulated islets are transplanted into the portal vein of the liver. This allows for direct contact with the circulatory system, which can enhance

vascularization, increase nutrient and oxygen supply, and improve survival[7]. One drawback of using nonencapsulated islets for transplantation is that patients are required to be on immunosuppressants. On the other hand, encapsulated islets take up a lot more space than nonencapsulated islets because encapsulation requires additional biomaterials (often hydrogels) around the islets and the transplantation of empty microcapsules (**Figure 2.4B**). In addition, placing microcapsules into the portal vein can be dangerous due to possible blockage. The transplantation location for an islet-laden device is very important and dependent on the type of encapsulation[141].

For encapsulated islets, many different transplantation areas have been tested (**Figure 2.4C**). Subcutaneous implantation is a very popular route since it has easy access and is noninvasive. Many macrodevices are implanted subcutaneously. Some examples include the TheraCyte and β-Air devices[49,142]. Subcutaneous implants can also be easily removed or replaced with new devices. A major drawback of subcutaneous implants is the possible lack of oxygen exchange and nutrients, which can stifle islet survival. Intramuscular implantation is another popular route[143]. However, the intramuscular implantation procedure is more difficult compared to other implantation site procedures. It is also difficult for oxygen to reach the implants due to a lack of surrounding vasculature at a resting state and limited early neovascularization[144].

The most popular transplantation area for microencapsulated islets is the peritoneal cavity[38,145,146]. Transplantations in the peritoneal cavity require minimal surgical procedures and can contain a large amount of implanted material. Although devices implanted into this region can be removed, the removal process is more

invasive than subcutaneous removal. More vascularization is observed intraperitoneally compared to subcutaneously, however, vascularization is still limited in the peritoneal cavity unless the islets are implanted on the cavity wall. In addition, it has been shown that the diffusion of insulin and nutrients is also better intraperitoneally than subcutaneously[141]. Some implant areas (e.g., epididymal fat pads) are selected to increase vascularization potential[90].

The greater omentum also has good vascularization potential, as well as proximity to the portal vein for improved insulin delivery to the body[147]. Intravascular transplantation has the benefit of being directly inside the bloodstream but can also pose several dangers for the patient. This procedure requires vascular surgery for implantation and has the potential to easily clog vasculature[83]. Due to multiple limitations and risks, the field no longer pursues intravascular transplantation of encapsulated islets.

2.6.3. Improving islet viability

One major problem that occurs during islet transplantation is islet hypoxia. Since islets are a dense cluster of cells, it is easy for the core of the islet to become hypoxic due to the diffusion limit of oxygen and nutrients (often only a few hundred microns)[148,149]. Also, the severance of the capillary network present in the islet during isolation further hinders the core cells from obtaining sufficient nutrients. Islets may experience undesired hypoxia during the first 7 days after transplantation. During this time, up to 70% of cells could die[21]. Significant islet death could also occur right after transplantation. Furthermore, exposure to a new environment in vivo can lead to significant cell death, diminishing the amount of insulin production[150].

Physiological concentrations of antioxidants have been shown to help to prevent cell death in hypoxic conditions. Bilirubin is one of the most well-studied antioxidants regarding islet viability. Bilirubin interferes with hypoxia-induced apoptotic pathways through the downregulation of apoptotic genes including TNF-α and upregulation of antiapoptotic genes including HO-1 and bcl-2. Bilirubin is an effective therapeutic at approximately 10 to 20 μM for organ perfusion[151-153]. Bilirubin had been shown to downregulate the release of damage-associated molecular patterns (**DAMPs**) from islets (which are major contributors to the host immune response), and incubation of islets with a physiologic dose of 20 μM bilirubin was shown to significantly decrease cell death under hypoxic stress[152]. Nanoparticle encapsulation technology has been used to increase the uptake of bilirubin into islets. In the work of Fullagar et al.,[154] bilirubin-loaded nanoparticles were shown to improve islet uptake of bilirubin. Islets were incubated with nanoparticles containing 0−20 μM bilirubin, and it was found that 5−10 μM bilirubin led to lower cell death levels of an insulinoma cell line (**INS-R3**) during hypoxia in vitro (bottom, **Figure 2.4A**). Physiological concentrations of antioxidants have been shown to increase islet viability under hypoxic conditions and reduce immune response[152].

When islets are transplanted, significant amounts of reactive oxygen species (**ROS**) are generated which leads to immune cell infiltration and pro-inflammatory cytokine-mediated apoptosis.[143] In the work of Lee et al.,[144] an oxygen carrier material, perfluorodecalin (**PFD**), was added to alginate at a 1:5 ratio of 1.908g/mL PFD to 2% alginate. Islets were then encapsulated in the PDF-alginate mixture, which resulted in reduced production of ROS, improving cell viability. Shalaly et al. used islet

dissociation to increase cell viability during culturing[155]. Islets were dissociated into single cells so that nutrients could reach individual cells, preventing a necrotic core during culture. The cells were further cultured and then seeded on silk scaffolds, resulting in the formation of islet-like clusters. Device designs have also been used to increase the amount of oxygen that reaches cells[49,125,126]. Other cell-based methods, such as co-encapsulation of islets and preconditioned adipose tissue-derived stem cells, have been used to increase vascularization around encapsulated islets[156].

2.6.4. Preventing fibrotic overgrowth

Pericapsular fibrotic overgrowth (**PFO**) is one of the main reasons that encapsulated islet transplantation has not had success in clinical trials[18]. PFO is a fibrotic build-up that occurs due to an immune response to implanted materials. In the case of islet transplantation, this build-up prevents the islets from receiving nutrients and secreting insulin. PFO is much more prevalent in large animals than small animals, so it is essential to study ways to prevent fibrotic build-up for clinical translation[157]. One approach to reduce the immune response after islet transplantation is modifying the alginate used for encapsulation of islets[158-160].

2.7 Conclusion

Islet encapsulation has greatly advanced over the past few decades. Although clinical trials are being performed on microencapsulated islets, there has not been a trial that has shown well-controlled blood glucose levels in patients over several years. Nonencapsulated islet transplantation requires patients to take immunosuppressants long-term, which can be very detrimental to health. The goal of islet encapsulation is

to prevent the body from rejecting implanted islets while allowing the islets to release insulin and receive the nutrients they need to survive for many years. For islet transplantation to become a viable standard of care, it must provide a long-term therapeutic effect. Long-term insulin release in patients first requires isolation methods for obtaining healthy islets. In addition, the encapsulation processes must not reduce the health of the islets. Methods for mitigating post-transplantation hypoxia can also be implemented to decrease cell death. The encapsulation needs to permit the exchange of oxygen and nutrients while preventing immune response and fibrotic build-up. By using engineering strategies to address these problems, islet transplantation could become a standard for T1D treatment.

Chapter 3 : Deep Learning-enabled Label-free On-chip Selection and Selective Extraction of Cell Aggregate-laden Hydrogel Microcapsules*

3.1 Introduction

Microfluidic encapsulation of cells/tissues in hydrogel microcapsules has attracted tremendous attention in the burgeoning field of cell-based medicine. However, when encapsulating rare cells and tissues (e.g., pancreatic islets and ovarian follicles), the majority of the resultant hydrogel microcapsules are empty and should be excluded from the sample. Furthermore, the cell-laden hydrogel microcapsules are usually suspended in an oil phase after microfluidic generation, while the microencapsulated cells require an aqueous phase for further culture/transplantation and long-term suspension in oil could compromise the cells/tissues. Thus, real-time on-chip selective extraction of cell-laden hydrogel microcapsules from oil into aqueous phase is crucial to the further use of the microencapsulated cells/tissues. Contemporary extraction methods either require labelling of cells for their identification along with an expensive detection system or have a low extraction purity (< ~30%). Here, we report a deep learning-enabled approach for label-free detection and selective extraction of cell-laden microcapsules with high efficiency of detection (~100%) and

extraction (~97%), high purity of extraction (~90%), and high cell viability (>95%). Our utilization of deep learning to dynamically analyze images in real-time for label-free detection and on-chip selective extraction of cell-laden hydrogel microcapsules is unique and may be valuable to advance the emerging cell-based medicine.

3.1.1. Background

Microencapsulation of cells and tissues has become a very popular area of research for its ability to encase cells in a 3D environment which can be utilized in cell-based medicine including tissue engineering, regenerative medicine, and cell-based therapies[64,149,161-163]. For example, microcapsules can be used to create a biomimetic environment for ovarian follicles and a biocompatible immunogenic barrier for stem cell and islet transplantation.[13,14,50,164,165] Microfluidics has been widely explored for cell and tissue encapsulation because of its good controllability in terms of the size, morphology, and composition of the microcapsules[92,94]. Microfluidic cell encapsulation is usually accomplished by shearing cell-laden aqueous fluids with a water-immiscible fluid (e.g., oil)[58,166,167]. One major challenge is that the percentage of cell-laden microcapsules to total microcapsules generated is very small (< 5%) due to the low cell density required for encapsulating only one piece of cell/tissue or cell aggregate per microcapsule, and in the case of pancreatic islets and ovarian follicles, the limited amount of these precious tissues that can be isolated[134,164,168-172]. This large number of empty microcapsules make downstream processing difficult, and in particular, are undesired for cell/tissue transplantation for which the space available in vivo for housing the transplants is very limited[15]. In order to remove empty microcapsules, sorting is needed. This can be done manually or by moving all the

microcapsules to another device for sorting, which is tedious and may cause sample loss, contamination, and/or, cell damage[99,100]. Another challenge is that oil is not favorable for cell viability[102]. Therefore, an effective method for selective extraction of cell-laden microcapsules from oil into an isotonic aqueous phase timely on-chip can be very important to maintain the cell quality for use in clinical settings.

Several methods have been reported for extraction of microcapsules from oil into an aqueous phase based on the size and/or natural hydrophilicity of the microcapsule surface[103-107]. However, these studies have not explored selective extraction of cell-laden microcapsules. Several studies reported optical detection of cell-laden microcapsules to selectively extract them[108,109]. However, these methods require either fluorescently labeling the cells or squeezing the cell-laden constructs. The former may negate the utility of the cell-laden microcapsules for cell-based medicine while the latter may damage the cell-laden hydrogel microcapsules permanently. More recently, a label-free method was demonstrated for on-chip selective extraction of cell aggregate-laden microcapsules from oil into an aqueous solution using an optical sensor and dielectrophoresis (**DEP**)[171]. However, the purity is low: only ~30% of the extracted microcapsules are cell-laden. In addition, cell aggregates less than ~80 μm in diameter are not detectable with the optical sensor-based method.

With the development of high capacity graphical processing units (GPUs) and availability of big data, deep learning has risen to prominence as an accessible tool for many fields in recent years, especially in the field of image processing[110-115]. Deep learning is a type of machine learning that uses neural networks (nodes connected by

varying weights) to make predictions based on the input data[117]. Supervised learning is a type of deep learning in which a program can be used to classify different objects that are input into the system, by first "learning" from pre-labeled objects that are used to train the program[118]. Object classification can be very useful for biomedical applications, and deep learning can be used to detect subtle features in images, which may surpass human performance[110,111]. More recently, deep learning has been used to detect live and dead cells, as well as different types of cells[119,120]. However, nearly all prior studies have been focused on analyzing static images offline. Two studies have used machine learning to identify and separate droplets containing cells from droplets without cells on microfluidic devices in real-time, but these studies require complex imaging setups with special photodetectors, do not result in high purity and efficiency in sorting, and/or do not create hydrogel microcapsules for further processing[121,122]. One study has examined sorting hydrogel microcapsules (containing no cells/tissues) of different sizes by deep learning[123]. The capability of deep learning in real-time detecting cell/tissue-laden hydrogel microcapsules for their label-free on-chip selective extraction has not been explored so far.

3.2 Methods and materials

3.2.1. Materials

The SYLGARD 184 Silicone Encapsulant Clear polydimethylsiloxane (PDMS) was purchased form Dow (Midland, MI, USA), photoresist was purchased from Kayaku Advanced Materials, Inc. (Westborough, MA, USA), and 4 inch silicon wafers were purchased from University Wafer (South Boston, MA, USA). Tubing for

connecting to microfluidic devices was purchased from Cole Palmer (Vernon Hills, IL, USA). The MCF-7 breast cancer cells were purchased from ATCC (Manassas, VA, USA). Materials for cell culture including Dulbecco's Modified Eagle Medium (DMEM), heat inactivated fetal bovine serum (**FBS**), penicillin, streptomycin, and trypsin-EDTA, were purchased from Thermo Fisher Scientific (Waltham, MI, USA).

3.2.2. Fabrication of microfluidic devices

The microfluidic devices were fabricated by soft lithography of PDMS on a mold/master that was created using photolithography. The design of the microfluidic device was created using AutoCAD (Autodesk, Mill Valley, CA, USA) and a mask of the design was printed by CAD/Art Services, Inc (Brandon, OR, USA). The device consisted of two PDMS parts: a top part containing the channels and a flat bottom part. To create the mold, SU-8 2100 photoresist (Kayaku Advanced Materials, Inc, Westborough, MA, USA) was first spin-coated onto a 4-inch silicon wafer (University Wafer, South Boston, MA, USA) to create a 250 μm thick layer. After soft baking on hot plates at 65 °C and 95 °C, the wafer was exposed to UV light through the patterned mask using a MA-4 Mask Aligner (Karl Suss, Munich, Germany). Next, the wafer was hard baked at 65 °C and 95 °C and developed using SU-8 developer (Kayaku Advanced Materials, Inc, Westborough, MA, USA). A post bake was then performed at 120 °C. The spin speeds, baking parameters, and exposure energy were all determined based on the SU-8 2100 datasheet from the manufacturer. PDMS was made by mixing a ratio of 10:1 w/w base to curing agent. To fabricate the top part of the microfluidic device, the PDMS was then poured over the mold, degassed, and baked at 75 °C for 2 h to cure/crosslink the polymer. The bottom part (i.e., a flat slab PDMS of ~1 mm thick)

was created by pouring a thin layer of PDMS over a plain silicon wafer, followed by degassing and 2 h of baking at 75 °C. Afterward, the PDMS parts were cut, and peeled off the mold, and then cleaned using tape. The top and bottom parts of the device were both plasma-treated using a PDC-32G plasma cleaner (Harrick Plasma, Ithaca, NY, USA) at 18 W and 27 Pa for 2 min and bonded together by gently pressing them against each other to assemble into the final device. The device was then baked at 75 °C for 3 days before further use.

3.2.3. Preparation of microfluidic solutions

A 250 mM mannitol solution was created by dissolving mannitol in 10 mM HEPES buffer, and its pH was adjusted to 7.2 using sodium hydroxide. A 2% w/v alginate solution was made by dissolving alginate in the aforementioned mannitol solution. To create the oil phase that is an emulsion of oil and aqueous solution of $CaCl_2$, 2 mL of aqueous $CaCl_2$ solution (1 g/mL) and 186.6 µL of Span 80 were added into 10 mL of mineral oil. Mineral oil is designated as generally recognized as safe (GRAS) by the FDA[173]. Then the mixture was sonicated using a Branson 450 Digital Sonifier (Emerson, St. Louis, MO, USA) for 1 min (20% amplitude). To prepare the 1% w/v methylcellulose extraction solution, the aforementioned 250 mM mannitol solution was slowly added into a 50 mL conical centrifuge tube containing the powder of high viscosity methylcellulose. The sample was mixed by placing it on a rocker (Fisher Scientific), at room temperature for 3 days to completely dissolve the powder. $CaCl_2$ (at a final concentration of 10 µM) was then added into the sample and it was further mixed on the shaker for an additional day. All aqueous solutions were filtered through a 0.22 µm filter.

3.2.4. Culture of cells and aggregates

MCF-7 cells were cultured in DMEM supplemented with 10% heat inactivated FBS, 100 U/mL penicillin, and 100 μg/mL streptomycin at 37℃ in a humidified incubator at 5% CO_2. At ~80% confluency, the cells were detached with 0.25% Trypsin-EDTA. Then, medium was added, and the sample was centrifuged at 200g, followed by removal of the supernatant and resuspended in medium. Cells were then counted with a hemocytometer and diluted with medium to a final concentration of 5×10^4 cells/mL. Drops of 30 μL of the cell suspension were pipetted onto the inner surface of a 100-mm petri dish lid (VWR International, Radnor, PA, USA) using a multi-channel pipette. A total of 15 mL of phosphate buffered saline (**PBS**) was added into the dish, and the lid with the drops was carefully placed on the dish with the drops suspended above the PBS in the dish. The cells were cultured at 37 ℃ and 5% CO_2 for 12 hours to 3 days to obtain aggregates of varying sizes (50-250 μm in diameter) for use in experiments.

3.2.5. Imaging

All on-chip images and movies were captured using an iPhone7 camera attached to a low-cost (~$3,000) Zeiss (Oberkochen, Germany) Primovert microscope at 100x total magnification (10x objective). The microfluidic device was placed on the microscope stage with the detection area aligned in the microscope field of view. An iPhone 7 was mounted to one of the eyepieces of the microscope to obtain images and videos of the detection area. The live phone video of the detection area was streamed to the computer using the iVcam (E2ESOFT, free software) application. In iVcam, the image resolution was set to 1920×1080 pixels and the acquisition speed was set to 30

fps. These imaging tools were used to collect micrographs for training the deep learning model, as well. Off-chip imaging of microcapsules collected from the outlet of the microfluidic devices and fluorescence imaging for assessing cell viability were performed with a Zeiss LSM 710 microscope.

3.2.6. Training of deep learning model

The deep learning model was trained using labeled images of empty and cell aggregate-laden microcapsules. Images of air bubbles and noise in the oil phase were included to help the model distinguish between noise, microcapsules, and cell aggregates. First, iVcam was used to record videos of microcapsules in the detection region using an iPhone7 attached to the eyepiece of a Zeiss Primovert microscope. Then the videos were split into frames, and frames with empty microcapsules and cell aggregate-laden microcapsules were collected (400 empty and 400 aggregate-laden). Images were cropped to include only one microcapsule and labeled as "empty" or "cell aggregate-laden" using the program LabelImg in the Python Package Index (**PyPI**). Labeled image data were then divided randomly into training and testing data (80% training, 20% testing). Images were used to train the deep learning models using Tensorflow (Google) for 100,000 steps. Testing data was then used to confirm the model's detection precision.

3.2.7. Microfluidic cell encapsulation, extraction, and collection

For microfluidic encapsulation, the aforementioned 2% (w/v) alginate solution suspended with the MCF-7 cell aggregates (~1,000 per mL), oil phase, and 1% w/v high viscosity methylcellulose solution (10 mL) in syringes were introduced into the

microfluidic device through the Cole Palmer tubing using the Harvard Apparatus (Holliston, MA, USA) Elite 11 syringe pumps via three different inlets. During encapsulation, microcapsules in both the oil (i.e., not extracted) and aqueous solution (i.e., extracted) were collected for a total of 1 hour, to determine efficiency and purity of the deep learning-enabled extraction. They were collected using P1000 pipettes and transferred into 5 mL of 250 mM mannitol solution containing 10 mM $CaCl_2$ in a 50 mL conical centrifuge tube. To further gel the microcapsules, a 200 mM $CaCl_2$ solution was added to the collection solution in a 1:1 ratio to create a 100 mM $CaCl_2$ solution. Gelling was performed for 60 seconds, and then the rest of the 50 mL conical centrifuge tube was filled with 250 mM mannitol solution for washing, to remove the $CaCl_2$ and any residual oil. After the microcapsules sunk to the bottom of the tube, the top of the solution was removed, and the microcapsules were transferred to a 6-well plate for counting.

3.2.8. Microfluidic-electronic interface setup

The system overview and experimental setup are shown in **Figure 3.1**. In the extraction region, two 25-gauge Hamilton (Reno, NV, USA) needles were used as the electrodes (E1 and E2). These two electrodes were loop-connected to a switch (Pololu basic SPDT relay carrier with 5 VDC relay) powered by an 8.4 V power converter (AA Portable Power Corp, CA, USA) which was controlled by a Mbed NXP LPC1768 microcontroller (Pololu, Las Vegas, NV, USA). The switch was connected to a Gamma High Voltage Research (Ormond Beach, FL, USA) RMC5R voltage generator. A direct current (**DC**) voltage, V_a, of 250 V was applied to the circuit of the electrodes through switch. The extraction region of the device was monitored using a cell phone. The cell

phone was attached to the eyepiece of the microscope and connected to the computer through a USB cable. The iVCam was then used for real-time image and video streaming from the cell phone camera to the computer. At the start of running the program, the detection area (10 μm upstream of the extraction area) was selected by drawing a bounding box on a frozen video frame. The bounding box was manually selected on the frozen video frame by clicking the top left and bottom right corners of the region. The bounding box then remained in the same spot until the program is ended. After generated at the FFJ, microcapsules flowed towards the detection area where detection and extraction then occurred once the program started to run.

3.2.9. Detection efficiency and extraction efficiency and purity

Detection efficiency was used to determine the deep learning program's ability to detect cell aggregate-laden microcapsules. To determine the detection efficiency, videos of the deep learning system running detection were analyzed. DtTP (detection true positive) was defined as the number of cell aggregate-laden microcapsules that contained cell aggregate that the system categorized as positive, and DtFN (detection false negative) was defined as the number of microcapsules that contained cell aggregate but did not categorize as positive by the system. The detection efficiency (DtE) was calculated as follows:

$$DtE = DtTP \,/\, (DtTP + DtFN) \quad (\mathbf{3.1})$$

Extraction efficiency and purity were used to evaluate the system's detection abilities combined with extraction abilities. When microcapsules were collected, they were classified as follows: EtTP (extraction true positive, collected from the aqueous exit) is the number of aggregate-laden microcapsules that were categorized correctly

as containing cell aggregates and extracted, EtTN (extraction true negative, collected from the oil exit) is the number of empty microcapsules that were categorized correctly as empty and not extracted, EtFP (extraction false positive, collected from the aqueous exit) is the number of microcapsules that were empty but were extracted (either through incorrect categorization or being extracted by DEP due to a capsule flowing through the extraction region while DEP is still activated), and EtFN (extraction false negative, collected from the oil exit) is the number of microcapsules that were filled and were not extracted (either through incorrect categorization or not being in the extraction region when DEP was activated). To calculate these values, microcapsules from both the aqueous and oil outlets were collected (n=3). The extraction efficacy (EtE) and purity (EtP) were calculated as follows:

$$EtE = EtTP / (EtTP + EtFN) \quad (\mathbf{3.2})$$

$$EtP = EtTP / (EtTP + EtFP) \quad (\mathbf{3.3})$$

3.2.10. Cell viability

Live and dead cells were labeled using calcein AM (Corning, Inc., Corning, NY) and propidium iodide (PI) (Invitrogen, Carlsbad, CA), respectively. Microcapsules from both the aqueous and oil exits were collected for one hour into a 50 mL conical centrifuge tube containing 5 mL of 250 mM mannitol solution with 10 mM $CaCl_2$ kept on ice, followed by further gelling with 100 mM $CaCl_2$. The microcapsules were then rinsed once by filling the rest of the 50 mL conical centrifuge tube up with the 250 mM mannitol to remove $CaCl_2$ and any possible residual oil. After the microcapsules sunk down to the bottom of the tube, the supernatant was aspirated out, and replaced with medium containing 5 μM calcein AM and 5 μM PI. They were

then incubated at 37 ℃ for 30 minutes, followed by fluorescence imaging. This was performed for the unencapsulated aggregates (control) (n=3) and extracted encapsulated aggregates (n=3). For each independent run, ~7 aggregates were imaged in each group. Using ImageJ, the red area of dead cells and the green area of live cells was compared to the total area of the aggregates to determine the percentage of dead and live cells, respectively.

3.2.11. Statistical Analysis

Statistical analyses were performed in Excel using unpaired Student's two-tailed *t*-test assuming equal variance. Data was reported as mean ± standard deviation from at least three independent runs. A *p value* less than 0.05 was considered statistically significant.

3.3 Results and discussion

In this study, we report a deep learning-enabled label-free method for highly efficient on-chip detection and selective extraction of cell aggregate-laden hydrogel microcapsules. This is achieved through using categorically labeled images to train a deep learning-based detection model, which is then used to dynamically analyze the real-time images for label-free detection of the cell aggregate-laden microcapsules with ~100% efficiency. The MCF-7 cell aggregates are used to mimic single pancreatic islets or ovarian follicles. Once detected, a DEP force is activated to extract the cell-laden microcapsules from oil into an aqueous phase with high efficiency (~97%), high purity (~90%), and high cell viability (>95%). DEP is a simple and fast method of moving particles that allows for a quick transfer of microcapsules from oil into an

aqueous phase. It is also independent on the stiffness and particle size as other methods can be[15]. As illustrated in **Figure 3.1A-B**, the system consists of a microfluidic device for microcapsule generation, a cell phone camera for imaging the on-chip detection area, a deep learning model for detection via analyzing the video frames from the camera in real-time, and a microcontroller that receives the output from the deep learning model and controls the switch to activate/deactivate the DEP-based extraction.

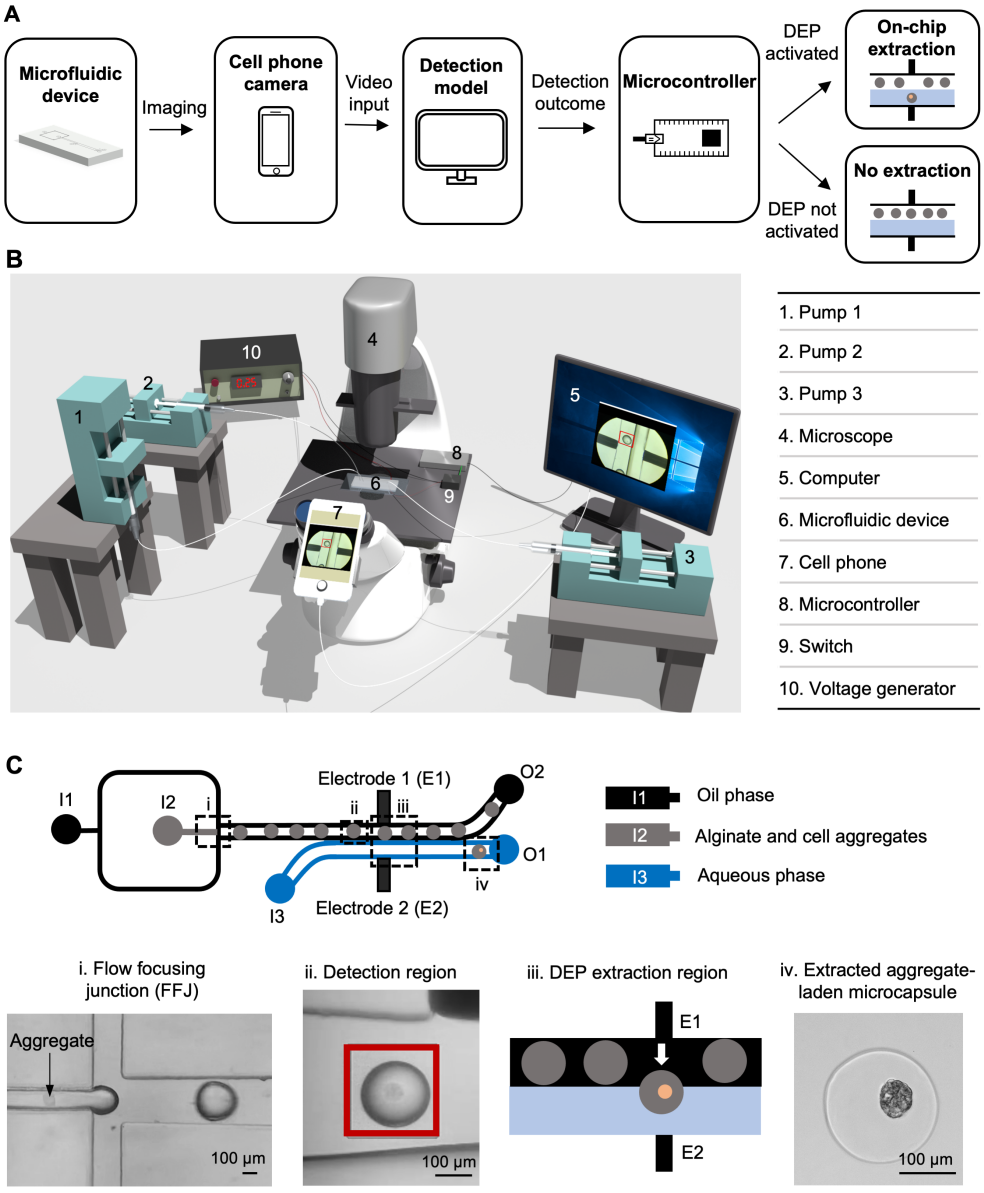

Figure 3.1. An overview of the deep learning-based detection and extraction system. (**A**) Flow chart of the overall system design and order of operations. (**B**) A 3D schematic illustration of the experimental setup. (**C**) A diagram of the microfluidic device showing its use for generating microcapsules and the deep learning-based label-free on-chip selective extraction of the cell aggregate-laden microcapsules. The microfluidic device consists of an oil channel inlet 1 (I1) for flowing an oil phase (containing $CaCl_2$), an I2 for flowing isotonic aqueous sodium alginate solution suspended with cell aggregates, and an I3 for flowing the isotonic aqueous extraction solution. Microcapsules are formed at the flow focusing junction (FFJ, i), gelled in the downstream gelling channel, and further flow into the detection region (ii) where images are taken for real-time detection. A deep learning-based detection program processes the images to determine if the microcapsules contain a cell aggregate or is empty. Once a cell aggregate-laden microcapsule is detected, the microcontroller is informed to turn the switch on, activating DEP force to extract the cell aggregate-laden microcapsule into the aqueous extraction channel (iii). Extracted microcapsules then flow down to the aqueous outlet (O1) where they are collected (iv). Non-extracted microcapsules continue to flow with oil to outlet O2. Adapted from White et al.[17]

The workflow of our approach is further illustrated in **Figure 3.1C**. In the microfluidic device, an aqueous solution of sodium alginate containing cell aggregates is connected to inlet 1 (I1), the oil phase that contains $CaCl_2$ for gelling the sodium alginate solution into calcium alginate hydrogel is connected to I2, and the isotonic aqueous extraction solution is connected to I3. The flow rates are 200 μL/h, 2 mL/h, and 6 mL/h for the sodium alginate solution, oil phase, and extraction solution, respectively. At the flow focusing junction (**FFJ**, i), the aqueous alginate solution is sheared by the oil phase to form microdroplets. The microdroplets are gelled into microcapsules by $CaCl_2$ in the oil phase at the FFJ and the downstream gelling microchannels before detection. Some of the microcapsules contain a cell aggregate and the majority of them are empty.

The microcapsules further flow into the detection region (ii) where images are taken by a cell phone camera via the objective of a low-cost Zeiss (Oberkochen, Germany) Primovert bright-field light microscope. This is done by attaching an iPhone

7 cell phone (Apple Inc., CA, USA) to the microscope with the phone camera being overlayed on the microscope eyepiece (**Figure 3.1B**). The phone also relays the images to a computer. The deep learning model on the computer analyzes the input images in real-time to determine if the microcapsule currently in the detection region contains a cell aggregate or is empty. This information is then sent to a microcontroller, which controls a switch that turns on when the model determines there is a microcapsule containing a cell aggregate in the detection region. Based on the flow rate of the oil phase, distance between two adjacent microcapsules, inference time of the detection system, and time needed for DEP activation, a distance of 10 μm is chosen between the detection region and electrode location to ensure timely extraction of a detected cell aggregate-laden microcapsules with minimal interference of neighboring microcapsules. When the switch is turned on, an electric field is applied across the microchannel via the two electrodes (E1 and E2, located at 10 μm downstream of the detection region) to generate DEP force for selectively extracting the cell aggregate-laden microcapsule from the oil phase into the isotonic aqueous extraction solution (iii).

The extracted microcapsules then flow to the outlet 1 (O1, iv), while non-extracted microcapsules stay in the oil phase and flow to the outlet O2 (**Figure 3.1C**). The microcapsules have a diameter of 219.4 ± 8.2 μm. Pictures of the microfluidics and detection setup and the microcontroller can be seen in **Figure 3.2A** and **Figure 3.2B** respectively. The schematic of the setup between the electrodes and microcontroller as well as a to scale sketch and image of the microfluidic device can be seen in **Figure 3.2C** and **Figure 3.2D, respectively**

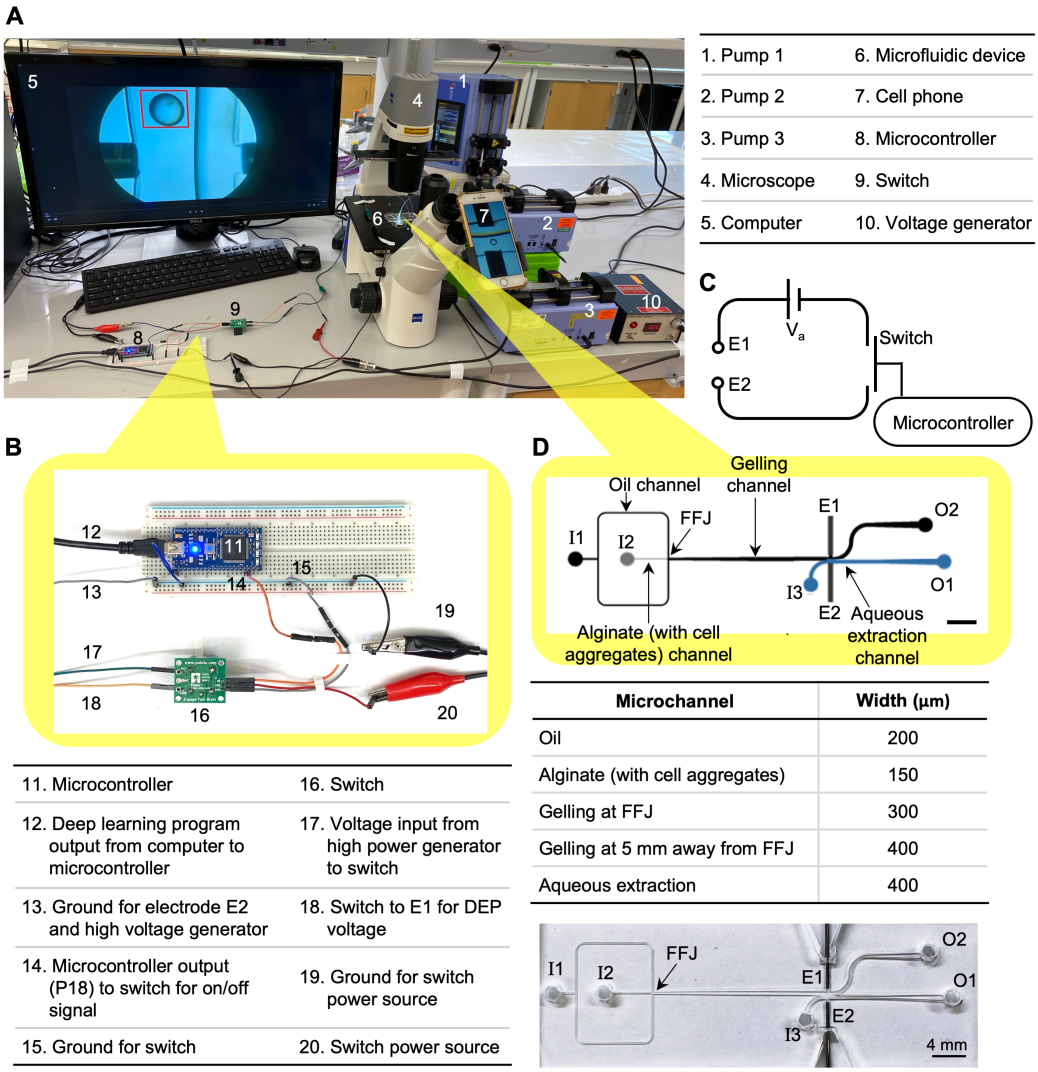

1. Pump 1	6. Microfluidic device
2. Pump 2	7. Cell phone
3. Pump 3	8. Microcontroller
4. Microscope	9. Switch
5. Computer	10. Voltage generator

11. Microcontroller	16. Switch
12. Deep learning program output from computer to microcontroller	17. Voltage input from high power generator to switch
13. Ground for electrode E2 and high voltage generator	18. Switch to E1 for DEP voltage
14. Microcontroller output (P18) to switch for on/off signal	19. Ground for switch power source
15. Ground for switch	20. Switch power source

Microchannel	Width (μm)
Oil	200
Alginate (with cell aggregates)	150
Gelling at FFJ	300
Gelling at 5 mm away from FFJ	400
Aqueous extraction	400

Figure 3.2. An illustration of the complete system design. (**A**) A real photo of the experimental setup with labels to explain the different components. (**B**) A real picture showing the circuit connection of the switch and microcontroller on an electronic circuit board. (**C**) The electric circuit connecting the electrodes, switch, and controller. V_a: 250 V. (**D**) A sketch (drawn to scale) of the microfluidic channels (top view) in the microfluidic device together with a table listing the microchannel dimensions and a real photo of the microchannels and electrodes. The gelling microchannel is 300 μm in width at the flow-focusing junction (FFJ) and it gradually increases to 400 μm at 5 mm away (downstream) from the FFJ. All channels are 250 μm in height. Adapted from White et al.[17]

As aforementioned, a deep learning model is utilized to enable label-free detection of cell aggregate-laden microcapsules in real-time in this study. This is

achieved through training the deep learning neural network model using pre-labeled (i.e., with or without a cell-laden microcapsule) images of the detection region (**Figure 3.3A**). Once the model is trained, images from the cell phone camera showing the detection region of the microfluidic chip are read into the detection program and the model determines whether or not there is an aggregate-laden microcapsule in the detection region in real-time. Based on the speed needed for real-time detection and the imaging rate of the iPhone 7 camera, an acquisition speed of 30 frames per second (**fps**) is chosen, meaning the time interval between two adjacent image frames should be ~33 ms. Interestingly, we find that there is some variability in the actual acquisition speed. The actual time interval between two adjacent image frames ranges from 18-50 ms (**Figure 3.3B**).

Therefore, for real-time application at 30 fps, the inference time (the time it takes the model to distinguish between an aggregate-laden and empty microcapsule in real-time) must be no greater than 18 ms. Using MobileNet as the backend structure, the model achieves the shortest inference time of ~16 ms (**Figure 3.3C**), while the inference time of the Inception model fluctuates between ~15 and ~33 ms and the ResNet model has the longest inference time of ~400 ms. Based on these findings, MobileNet has the shortest inference time (16 ms) and is chosen for further experiments. To train the model using MobileNet as the backend structure, images of microcapsules in the detection region are taken and labeled as being cell aggregate-laden or empty (400 for each) as the input images. Images of noise and air bubbles were also included in training to improve detection efficiency. The model is trained for

100,000 steps, using TensorFlow (Google) on a GTX 1050ti GPU with 16 GB memory[174].

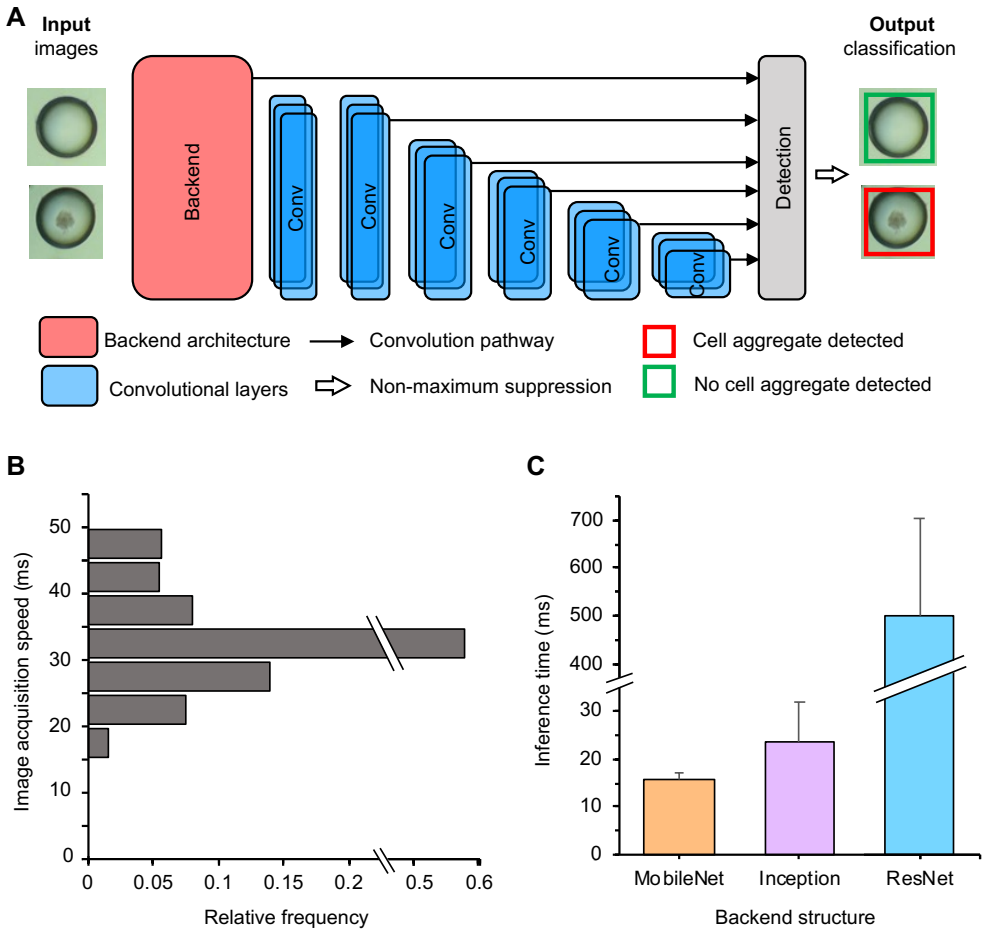

Figure 3.3. Characterization of the deep learning approach for label-free detection. (**A**) An illustration of the deep learning detection model including the backend architecture and a convolution (Conv) neural network using the single shot multibox detection (**SSD**), for detecting cell aggregate-laden microcapsules. (**B**) Quantitative data showing the image acquisition speed using the iPhone 7 camera. (**C**) Inference times of the deep learning detection models with three different backend structures. Adapted from White et al.[17]

We then conducted real-time extraction on cell aggregate-laden microcapsules, enabled by the deep learning-based label-free detection of the cell aggregate-laden

microcapsules on-chip using the detection model trained with the MobileNet backend structure. We determined the efficiency and purity of our approach for both detection and selective extraction through microcapsule collection and counting, as well as quantification of cell viability. A video frame breakdown of the detection and extraction area (**Figure 3.4A**) with deep learning-based detection and selective extraction is shown in **Figure 3.4B**. After formation at the FFJ and further gelling in the downstream gelling microchannel, the microcapsule flows into the detection area. The deep learning detection model running on the computer can then determine if the microcapsule is empty or cell-laden. The detection region is indicated by a green box (**Figure 3.4 b.1**) that turns red when the model detects a cell aggregate-laden microcapsule (note: the color change indicates a cell aggregate to the user and is not necessary for performing the detection or extraction).

If a cell aggregate-laden microcapsule appears in the detection region (**Figure 3.4 b.2-3**), the computer program sends a corresponding signal to the microcontroller which is connected with the computer through USB (COM6). The microcontroller then activates DEP for 0.15 seconds to extract the cell aggregate-laden microcapsule from oil phase into the aqueous phase (**Figure 3.4 b.4-6**). The duration of 0.15 seconds for DEP activation is determined experimentally to achieve the extraction of one microcapsule per DEP activation, based on the speed of the microcapsules, time between microcapsules passing the extraction region, and time of extraction. If no cell aggregate-laden microcapsule is detected, DEP stays off and the microcapsule continues to flow down the oil channel (**Figure 3.4 b.7-9**). This selective extraction process can be seen in both **Supplemental Video 3.1** (in full speed) and **Supplemental**

Video 3.2 (in full speed except when extraction occurs, and it is slowed down to 10% speed for better visualization of the extraction process).

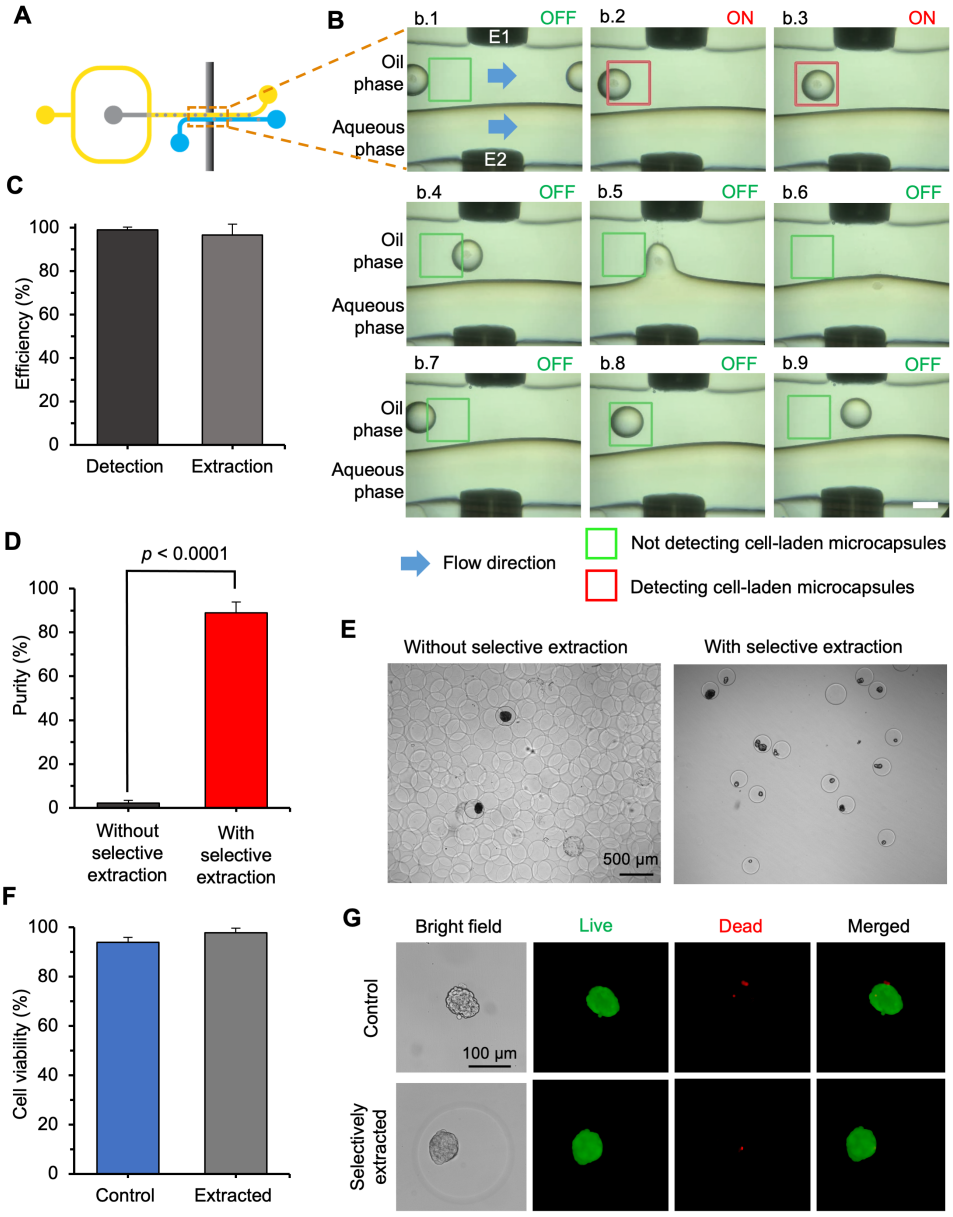

Figure 3.4. Characterization of the deep learning-enabled detection and selective extraction of cell aggregate-laden microcapsules. (**A**) Diagram of microfluidic device design with detection and extraction region indicated by orange box. (**B**) Typical image sequence showing the selective extraction of a cell aggregate-laden microcapsule from oil into the aqueous extraction solution. The blue arrows indicate the flow direction, and the red/green box is the detection area. The green box indicates either no microcapsule or an empty microcapsule is present in the detection region,

while the red box represents a cell aggregate-laden microcapsule is detected in the detection region. (**C**) Quantitative data of the deep learning-based detection efficiency and selective extraction efficiency of cell aggregate-laden microcapsules (n=3 independent runs with ~1000 microcapsules per run). (**D**) Quantitative data comparing the purity of microcapsules without and with the deep learning-based selective extraction (n=3 independent runs with ~1000 microcapsules per run for each condition). (**E**) Images of microcapsules collected from the device without and with selective extractions, showing the difference in purity between the samples. (**F**) Cell viability in both control cell aggregates without microencapsulation or extraction (control) and cell aggregates in microcapsules selectively extracted using the deep learning-enabled label-free method (n=3 independent runs with 7 cell aggregates per run for each condition). (**G**) Bright field and fluorescence images showing live/dead (green/red) staining in both cell aggregates without going through microencapsulation or extraction (control) and cell aggregates in microcapsules selectively extracted using the deep learning-based label-free method. Adapted from White et al.[17]

To determine the detection efficiency, videos of the detection region are analyzed, and the number of cell aggregates are counted. The detection efficiency is the percent of cell aggregate-laden microcapsules that the deep learning program detects out of all the cell aggregate-laden microcapsules passing through the detection region. It is determined that the deep learning-based label-free method can detect cell aggregates (50-250 μm in diameter) with an ~100% detection efficiency (**Figure 3.4C**).

To determine the selective extraction efficiency and purity as well as cell viability, microcapsules are collected from both the aqueous outlet O1 and oil outlet O2 (**Figure 3.1C**). The extraction efficiency is defined as the percent of extracted cell aggregate-laden microcapsules out of all cell aggregate-ladened microcapsules, while the extraction purity is defined as the percent of the extracted cell aggregate-laden microcapsules out of the total extracted microcapsules. The extraction efficiency and purity of the cell aggregate-laden microcapsules in the selectively extracted sample collected from the aqueous outlet O2 are ~97% (**Figure 3.4C**) and ~90 % (**Figure 3.4D**), respectively. The purity of the selectively extracted microcapsules is

significantly higher than that (~2%) without selective extraction. Typical images of the samples without and with selective extraction showing the difference in their purity are given in **Figure 3.4E**.

The cell viability is examined by live/dead staining to determine if the DEP extraction process causes any damage to the cells, since cells have to be highly viable for their further biomedical applications. The cell aggregates in the microcapsules collected from the aqueous outlet O2 are labeled using live/dead (green/red) staining and imaged with fluorescence microscopy, and the green and red areas in the images are quantified using ImageJ. Quantitative analysis of the green/red (live/dead) areas shows more than 95% cells in the selectively extracted microcapsules (n=3 independent runs) are viable (**Figure 3.4F**), which is not significantly different from that of fresh cells (control) in the cell aggregates (n=3 independent runs) without microencapsulation or extraction. Typical fluorescence images are given in **Figure 3.4G**, which shows negligible red (dead) stain, indicating the cells are highly viable.

The deep learning-based label-free method can detect cell aggregates of 50-250 μm in diameter with an ~100% detection efficiency, which enables selective extraction of the cell aggregate-laden microcapsules via DEP force with an ~97% extraction efficiency. This high detection efficiency can also be attributed to the size of the microcapsules and the design of the device, to ensure the cell aggregates are not far away from the plane of focus (i.e., within the depth of focus) so that they show up in the images used by the deep-learning algorithm for detection. This detection method is much better than a previously reported optical sensor-based approach that is unable to detect or extract any cell aggregates less than 82 μm. This is important for biomedical applications, for

instance for islet microencapsulation, because islets can be as small as 50 μm[28]. The purity (~90%) of the deep learning-based extraction is also much higher than that (~30%) achieved with an optical sensor-based detection method for DEP-based extraction. However, the purity is lower than the extraction efficiency. As shown in **Supplemental Videos 3.1** and **3.2**, this is probably because the oil-water interface in the extraction area is destabilized slightly during extraction of a cell-laden microcapsule, which may cause an upstream neighboring microcapsule (either empty or cell-laden) to be extracted if the interface has not completely stabilized by the time when the neighboring microcapsule passes through the extraction region. This issue may be resolved by increasing the oil speed to make the microcapsules further away from each other and/or by improving the interface stability via adjusting the physical properties (e.g., viscosity and electrical conductivity) of the oil and aqueous phases in the extraction channel[175]. This issue may also be overcome by using an extraction method faster than DEP. Similarly, a more precise extraction method could further improve the extraction efficiency to ~100%, since the efficiency for the deep learning-based detection is ~100%.

Of note, the throughput of the system is ~1.5 microcapsules per second. This is due to the flow rates of the aqueous and oil phases used, which are optimized based on the time needed for detection and extraction, as well as the time needed for the oil/aqueous interface to become stable after extracting a cell-laden microcapsule. If the rate of microcapsule generation is too high and the microcapsules are too close to each other, the purity of the extracted cell-laden microcapsules may decrease. This is because the neighboring microcapsules (cell-laden or not) may be extracted either

before the DEP is de-activated, or before the interface becomes stable after extracting a target cell-laden microcapsule. This may contribute partially to the low purity (~30%) of our previous optical sensor-based system with a throughput of ~3.75 microcapsules per second. Nonetheless, for the applications of microencapsulating islets and follicles, usually ~100 follicles or ~1000 islets are needed at a time, making this throughput of ~1.5 microcapsules per second sufficient. For applications that require higher throughput, smaller microcapsules that may cause less interface destabilization could be used, along with more viscous oil phase and aqueous extraction solution to further stabilize the interface, for increasing the throughput while keeping a high purity. The electrical conductivity of the oil phase could also be adjusted for faster extraction. Advances in deep learning and improved backend structures, along with a high-speed camera for imagining, and a faster computer processer and microcontroller can also help to improve throughput. Lastly, throughput may be improved by running multiple microfluidic devices in parallel.

It is also worth noting that this work is focused on cell aggregates with a diameter of 50 – 250 μm for the application of microencapsulating single pancreatic islets and ovarian follicles that have a diameter over the same range. However, the deep learning system can also be trained with images of smaller aggregates or single cells. The microfluidic device and detection system can also be adjusted to ensure that smaller aggregates and single cells can be identified and are within the depth of focus for imaging so that a high detection and extraction efficiency could be achieved. Reducing the microcapsule size may also help to improve detection efficiency, especially for detecting smaller aggregates or one single cell in the microcapsules,

although we did not vary the size of the microcapsules (diameter: 219.4 ± 8.2 μm) in this study. Moreover, the position of cells, the plane of focus, and microcapsule edge opacity may vary with microcapsule size and could affect the detection efficiency, which should be taken into consideration when designing a device and training a deep learning model. This type of model could also be applied to sort cell aggregates based on their size by training the model with images of aggregates of varying sizes in the microcapsules.

Lastly and importantly, the elimination of cell labeling with our label-free method is of great significance to the use of the cells for downstream biomedical applications where labelled cells can't be used, including treating type 1 diabetes with microencapsulated islets, as well as microencapsulation of ovarian follicle for biomimetic 3D culture to treat infertility. Furthermore, our approach allows for a quick transfer of microcapsules from the time of detection to extraction (~15 ms, **Supplemental Videos 3.1** and **3.2**), and microcapsules are moved from the oil phase that is not favorable for the survival of living cells, to an aqueous solution in less than 10 seconds (determined by dividing the gelling microchannel length with the flow rate in the channel), from the time when the microcapsules are generated at the FFJ to their extraction. This may contribute to the high cell viability of the extracted sample. Moreover, this approach eliminates the need for tedious manual sorting of non-labeled aggregates and the associated possibility of sample contamination. Lastly, we used an inexpensive and accessible system setup involving a low-cost inverted bright-field light microscope and a cell phone camera for detection, and an open-source deep learning detection platform, TensorFlow, which does not require extensive modifications.

3.4 Conclusion

In summary, we developed a low-cost deep learning-based method for detecting and selectively extracting cell aggregate-laden microcapsules dynamically, which enables highly efficient label-free detection (~100%) and on-chip selective extraction (~97%) of the cell aggregate-laden microcapsules out of empty ones in a microfluidic device. Furthermore, the extracted samples are with high purity (~90%) and high cell viability (>95%). This technology may find many potential applications including microencapsulating pancreatic islets, ovarian follicles, and stem cell aggregates for the treatment of diabetes and infertility and stem cell-based therapy of many diseases.

Chapter 4 : Deep Learning-Enabled Fabrication of Highly Pure Islet-Laden Biomimetic Core-Shell Hydrogel Microcapsules for Treating T1D in Mouse Model

4.1 Introduction

Microencapsulated islet transplantation for treating type 1 diabetes has predominantly relied on encapsulation techniques involving homogeneous alginate microcapsules[53,176]. The goal of microencapsulation is to provide the islets with a beneficial environment while also preventing immune response and eventual immune rejection[11,53]. While these homogeneous alginate microcapsules offer some immune protection for the encapsulated islets, they have limitations that could prevent successful islet transplantation[93].

Alginate microcapsules, produced through conventional methods such as droplet generation into a gelling bath or electrospray can be relatively large (1mm in diameter) and their size can be challenging to control[93,177]. Large microcapsules have been found to restrict efficient oxygen and nutrient exchange, potentially compromising the health and viability of the encapsulated islets[178-180]. While alginate is a biocompatible material derived from brown seaweed, it does not naturally occur in the body and lacks adhesion motifs to facilitate cell interactions and other characteristics of the native pancreatic environment of islets[181]. Additionally, there is a risk of triggering immune responses if the islets protrude from these microcapsules due to fabrication methods of homogeneous alginate microcapsules[13].

Microfluidic chips present an innovative solution by enabling the creation of microcapsules that can be precisely adjusted using microfluidic device design and flow parameters[96,97]. Microencapsulation also allows for the production of small microcapsules (less than 600 μm in diameter), enhancing nutrient exchange and increasing cell viability and insulin release[97]. Microfluidic devices are extensively used to microencapsulate cells and tissues, resulting in microcapsules typically suspended in an oil phase[182]. However, subsequent steps often involve off-chip processes such as centrifugation to collect and transfer the microcapsules from oil into an aqueous based-solution as discussed in Chapter 3. This can lead to unintended cell damage and microcapsule loss[16]. Furthermore, when encapsulating precious and rare cell aggregates or tissues, such as pancreatic islets, the majority of microcapsules remain empty, with the few islet-laden microcapsules hidden among the empty ones. It is essential to remove empty microcapsules because they take up precious space during transplantation[183]. Hand picking islet-laden microcapsules to remove them from the empty microcapsules is a challenging, time-consuming process that may risk sample contamination.

Non-planar microfluidic devices enable the production of core-shell hydrogel microcapsules, as opposed to conventional homogeneous microcapsules. Importantly, using core materials containing components of the extracellular matrix, such as collagen, can provide the encapsulated islet an environment closer to the native pancreas [77,184,185]. Collagen has been shown to increase cell viability and insulin release when used for islet encapsulation. A combination of collagen and alginate can further improve microcapsules by creating an environment with a stiffness closer to the native

pancreatic environment (approximately 1.2 kPa at a frequency of 40 Hz[186,187]) than just collagen alone[188,189]. Core-shell hydrogel microcapsules have also been shown to help prevent islets from protruding from the microcapsules, thereby reducing the likelihood of immune response[13].

In this chapter, we develop a non-planar microfluidic device capable of encapsulating islets within core-shell hydrogel microcapsules. The device also integrates on-chip selective extraction from an oil emulsion to an aqueous-based extraction solution using DEP and the deep learning-based detection system presented in Chapter 3. Core-shell hydrogel microcapsules and traditionally used homogeneous alginate microcapsules are fabricated and characterized, and islets are encapsulated and tested in vitro. Then, islets are transplanted in vivo in a syngeneic diabetic mouse model, showing superior blood glucose control with core-shell hydrogel encapsulated islets compared with conventional alginate microcapsules.

4.2 Materials and methods

All media and supplements for islet culture were purchased from Thermo Fisher Scientific, and all chemicals were purchased from Sigma unless otherwise specified.

4.2.1. Islet isolation and culture

All animal procedures were approved by the University of Maryland Institutional Animal Care and Use Committee (**IACUC**). For islet isolation, female NCI C57BL/6 mice from Charles River (Wilmington, MA, USA) were used. For Streptozocin (**STZ**)-based diabetic induction, male NCI C57BL/6 mice from Charles River were used. Islets with firefly luciferase expression were isolated from FVB-

Tg(CAG-luc,-GFP) L2G85Chco/J (L2G85) mice from The Jackson Laboratory (Bar Harbor, ME, USA). Islets were cultured in Gibco (Billings, MT, USA) RPMI 1640, supplemented with 10% heat inactivated fetal bovine serum (**FBS**) and 1% penicillin-streptomycin (**P/S**) (Thermo Fisher Scientific) or Gibco Medium 199 with 10% heat inactivated fetal bovine serum and 1% penicillin-streptomycin (Thermo Fisher Scientific). Islets were cultured at 37℃ in a humidified incubator at 5% CO_2.

Collagenase solution was prepared by adding 2 mg/mL of bovine serum albumin (**BSA**) to Hank's balanced salt solution (**HBSS**), along with 1.5 mg/mL of collagenase D. A 5 mL solution was prepared for every mouse from which islets were being isolated. The collagenase solution was drawn into a 3 mL syringe and placed on ice, while the remaining collagenase solution was kept on ice in a 50 mL conical centrifuge tube.

Mice were euthanized using CO_2, followed by cervical dislocation. Each mouse was positioned with its abdomen facing up and sterilized with 70% ethanol. The mouse was then placed under a Zeiss Stemi 305 stereoscope for the rest of the perfusion procedure. The abdomen was carefully incised to expose the intraperitoneal (**IP**) cavity, followed by a bilateral thoracotomy. A cotton-tipped applicator dipped in PBS was used to keep the organs moist during the procedure. The intestines were repositioned to the right, revealing the pancreas, duodenum, and the common bile duct.

The pancreas was perfused using the methods outlined in Li et al. [136] Specifically, the ampulla on the duodenum was clamped using curved hemostatic forceps. A 30-gauge needle was bent to be parallel with the ducts and inserted into the bile duct through the junction of the hepatic duct and the cystic duct. Collagenase was

then slowly perfused through the bile duct into the pancreas, where inflation was observed. The pancreas was carefully dissected away from the duodenum, the remaining intestines, and the spleen using micro scissors. The dissected pancreas was subsequently placed into the remaining collagenase solution and kept on ice. No more than four mouse pancreases were added per 50 mL conical centrifuge tube.

To begin islet isolation, perfused pancreases were placed in a water bath at 37°C for 15 minutes for digestion. Tubes were gently shaken to break up the pancreases, and then the digestion was stopped by filling the 50 mL conical centrifuge tube with RPMI media with 10% FBS and 1% P/S. The tube was then centrifuged at 70 g for 1 minute. A 500 μm strainer was prewetted with RPMI media and the solution was poured through the strainer to remove large pieces of tissue. The solution was then centrifuged at 100 g three times. A density gradient was created to separate the islets from other tissue. For the bottom layer, 9 mL of Histopaque-1119 was added to the remaining tissue and thoroughly mixed. For the middle layer, 6 mL of Histopaque-1077 was gently placed on top of the bottom layer. For the top layer, 6mL of RPMI media was gently placed on top. The conical centrifuge tube was then centrifuged at 1000 g for 20 minutes at 4 °C with a deceleration of zero. After gradient separation, the islets were picked out of the middle layer of the gradient, placed in fresh RPMI media, and centrifuged at 270 g for 4 minutes, followed by 200 g for 3 minutes. The islets were then placed in a petri dish, picked under the microscope using a 10 μL pipette to remove the exocrine tissue, placed in a fresh RPMI media and cultured at 37 °C with 5% CO_2.

4.2.2. Fabrication of non-planar microfluidic device

Devices were created by first fabricating a master/mold using photolithography, followed by using PDMS to create the microfluidic device. Device designs were first created in AutoCAD). Each layer of the non-planar device (consisting of 3 layers) has a different mask, which is aligned to create the final design. The masks were then printed by CAD/Art Services, Inc.

Four-inch silicon wafers from University Wafer were used. The device consists of three layers of photoresist to create the different channel heights using SU-8 2050 photoresist (Kayaku Advanced Materials, Inc., Westborough, MA, USA). First, the silicon wafers were cleaned to remove any residue or dust by washing them with methanol, acetone, and isopropyl alcohol (**IPA**), and rinsing with water. They were then left to sit on a 65 °C hotplate for 5 minutes to ensure the wafer was completely dry.

For coating with photoresist, the directions for spin speed and baking times were determined using the Kayaku Advanced Materials data sheet. The first photoresist layer (100 μm thick) was spin-coated onto the wafer using a Laurell Technologies (Lansdale, PA) spin coater model WS-650MZ-23NPP by starting with a 500 rpm spin speed for 10 seconds with an acceleration of 100 rpm/second, followed by 1750 rpm spin speed for 30 seconds with an acceleration of 300 rpm/second. It was then soft-baked on a 65 °C and 95 °C hotplate for 5 and 20 minutes, respectively. The wafer and the mask for the first layer were then placed in a Karl Suss MA-4 Mask Aligner with a UV light exposure time of 20 seconds. A post-exposure bake (**PEB**) was performed at 65 °C and 95 °C for 5 and 10 minutes, respectively.

The second layer of photoresist (50 μm thick) was then added using the spin coater by starting with a 500 rpm spin speed for 10 seconds with an acceleration of 100 rpm/second, followed by 2500 rpm spin speed for 30 seconds with an acceleration of 300 rpm/second. It was then soft baked on a 65 °C and 95 °C hotplate for 5 minutes and 30 minutes, respectively. The wafer and the mask for the second layer were then placed on the MA-4 mask aligner, and the mask was adjusted so that the alignment marks of the mask were aligned with the alignment marks on the wafer. The wafer was then exposed to 22 seconds of UV, followed by a PEB at 65 °C and 95 °C for 5 minutes and 12 minutes, respectively.

For the third layer (50 μm thick), the spin speed was 500 rpm for 10 seconds with an acceleration of 100 rpm/second, followed by 2500 rpm spin speed for 30 seconds with an acceleration of 300 rpm/second. The soft bake time was 65 °C and 95 °C for 7 minutes and 40 minutes, respectively. The wafer and the third layer masks were then placed on the mask aligner and aligned. The UV exposure time was 25 seconds, and the PEB was at 65 °C and 95 °C for 5 and 15 minutes, respectively. The unexposed photoresist was then removed using SU-8 developer (Kayaku Advanced Materials) for approximately 20 minutes and rinsed with IPA to stop development, followed by a rinse with water. A hard bake was then performed at 65 °C and 95 °C for 5 minutes and 20 minutes, respectively.

After the master/mold was created, SYLGARD 184 Silicone Encapsulant Clear PDMS was used to create the device itself. PDMS was made by mixing base to curing agent at a 10:1 w/w ratio. PDMS was poured over the mold and then cured in an oven at 75 °C for 2 hours. The device was then cut and peeled off the mold and cleaned using

Scotch tape to ensure all dust was removed. The top and bottom pieces of the device were placed in a Harrick Plasma PDC-32G plasma cleaner at 18 W and 27 Pa for 2 minutes, then removed and placed together with methanol in between the two pieces to allow for the channels to be aligned under a microscope. The aligned device was then placed back into the 75 ℃ oven for a minimum of three days before use.

Polytetrafluoroethylene (**PTFE**) electronic and industrial tubing (Scientific Commodities Inc, Lake Havasu City, AZ, USA) with an inner diameter of 0.508 mm and an outer diameter of 2.108 mm (tubing type 1) was added to the inlet holes in the devices. Then, uncured PDMS (also with a 1:10 ratio of base to curing agent) was placed around the connection between the inlet hole and the tubing and placed in the 75 ℃ oven for 30 minutes to seal any space between the tubing and inlets to prevent leaking.

4.2.3. Solution preparation for microfluidic fabrication of microcapsules

First, a 250 mM mannitol solution was created by dissolving mannitol in a 10 mM HEPES buffer. The pH of the solution was then adjusted to 7.2 using a one molar sodium hydroxide solution. To create an alginate solution, Sigma low viscosity alginic acid sodium salt from brown algae (alginate) was purified by first measuring out 4 grams. The alginate was dissolved in 20 mL of chloroform by mixing, and then it was poured onto a VWR (Radnor, PA, USA) 413 filter placed on a Buchner funnel with suction for 30 minutes. This process was repeated twice, and then dried alginate was weighed again and dissolved in water to create a 1% w/v solution. 1% w/v charcoal was added to the alginate solution, and it was stirred at 4 °C for 4 hours. The solution was then filtered using a 0.4 μm bottle filter, frozen at -80 °C, and subsequently

lyophilized on a Labconco (Kansas City, MO, USA) FreeZone 6 L Console Freeze Dryer using machine set points of -80 °C and 0.230 bar for a minimum of 72 hours. A 2.5% w/v purified alginate solution was made by dissolving the purified alginate in 250 mM mannitol. Purified alginate was sterilized by and filtering through a 0.22 μm filter.

1.3% w/v Sigma medium-viscosity carboxymethyl cellulose sodium salt (**CMC**) solution used for the microcapsule extraction solution was created by heating the 250 mM mannitol solution to 80 °C and slowly adding medium-viscosity CMC in the solution while stirring until completely dissolved. The 1.5% v/w high-viscosity CMC solution used in the microcapsule core was prepared in the same manner. Corning rat tail high-concentration type I collagen at a concentration of approximately 8 mg/mL was neutralized using 10% 10X PBS, 1.67% 1M NaOH, and deionized (**DI**) water, resulting in a 6 mg/mL collagen. The neutralized 6 mg/mL type I collagen solution was mixed with a 1% purified alginate solution and 1.5% high viscosity CMC solution to create a 3 mg/mL type I collagen, 0.5% purified alginate, and 0.375% CMC solution to create the core solution for the core-shell hydrogel microcapsules. The core solution was kept on ice before encapsulation to prevent gelling during the encapsulation process. An oil emulsion for microcapsule gelling was created by adding 5 mL of mineral oil to 1.33 mL of a 1 g/mL calcium chloride solution and 93.3 μl of Span 80 in a scintillation vial. They were then emulsified using a Branson 450 Digital Sonifier for 1 minute at a 20% amplitude.

4.2.4. Generation and characterization of microcapsules

A 2.5% purified alginate solution was added into a 1 mL syringe for the shell. Either 2.5% purified alginate solution (for fabricating the homogeneous alginate

microcapsules) or core-shell hydrogel core solution (for fabricating the core-shell hydrogel microcapsules) was added into a 1 mL syringe for the core. The oil emulsion was added to a 10 mL syringe, and the 1.3% medium viscosity CMC extraction solution was added to a 10 mL syringe. Tubing type 1 was joined to all the syringes, connecting them to smaller tubing with an inner diameter of 0.304 mm and an outer diameter of 0.762 mm (tubing type 2), which was connected to the type 1 tubing at the inlets of the device. After optimization of device widths and flow rates, the device that performed best had a core channel with a width and height of 200 μm, a shell channel width and height of 150 μm and 300 μm, respectively, an oil channel width and height of 200 μm and 400 μm, respectively, a flow focusing junction (**FFJ**) width and height of 400 μm, a gelling channel width and height of 700 μm and 400 μm, respectively, and an extraction channel width and height of 700 μm and 400 μm, respectively.

The optimized flow rates were 100 μL/hr for the core solution, 200 μL/hr for the shell solution, 2 mL/hr for the oil emulsion, and 4 mL/hr for the extraction solution. Microcapsules were collected in 250 mM mannitol solution and gelled for 5 minutes using 100 mM $CaCl_2$. They were then washed twice with mannitol by filling a 50 mL conical centrifuge tube to the top with mannitol and letting the microcapsules sink to the bottom of the tube (around 10 minutes) before further use. After collection, images of microcapsules were taken using a confocal Zeiss LSM 710 microscope to determine their size. They were also imaged using a Zeiss Primovert microscope to capture images of the microcapsule's shape. Their size was determined using ImageJ.

To evaluate molecular diffusion out of the microcapsules, microcapsules were incubated with 0.15 mg/mL 10 kDa dextran labeled with fluorescein for 30 minutes.

They were then washed, placed under the microscope, and imaged using green fluorescence at 1, 5, 10, 20, and 40 minutes as the dextran diffused out of the microcapsule. The mean gray value of the image was then analyzed using ImageJ.

4.2.5. Immunofluorescent and viability staining of islets

Islets were stained for viability using calcein AM (Corning Inc) to stain live cells and PI to stain dead cells (i.e., cells with compromised membranes). Subsequently, the islets were placed in a 4-well plate and imaged using a Zeiss LSM 710 confocal microscope. Z-stack imaging and laser scanning were employed to create a three-dimensional rendering of the islets.

Abcam (Cambridge, United Kingdom) rabbit polyclonal anti-insulin antibody was utilized for insulin staining. Initially, the islets were fixed for 30 minutes in 4% paraformaldehyde in PBS. Following fixation, they underwent three washes with PBS and permeabilization using 0.01% Triton X-100 in PBS for 15 minutes at room temperature, followed by further PBS washing. Blocking was carried out with 1.5% BSA in PBS for 1 hour, followed by another round of PBS washing. The islets were then incubated overnight at 4°C in a humidified incubator at 37ºC and 5% CO_2 with the primary anti-insulin antibody at a 1:100 dilution in 1.5% BSA in PBS. On the following day, the islets were washed and stained with an Alexa Fluor 568 goat anti-rabbit antibody (Invitrogen) at a 1:200 dilution in 1.5% BSA in PBS for 2 hours at room temperature. Subsequently, the islets underwent another round of washing and nuclei were stained with 4',6-diamidino-2-phenylindole (**DAPI**) at a 1:250 dilution for 15 minutes at room temperature. After this staining step, they were washed and mounted on a 25 mm x 75 mm x 1 mm microscope slide with a coverslip using CC/Mount.

Finally, they were imaged using a confocal scanning microscope with z-stack imaging to generate a three-dimensional rendering of the islet.

4.2.6. Islets encapsulation

Islets were placed in a solution of either 2.5% purified alginate or core-shell hydrogel microcapsule core solution, depending on the group. They were gently mixed with the core solution and loaded into a 1 mL syringe, which was used to transfer the solution into type 2 tubing carefully. The syringe was subsequently refilled with the core solution without islets and reattached to the tubing. This step was taken to minimize the loss of islets. Islets and core solution mixture was kept on ice until encapsulation to prevent collagen gelling and to keep islets viable.

For islet encapsulation, the flow rate parameters were set at 100 μL/hr for the core, 200 μL/hr for the shell, 2 mL/hr for the oil emulsion, and 4 mL/hr for the aqueous extraction solution. After encapsulation, microcapsules were collected in 250 mM mannitol solution and kept on ice. Following collection, the microcapsules were gelled in 100 μM $CaCl_2$ in 125 mM mannitol. Subsequently, they were washed twice with the mannitol solution, allowing the microcapsules to settle for 15 minutes before removing the supernatant. Finally, the microcapsules were placed in medium 199 with 10% FBS and 1% P/S for culturing.

4.2.7. Microcapsule extraction and application of deep learning-based detection model

For extraction, the device was placed on a Zeiss Primovert microscope with the detection area over the objective. Details about the setup can be found in Chapter 3,

Figures 3.1 and **3.2**. Additionally, comprehensive information regarding the code setup can be found in Chapter 3. A Teledyne FLIR (Arlington, VA, USA) Grasshopper3 USB3 color 32S4C FLIR camera was used for imagining the detection region to input video for the detection model.

4.2.8. In vitro islet culture and characterization

Encapsulated islets were evaluated for viability over time, including alginate microcapsules, core-shell hydrogel microcapsules, and free islets. At 1 and 4 weeks of culturing, islets were stained with PI. The resulting images were then analyzed using ImageJ, and the percentage viability was determined by calculating the percent of PI positive cells and subtracting that from 100% to get the percent of viable cells. At 1 and 4 weeks of culturing, islets were stained for apoptosis using a BD Pharmingen (San Diego, CA, USA) Annexin V- Fluorescein Isothiocyanate (**FITC**) Fluorescence Microscopy Kit by following the kit instructions. Islets were incubated with FITC Annexin for 30 minutes for staining. After staining and imaging, the mean gray value for annexin V was determined for the islets using ImageJ to compare fluorescence levels.

Islets were evaluated using a glucose stimulated insulin secretion (**GSIS**) assay. Glucose solutions were prepared by creating Krebs Ringer Buffer Solution with concentrations of 2.5 mM glucose for the low glucose stimulation (**LGS**) solution and 16.7 mM for the high glucose (**HGS**) stimulation solution. To perform GSIS, twenty islet equivalents (**IEQ**) were placed in 1.5 mL microcentrifuge tubes with 700 μL of the LGS solution and incubated for an hour to establish a baseline. The LGS solution was then removed, replaced with 700 μL of fresh LGS solution, and incubated for

another hour. The top 600 µL of glucose solution was collected, and the solution was replaced with 600 µL of HGS solution. After an additional hour of incubation, the HGS solution was collected, and the samples were stored at -20°C until analysis. An enzyme-linked immunosorbent assay (**ELISA**) was used to quantify insulin secretion using an Invitrogen Insulin Mouse ELISA Kit was used, and results were measured using a Tecan (Männedorf, Switzerland) Spark Multimode Microplate Reader. The insulin concentrations per sample were calculated, and the stimulation index was calculated by dividing the insulin concentration released in the HGS sample by that in the LGS sample.

4.2.9. IVIS imagining of bioluminescent transplanted islets

In vivo imaging of transplanted islets was conducted using a PerkinElmer (Waltham, MA, USA) IVIS Spectrum In Vivo Imaging System. The islets used in this study expressed firefly luciferase and were isolated from L2G85 mice using the isolation method described above. After isolation and culture in RPMI supplemented with 10% FBS and 1% P/S, approximately 400 islets were transplanted IP into C57BL/6 mice using an 18-gauge needle. At 15 minutes before imaging, mice received an IP injection of 50 mg/kg of Gold Biotechnology (St. Louis, MO, USA) D-Luciferin Potassium Salt. The mice were then anesthetized and placed into the IVIS machine. Imaging was performed using Living Image software (PerkinElmer) to capture the bioluminescence emitted by the transplanted islets. The acquired images were then subjected to analysis using the Living Image software to quantify flux values.

4.2.10. IVIS imagining of bioluminescent transplanted islets

For syngeneic in vivo testing, male C57BL/6 mice were used for islet transplantation recipients. Diabetes was induced by injecting mice IP with STZ at a dose of 150 mg/kg intraperitoneally in a pH 4.5 sodium citrate solution. Mice were classified as diabetic if their blood glucose levels exceeded 300 mg/dL for two consecutive days, and blood glucose levels were monitored using a Johnson & Johnson (Rockville, MD, USA) One Touch Ultra 2 blood glucose meter and testing strips.

Islets were isolated from C57BL/6 mice, encapsulated, and then transplanted intraperitoneally into the recipient mice, which were anesthetized with isoflurane using a nosecone. The microcapsules were slowly introduced into the IP cavity using an 18-gauge needle. Non-fasting blood glucose levels in mice were measured three times per week. At approximately day 50 of the study, an intraperitoneal glucose tolerance test (**IPGTT**) was conducted. To perform IPGTT, mice were fasted overnight, and an initial blood glucose reading was recorded. A glucose injection of 2 g/kg was administered intraperitoneally using a 200 mg/mL glucose solution and a 30-gauge needle. Blood glucose measurements were taken at 15, 30, 60, 90, 120, and 150 minutes post-injection.

To assess the immune response to the implants within the IP cavity, mice were euthanized using CO_2, followed by cervical dislocation. Immune cells were retrieved via IP lavage using a saline solution. To perform IP lavage, the IP cavity was flushed with a total of 15 mL of saline. This was done by making an incision in the IP cavity and injecting the saline, gently massaging the saline around the IP cavity, and then collecting the saline in a 50 mL conical centrifuge tube and placing it on ice. Following

the lavage, the solution was filtered through a 70 μm filter to remove any debris and centrifuged at 200 g for five minutes. Cells were washed with PBS and centrifuged again. These cells were then incubated with antibodies at a 1:100 dilution in PBS for 30 minutes on ice. The antibodies used included anti-CD45 FITC as a marker for all white blood cells, anti-CD11b BV510 as a monocyte marker, anti-F4/80 BV785 as a macrophage marker, anti-CD4 Pacific Blue as a marker for CD4 T cells, and anti-CD8 APC for CD8 T cells. Following incubation, the cells were washed and analyzed using a BD FACSCelesta Cell Analyzer, and the results were processed using FlowJo (Ashland, OR, USA) software.

4.2.11. Statistical Analysis

Data analysis in this chapter was performed using GraphPad (La Jolla, CA, USA) Prism 8. The unpaired Student's two-tailed t-test assuming equal variance was used. Data was presented as mean ± standard deviation. A *p value* of less than 0.05 was considered statistically significant.

4.3 Results and discussion

4.3.1. Fabrication and optimization of a non-planar microfluidic device for generating core-shell hydrogel microcapsules

We successfully designed a non-planar microfluidic device to encapsulate islets which creates microcapsules with a hydrogel core and a hydrogel shell (core-shell hydrogel microcapsules). This design has many advantages for microcapsule fabrication. Instead of having a homogeneous microcapsule, the design allows for the composition of the core to be fine-tuned by adjusting the materials while still having a

shell made of alginate, a biocompatible material that has been used in islet transplantation for years[85,190]. The non-planar device design allows for this core to be encapsulated by a layer of shell material (approximately 60 μm thick), unlike a planar device. This creates a layer of shell material thick enough to limit protrusion of islets out of microcapsules[88]. The total microcapsule size, along with the core size, can be easily adjusted by changing the channel width of the device and adjusting the flow rate unlike the popularly used methods for creating microcapsules using droplets from needle into gelling baths and electrospray (**Figure 2.2**)[191,192]. Planar devices also do not allow for the creation of core-shell hydrogel microcapsules[193].

The significant advantage of core-shell microcapsules is control of the core material, which is the environment in which the islets will reside. Homogeneous (non-core-shell) microcapsules face limitations in material selection since their materials must rapidly crosslink. The traditional method for creating microcapsules with distinct inner and outer layers involves fabricating and crosslinking the microcapsules first and then applying the outer coating[11,194], and controlling coating thickness and ensuring a uniform shell around the microcapsules can also be difficult[83,195]. In contrast, on-chip production of core-shell microcapsules results in a solid and well-crosslinked alginate shell, allowing for easy adjustment of the core material. Microcapsule fabrication using the non-planar microfluidic device also allows for easy adjustment of the shell thickness by changing the flow speed or the channel width and fully encapsulates the core[14,97].

Using a microfluidic device also allows for on-chip microcapsule sorting to extract islet-laden microcapsules from empty microcapsules [17], which has not been

researched previously. Extraction is not only used for sorting, but it quickly moves the microcapsules from the oil emulsion to the aqueous-based extraction solution, which can help improve cell health compared with microencapsulated cells that continue to sit in oil[16].

A diagram of the non-planar microfluidic device can be seen in **Figure 4.1A**. The solutions enter the device at inlets 1 to 4. The core solution enters the device through inlet 1 (**I1**) and flows down the core channel to the FFJ. The shell solution (2.5% purified alginate) enters the device through inlet 2 (**I2**) and flows down the two sides of the shell channel toward the FFJ. The oil emulsion (oil and calcium chloride) enters the device through inlet 3 (**I3**) and flows down the two sides of the oil channel toward the FFJ. The oil shears the core and shell solution to create the microcapsule. The microcapsule flows down the gelling channel where the calcium chloride in the oil emulsion gels the microcapsule. The extraction solution (1.3% medium viscosity CMC in 250 μM mannitol solution) enters the device at inlet 4 (**I4**). It flows down the extraction channel, creating an interface with the oil emulsion in the extraction region. The electrodes cause the microcapsule to be extracted using DEP when the voltage is turned on, with electrode 1 (**E1**) connected to the switch and the power and electrode 2 (**E2**) connected to ground. A detailed schematic for DEP extraction can be seen in **Figure 3.2 C and D**. Microcapsules that are not extracted are collected from outlet 1 (**O1**), and extracted microcapsules are collected from outlet 2 (**O2**).

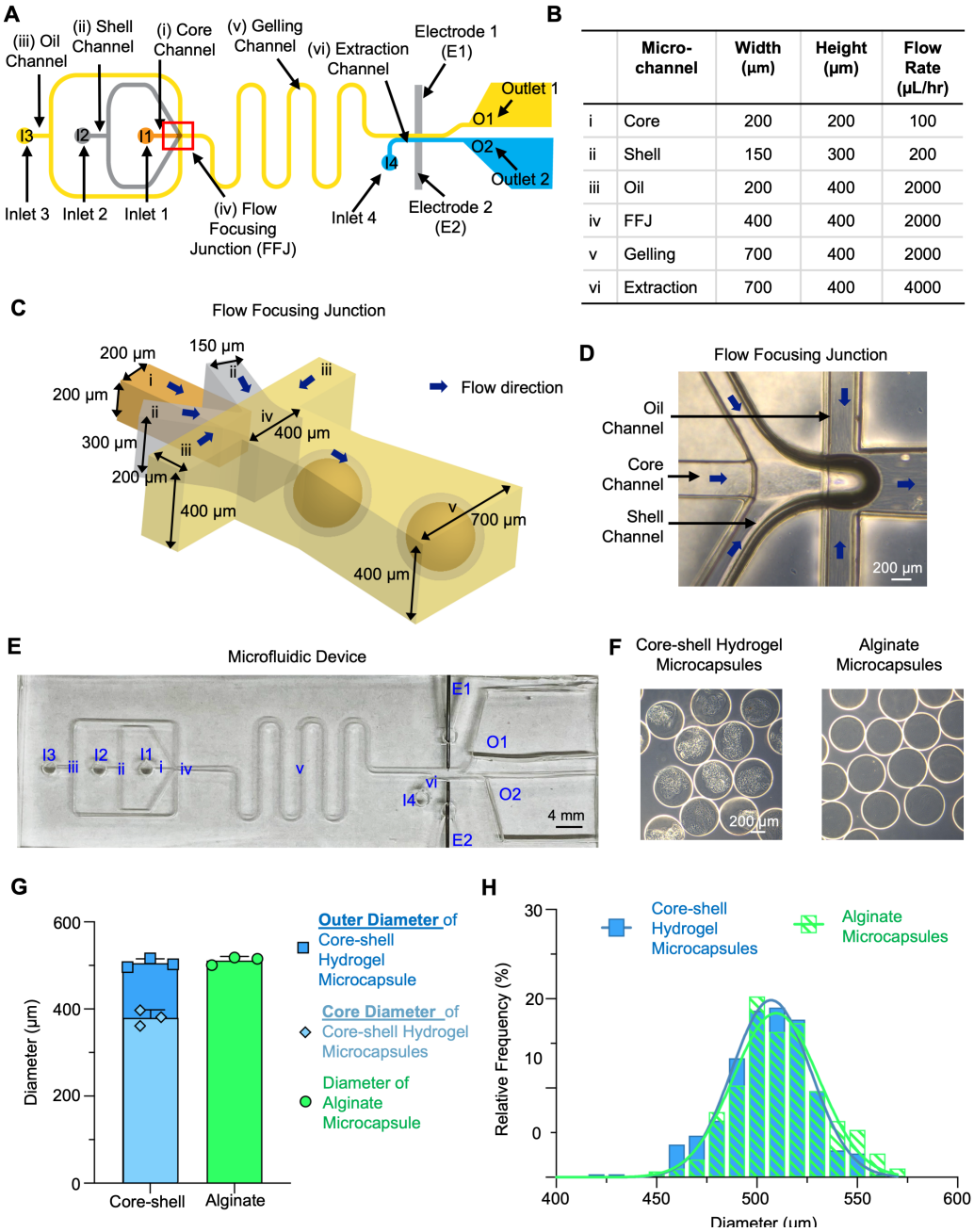

	Micro-channel	Width (µm)	Height (µm)	Flow Rate (µL/hr)
i	Core	200	200	100
ii	Shell	150	300	200
iii	Oil	200	400	2000
iv	FFJ	400	400	2000
v	Gelling	700	400	2000
vi	Extraction	700	400	4000

Figure 4.1. Overview of non-planar microfluidic device and core-shell hydrogel microcapsule/alginate microcapsule fabrication and size measurements. (**A**) Schematic of non-planar microfluidic device with channels, inlets, and outlets labeled. (**B**) Table describing dimensions and flow rates for each microchannel. (**C**) Schematic of non-planar microfluidic device FFJ with widths and heights of channels labeled. The blue arrow represents the flow direction. (**D**) Image of the FFJ with solutions and a microcapsule being created. The blue arrows represent the flow direction. (**E**) Image of the microfluidic device with inlets, outlets, and channels labeled. (**F**) Images of core-shell hydrogel microcapsules and alginate microcapsules fabricated using flow

conditions in **B**. (**G**) Graph comparing the averages of the outer diameter and core diameter of the core-shell hydrogel microcapsules, and the diameter of the alginate microcapsules. n = 3 with 100 microcapsules per run. (**E**) Histogram of the microcapsule diameters for the 300 core-shell and 300 alginate microcapsules. Bin size: 10 μm.

The non-planar microfluidic device is designed with dimensions to ensure the core channel is large enough to accommodate islets without damaging the islets or clogging occurring while also making the microcapsules less than 600 μm to ensure optimal nutrient exchange[11,183,191,196]. Islets range from 50 μm to 350 μm in diameter, with the majority of islets falling between the 100 μm to 200 μm range[28]. Based on the parameters of islet size and total microcapsule size, a core channel width of 200 μm and height of 200 μm is chosen (**Figure 4.1B**).

Alginate is purified to decrease the chance of immune response after transplantation in vivo[197,198]. However, the purification process leads to longer gelling times for the microcapsules. As a result, there is a risk of microcapsule deformation or islet release during extraction from the oil emulsion to the extraction solution. To mitigate this issue, the gelling time needs to be increased before extraction. The planar device in used in Chapter 3 has a straight gelling to allow for optimal spacing between microcapsules for high purity microcapsule samples (**Figure 3.2D**). The straight gelling channel was first lengthened to allow for more gelling time while keeping the microcapsules evenly spaced in the channel for extraction; however, the gelling time still proved to be insufficient. Therefore, a serpentine channel is introduced to provide additional gelling time. Subsequently, more curves are added to the gelling channel (**Figure 4.1A**). Combined with optimization of flow rates (**Figure 4.1B)**, the gelling

time is long enough for sufficient alginate crosslinking to generate well-formed extracted microcapsule.

A detailed schematic of the FFJ including channel widths and heights can be seen in **Figure 4.1C**. As seen in the schematic, the core channel has a width and height of 200 μm. The shell channel and has a height of 300 μm which allows the core solution to be surrounded by the shell solution, and the oil channel has a height of 400 μm which allows the microcapsule to be sheared into a sphere. An image of the FFJ with solutions in the core, shell, and oil channel and a microcapsule being formed can be seen in **Figure 4.1D**. A picture of the microfluidic device with all inlets and channels labeled can be seen in **Figure 4.1E**.

A 2.5% purified alginate solution is used for the microcapsule shell and a solution containing 0.5% purified alginate, 0.375% high viscosity CMC, and 3 mg/mL collagen type I is used for the core solution of the core-shell hydrogel microcapsules. By using these parameters along with optimized flow rates (**Figure 4.1B**), the microcapsules are not damaged upon extraction from the oil channel to the extraction channel. In later experiments, the core-shell hydrogel microcapsules are compared with conventionally used homogeneous alginate microcapsules (called alginate microcapsules) to determine if the core-shell hydrogel microcapsules improve islet viability and glucose responsiveness. To fabricate these alginate microcapsules, 2.5% purified alginate is used in the core channel of the device along with 2.5% purified alginate in the shell channel. Example images of the core-shell hydrogel microcapsules and the conventional alginate microcapsules can be seen in **Figure 4.1F**.

Core-shell hydrogel microcapsules and alginate microcapsules are fabricated and compared to ensure they have a similar average diameter and size distribution for in vitro and in vivo testing **(Figure 4.1G** and **Figure 4.1H)**. For the core-shell hydrogel microcapsules, the average outer diameter of the microcapsules is 505.02 ± 10.15 μm, the core diameter is 377.48 ± 18.09 μm, and the shell thickness is 63.78 ± 14.10 μm. The homogeneous alginate microcapsules have an average diameter of 511.37 ± 9.29 μm (**Figure 4.1G**).

4.3.2. Comparison of dextran diffusion out of core-shell hydrogel microcapsules and alginate microcapsules

Diffusion of molecules out of the microcapsules is assessed using fluorescein-labeled dextran with a molecular weight of 10 kDa. This dextran is chosen because it has a slightly higher molecular weight than molecules that are essential to diffuse through the microcapsule, such as insulin (6 kDa), while having a smaller molecular weight than antibodies such as immunoglobulin G (150 kDa) or proinflammatory cytokines such as interleukin-1β (17.5 kDa), tumor necrosis factor-alpha (17.3 kDa), and transforming growth factor- β (25 kDa)[199-201]. This was done to ensure that insulin can readily move through the microcapsule, and the alginate and core-shell hydrogel microcapsules were compared to determine if the core of the microcapsule negatively affects diffusion compared with the conventionally used alginate microcapsule.

Dextran diffusion is examined from both alginate microcapsules and core-shell hydrogel microcapsules (**Figure 4.2**). First, a dextran solution is incubated with microcapsules for 30 minutes, followed by washing away excess dextran before monitoring diffusion. **Figure 4.2A** shows representative images of dextran

fluorescence within microcapsules at various time points and their corresponding bright field images.

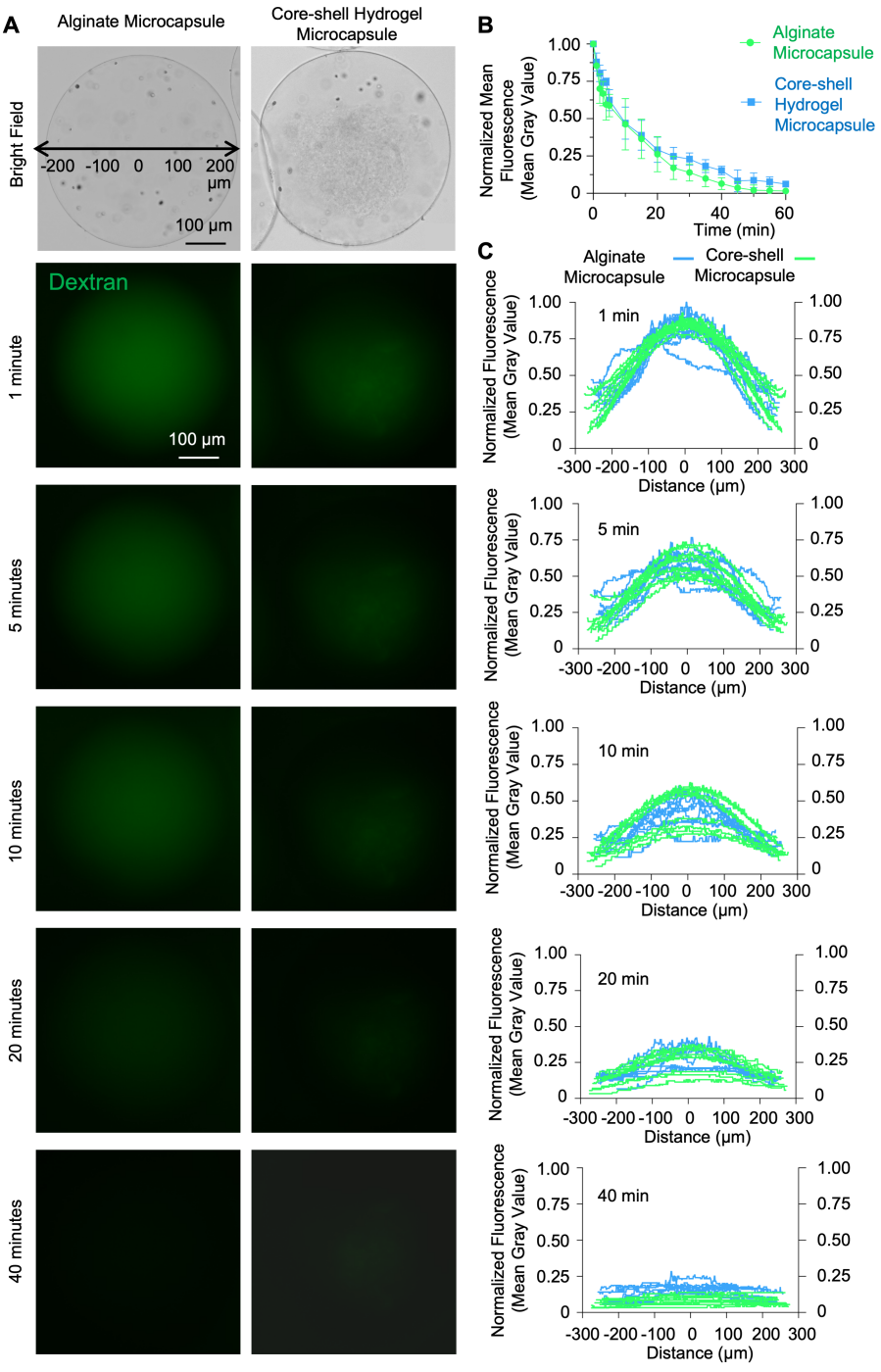

Figure 4.2. Comparison of dextran diffusion out of core-shell hydrogel microcapsules and alginate microcapsules. (**A**) Representative bright field and fluorescent images of microcapsules measured over time. The bright field alginate

microcapsule image illustrates how fluorescence measurements are taken using a line drawn along the diameter of the microcapsule. (**B**) Average fluorescence across the diameter of microcapsules over time, normalized by fluorescence at t = 0 minutes. n = 3 independent runs with 3 microcapsules per trial. (**C**) Fluorescence measurements across the diameter of the microcapsules, with fluorescence measured at various distances from the microcapsule's center. An example of the distance measurement is shown on a microcapsule in 4.4A.

The bright field image of the alginate microcapsule has a line across the diameter representing how the mean gray value was spatially measured. **Figure 4.2B** presents the average mean gray value across the microcapsule diameter over time normalized by the value at time 0. **Figure 4.2C** displays the spatial mean gray value distribution across the microcapsule diameter, following the measurement method shown in **Figure 4.2A** normalized by the measurement at time zero.

The results indicate that dextran molecules can diffuse both into and out of the microcapsules suggesting, that insulin and other molecules essential for nutrients, including glucose and oxygen, easily diffuse in and out of the microcapsules to reach the encapsulated islets[93]. Although there is no significant difference in the average diffusion time between the alginate microcapsules and core-shell hydrogel microcapsules, it takes slightly longer for dextran to diffuse out of the core-shell hydrogel microcapsule. Examining the core and shell of the core-shell hydrogel microcapsule, it also takes longer for the dextran to diffuse out of the core than to diffuse out of the shell, indicating that diffusion is slightly slower in the core material. This could be due to several factors including smaller pore size, varying distribution of pores in the core, and interactions with the molecules and the core material[202,203].

However, these differences did not appear to have any measurable impact on islet health or insulin diffusion, as demonstrated in the subsequent data in this chapter.

4.3.3. Islet isolation and characterization

Islets are successfully isolated from C57BL/6 mice and stained to evaluate their quality. **Figure 4.3A** gives an overview of the isolation process. A detailed description of the process can be found in the methods section. After euthanasia, the mouse's abdomen is cut to expose the IP cavity. The ampulla is clamped using curved hemostatic forceps, and a 30g needle is inserted through the joining site of the hepatic duct and the cystic duct and into the common bile duct. Then, the collagenase digestion solution (1.5 mg/mL collagenase D and 2mg/mL BSA in HBSS) is slowly injected while ensuring the pancreas inflates to achieve proper perfusion. The pancreas is then collected and kept on ice until digestion.

Digestion is performed by incubating the perfused islets in a 37ºC water bath for 15 minutes. Islets are washed with RPMI with 10% FBS and 1% P/S. They are then placed in a histopaque gradient and centrifuged to separate the islets from the other tissue. Islets are then collected from the second layer of the gradient, washed, and placed in a petri dish with RPMI media. Islets are then picked to remove them from the other remaining tissue using a 10 µL pipette, placed in a petri dish with fresh RPMI media, and incubated until further use. The typical morphology of islets directly after isolation with a shiny appearance is shown in **Figure 4.3B**. Moreover, they are highly viable, as demonstrated by the fluorescence image of live/dead (green/red) staining a typical islet (**Figure 4.3C**). Islets are also stained with DAPI (blue) for nuclei and for

insulin with an anti-insulin antibody (red), showing they are releasing insulin (**Figure 4.3D**).

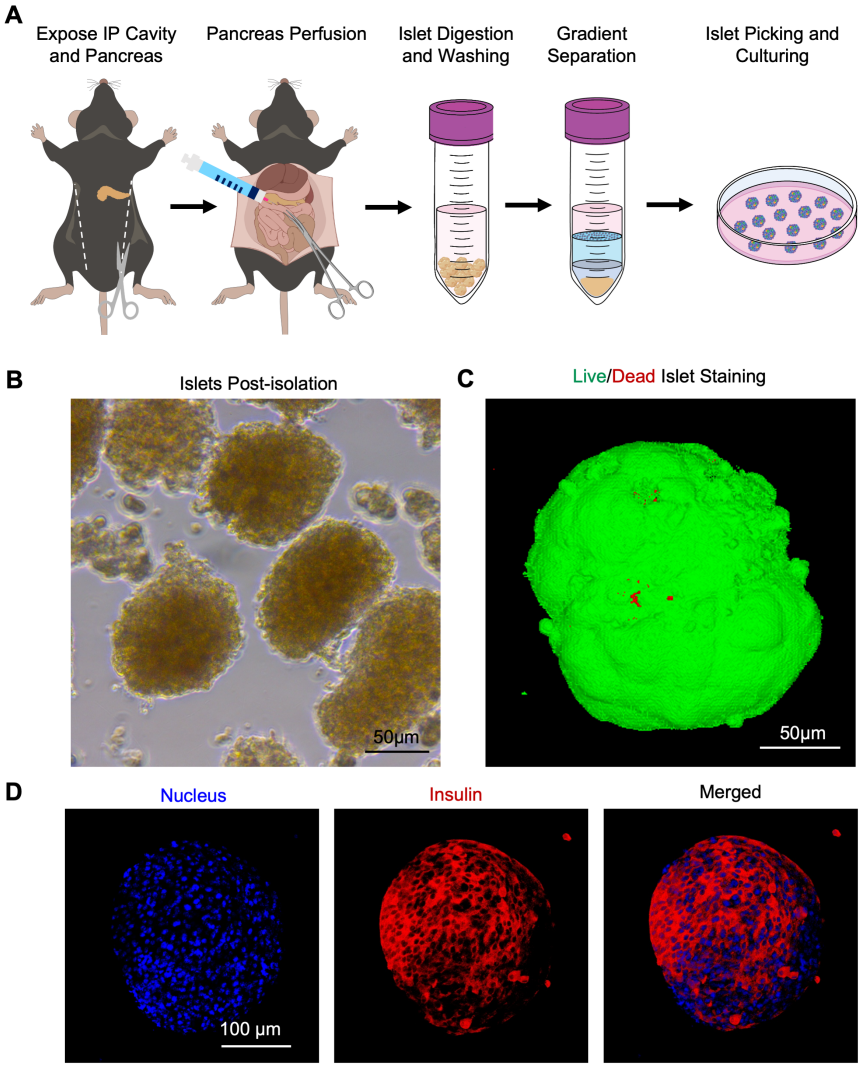

Figure 4.3 Islet isolation and characterization. (**A**) Schematic illustration of the islet isolation process. Drawings adapted from BioRender. (**B**) Image of islets post-isolation. (**C**) Confocal image of islet stained with live/dead (green/red) staining with a 3D reconstruction. (**D**) Images of islets stained for nucleus (blue) and insulin (red).

4.3.4. Islet encapsulation and sorting using deep learning-based detection system and extraction

Successful islet encapsulation and extraction is achieved using the non-planar microfluidic device. Due to the gelling of the alginate in the serpentine channel before extraction, all islets that enter the flow focusing junction can be successfully encapsulated in microcapsules. The serpentine gelling channel ensures thorough microcapsule gelling, preventing islets from escaping the microcapsules from the force of transitioning between the gelling and extraction channels (**Figure 4.4A**). Due to the low concentration of islets required to prevent islets clumping, resulting in multiple islets in a single microcapsule, the majority of microcapsules are empty.

Figure 4.4A shows the islets flowing down the core channel into the FFJ. Microcapsules created at the FFJ are empty or contain an islet. The microcapsules then move into the gelling channel, followed by the detection and extraction region, where there is an interface between the oil emulsion and the extraction solution. The electrodes in the region create a DEP force that extracts the microcapsules from the oil emulsion in the oil channel to the aqueous-based extraction solution in the extraction channel with both the microcapsules and islets remaining intact.

Figure 4.4B shows images from a video (**Supplemental Video 4.1**) of islet-laden microcapsules being extracted from the oil channel to the aqueous channel in the extraction region. In **Figure 4.4 b.1,** the microcapsule moves towards the extraction region where DEP is on. When it reaches the extraction region, the DEP force causes the microcapsule to be pushed towards the extraction solution (**b.2**), where it is pulled into the extraction channel with the microcapsule still intact and the islet still in the

center (**b.3**). The intact microcapsule then moves down the extraction channel to be collected (**b.4**).

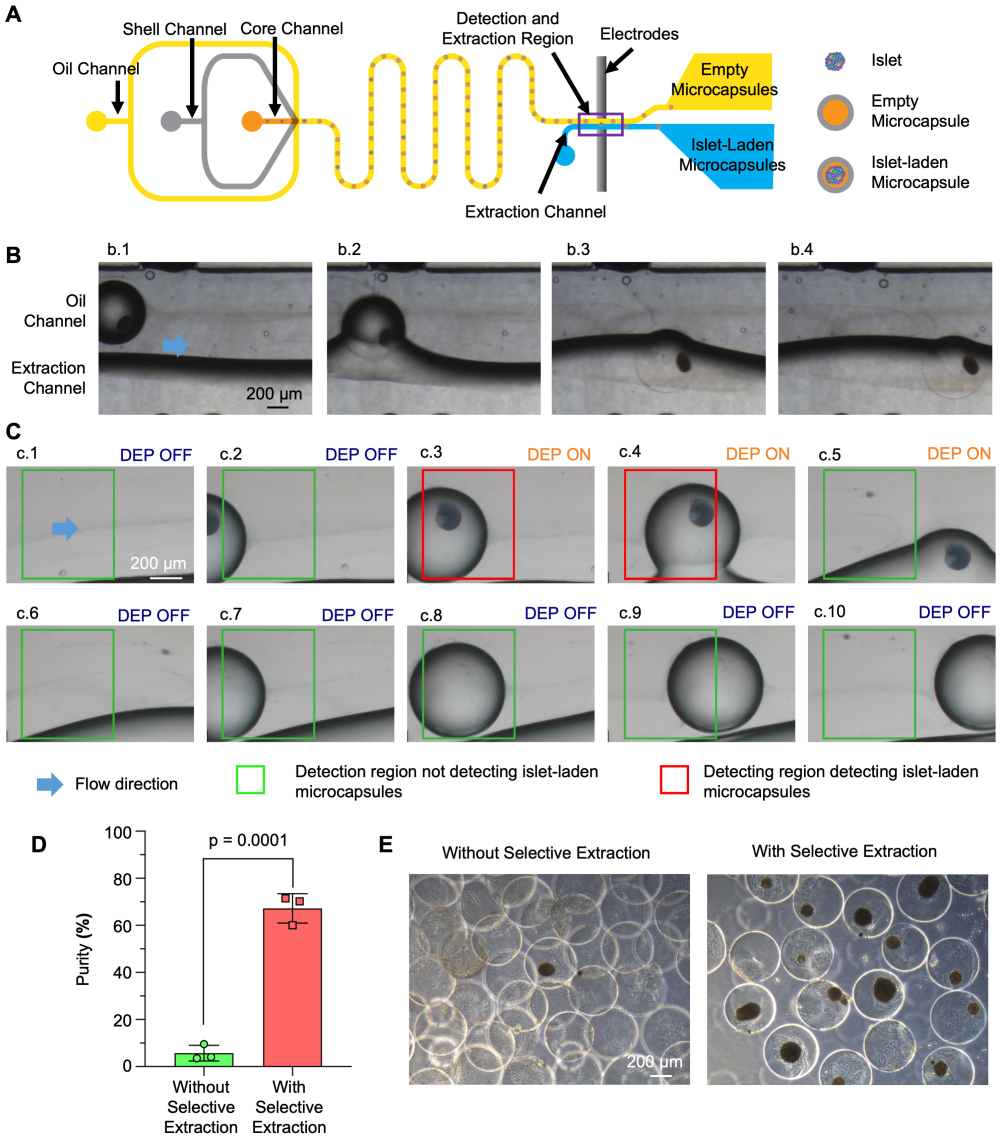

Figure 4.4. Deep learning-based detection and extraction of microencapsulated islets. (**A**) Schematic illustration of the microfluidic device depicting empty microcapsules and islet-laden microcapsules flowing down the gelling channel and being extracted to the extraction channel or continuing down the oil channel. The purple box indicates the area where detection and extraction take. (**B**) Phase contrast video frames of microcapsule being extracted with DEP from the oil emulsion to the extraction solution. The microcapsule moves from left to right towards the extraction region (b.1). When the microcapsule reaches the extraction region and DEP turns on (b.2), the microcapsule is pushed towards the extraction channel. Once the microcapsule touches the aqueous-based extraction solution, it is pulled into the

extraction channel (b.3), and then the intact microcapsule continues to flow down the extraction channel (b.4) where it is collected. (**C**) Video frame sequence illustrating the microcapsule detection and extraction process. An islet-laden microcapsule moves towards the detection region (c.1-c.2). Upon entering the detection region, the detection system identifies a microcapsule containing an islet, marked by a red box, and activates DEP (c.3) The microcapsule proceeds into the extraction region (c.4) where DEP pushes it from the oil emulsion into the extraction solution (c.5) and the microcapsule advances down the extraction channel for collection. DEP is deactivated (c.6). An empty microcapsule moves into the detection region without islet detection (c.7-c.8) and DEP remains inactive (c.9). The empty microcapsule continues to flow down the oil channel (c.10). (**D**) Purity of microcapsules with and without selective extraction. n = 3 independent runs. (**E**) Images showing the purity of microcapsules without selective extraction and with selective extraction.

Phase contrast is used in **Figure 4.4B** and **Supplemental Video 4.1** to show the extracted microcapsule in the aqueous-based extraction solution more clearly and show that the microcapsule is still intact. A video taken in bright field, the mode used for training the detection model and performing real-time microcapsule extraction, can be seen in **Supplemental Video 4.2.** In **Figure 4.4B**, **Supplemental Video 4.1** and **Supplemental Video 4.2**, the islet-laden microcapsules are extracted by manually turning on and off DEP so that both the channels can be shown using the 4x objective on the microscope which cannot be done while using the deep learning detection system, which requires the 10x objective. Manually toggling the voltage supply for DEP on and off results in multiple microcapsules coming into contact with the extraction solution, as observed in **Supplemental Video 4.1** and **Supplemental Video 4.2**. This is in contrast to controlling DEP with the use of the switch and the detection system, which can extract one microcapsule at a time.

The deep learning code trained on the planar device with MCF-7 aggregates from Chapter 3 is successfully used for the detection of microencapsulated islets in the non-planar core-shell hydrogel microcapsule fabricating device. A video frame

breakdown of detection and extraction can be seen in **Figure 4.4C**. **Supplemental Video 4.3** shows the detection and extraction at full speed, and **Supplemental Video 4.4** at 10% speed for better visualization. The efficiency of the system is 79.8 ± 1.1% and is calculated using equation 3.2. The efficiency is not as high as the efficiency in Chapter 3, likely due to the microcapsules being larger than the microcapsules in the planar device, making islets appear out of focus more often. Most islets the system does not detect are located at the periphery of the microcapsule or are out of focus.

The sample purity is calculated using equation 3.3. Without selective extraction, the purity is approximately 5% (**Figure 4.4D**), and with selective extraction, the purity is approximately 70% (**Figure 4.4E**). A lot of false positive microcapsules are detected due to the debris in the microcapsules being detected as if it were islets. Debris is much more prominent during islet encapsulation compared with MCF-7 aggregate encapsulation, which the model is trained on. This large number of false positive islets leads to a lower purity sample. This can be improved by more training with images of debris, but this also may reach the limit of the MobileNets system; therefore, a higher resolution system should be used[17,108,204,205].

4.3.5. In vitro microcapsule and characterization of islet-laden microcapsules

Islet viability and function after culturing are examined to determine the positive effects that encapsulation may have in vitro and ensure that function is not decreased due to the encapsulation process. Core-shell hydrogel microcapsules, conventional alginate microcapsules, and islets that are not encapsulated (free islet control) in suspension culture are cultured for up to 4 weeks in a humidified incubator at 37ºC with 5% CO_2.

After isolation, the islets are encapsulated using the non-planar microfluidic device with flow rates described in **Figure 4.1B**. After encapsulation, islets are cultured in Medium 199 supplemented with 10% FBS and 1% P/S media because culturing the microcapsules in RPMI media leads to the eventual dissolution of alginate in microcapsules, presumably due to the phosphate content of RPMI[206].

The health of core-shell hydrogel encapsulated, alginate microcapsule-encapsulated, and free islets in suspension culture are evaluated using fluorescent staining and GSIS. A range of islet sizes between 50 μm and 350 μm are evaluated. After 1 week of culture, viability is assessed per the cell membrane integrity using PI. Subsequently, the stained islets are imaged red fluorescence and quantified for viability using ImageJ to determine the percentage of cells that contain PI (and have damaged membranes).

Staining of whole islets with PI and annexin V is performed because it is a widely used method for quantifying dead and apoptotic cells[207]. PI can penetrate islets, enabling staining throughout the islets and detection of necrotic cores that may form[208]. While flow cytometry was considered for quantifying cell viability, the cells were found to have an increased amount of apoptosis after dissociation, aligning with findings in previous studies[209,210]. Consequently, staining intact islets with PI and annexin proved to be the most effective method for determining cell viability and apoptosis.

Representative images of islets stained with PI after 1 week and 4 weeks of culturing can be seen in **Figure 4.5A.** As seen in **Figure 4.5B**, at 1 week the mean viability of islets in all groups is above 95% and there is no significant difference

between groups. After 4 weeks of culture, islets encapsulated in core-shell hydrogel microcapsules 93.5 ± 5.3%, islets encapsulated in alginate microcapsules have a viability of 86.9 ± 6.0 % and free islets have a viability of 79.2 ±12.6%. While the difference between these groups is not statistically significant, the core-shell hydrogel encapsulation leads to the highest cell viability out of the groups, and $p = 0.1460$ compared to the free islet group. This improvement of the core-shell hydrogel microencapsulated islets could be due to the collagen in the core being a more favorable microenvironment, which has been shown to improve islet viability[181,185].

The effects of encapsulation on apoptosis are also examined at 1 and 4 weeks by staining islets with annexin V. Annexin V stains for phosphatidylserine residues, which translocate to the surface of the cell membrane during apoptosis[211]. Images of islets are taken, and the mean gray value of the fluorescence is quantified using ImageJ.

Representative images of islets stained with annexin V can be seen in **Figure 4.5C**. **Figure 4.5D** shows annexin V fluorescence intensity at 1 and 4 weeks of culture. After 1 week, the mean gray value for free islets is 1.78 ± 1.21, alginate microencapsulated islets is 3.01 ± 1.45, and core-shell hydrogel microencapsulated islets is 2.27±0.82. At week 4 the fluorescence intensity increases over all groups and islets have a mean gray value of 5.12 ± 3.76, 5.74 ± 1.18, and 4.39 ± 1.97 for free, alginate encapsulated, and core-shell hydrogel encapsulated islets, respectively. While the values are not significantly different, it is also important to note that the encapsulation process and culturing in microcapsules does not negatively affect viability or increase apoptosis. Representative images of encapsulated islets at 1 week and 4 weeks are shown in **Figure 4.5E**. Islets in both the alginate and core-shell

hydrogel microcapsules look healthy over 4 weeks of culture, displaying a similar morphology.

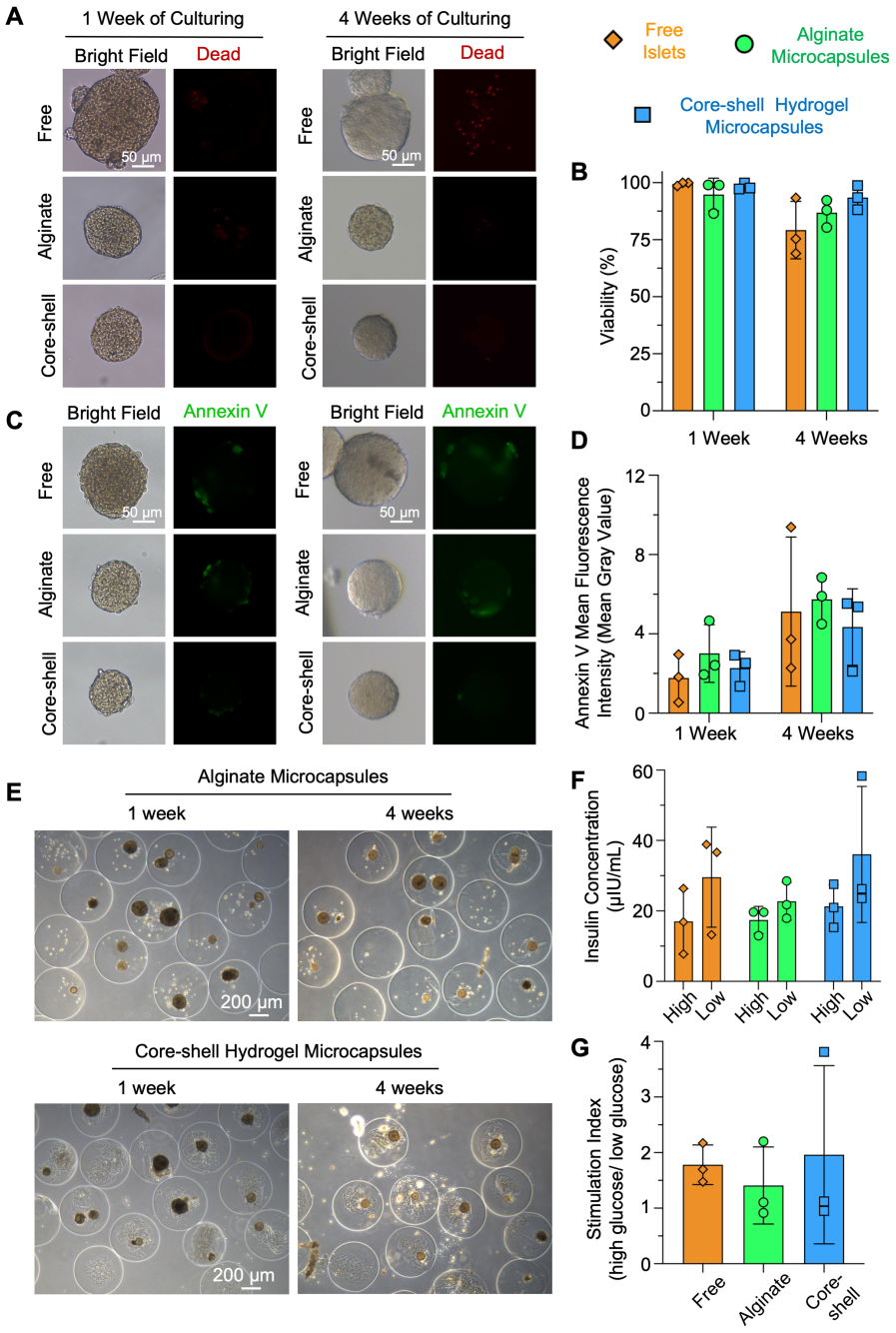

Figure 4.5. Characterization of encapsulated islets after in vitro culture. (**A**) Representative images of islets stained using PI after 1 week and 4 weeks of culturing. (**B**) Islet viability assessed per bright field and PI image analysis after 1 week and 4 weeks of culturing. n = 3 independent runs with approximately 7 islets per trial. (**C**) Representative images of islets stained with annexin V after 4 weeks of culture. (**D**)

Apoptosis assessed per annexin V staining quantification using mean gray value of islet images after 1 week and 4 weeks of culturing. n = 3 independent runs with approximately 7 islets per trial. (**E**) Representative images of islets encapsulated in alginate microcapsules and core-shell hydrogel microcapsules at 1 and 4 weeks of culture. (**F**) Insulin concentration per well of islets after 14 days of culturing during GSIS with LGS and LGS in micro insulin units (μIU) per mL. n = 3 independent runs with approximately 20 IEQ per run. (**G**) Simulation index (HGS insulin release / LGS insulin release) of islet groups after 14 days of culture using GSIS assay. n= 3 independent runs with approximately 20 IEQ per run.

A GSIS assay is performed on the islet groups to compare their ability to stimulate glucose after 2 weeks of culturing. No significant differences are observed between the groups in terms of the total concentration of insulin released (**Figure 4.5F**) or the stimulation index (**Figure 4.5G**). This indicates that the microcapsules do not prevent insulin secretion. The stimulation index is calculated by dividing the amount of insulin secreted under HGS conditions by that under LGS conditions. The average stimulation index is greater than 1 for all groups, meaning the islets are healthy and respond to glucose stimulation[207].

In summary, there is no significant difference between islets viability at 1 week of culturing, but at 4 weeks of culturing, core-shell hydrogel microcapsules have the highest viability. This indicates that core-shell hydrogel encapsulation may have positive health effects for islets in vitro and should be measured in vivo. While there is no significant difference in insulin secretion between groups, is it important to note that the microcapsules do not impede glucose stimulation and insulin release when compared to free islets in suspension culture, which is important for further testing in vivo.

4.3.6. Islet transplantation process and bioluminescent islet for tracking islets in vivo

Figure 4.6A illustrates the islet transplantation site located in the upper left side of the mouse's peritoneal cavity. **Figure 4.6B** shows the steps for islet transplantation using images from **Supplemental Video 4.5**. As shown in the figure, the mouse (anesthetized) skin near the transplantation site is pinched using tweezers, and the needle is carefully inserted into the IP cavity. Then, the islets are injected intraperitoneally into the mouse, and the needle is removed. This injection method requires little to no recovery time for mice and no need for large incisions and suturing.

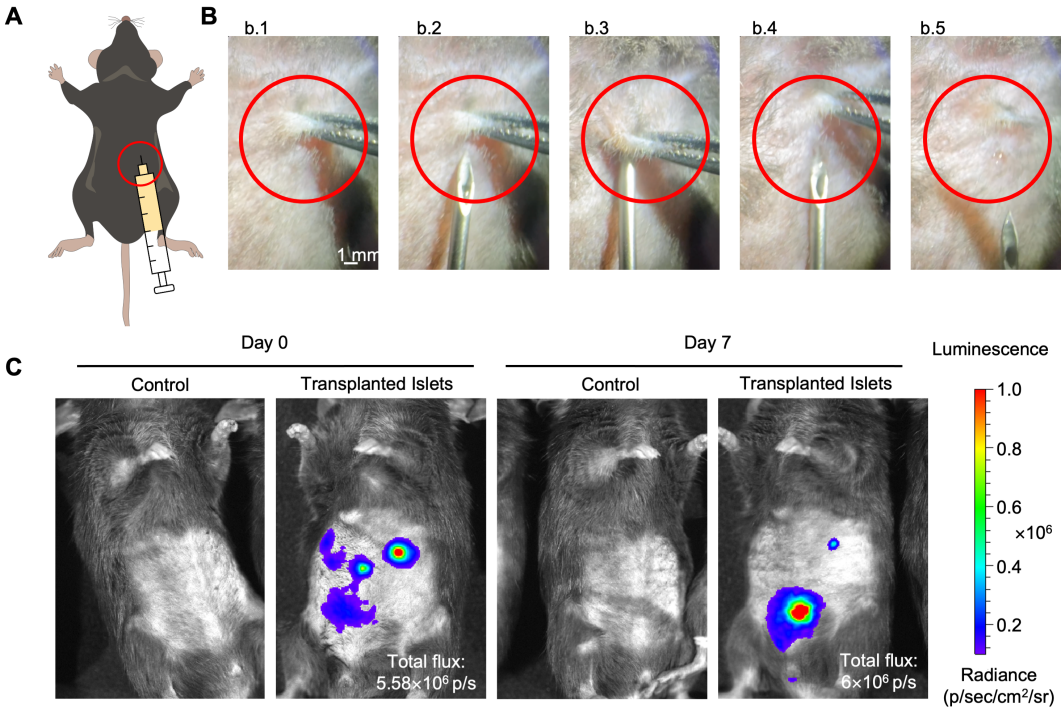

Figure 4.6. Overview of the islet transplantation process and IVIS imaging of bioluminescent islets in vivo. (**A**) Schematic illustration of the site (red circle) of transplantation via needle injection into the IP cavity. (**B**) Images from a video of transplantation into the IP cavity using an 18 g needle. Tweezers are used to pinch the mouse skin at the transplantation size (b.1). Then the needle is inserted into the IP cavity and the islets are injected through the needle (b.2 and b.3). The needle is then removed from the transplantation site (b.4 and b.5). (**C**) IVIS imaging of transplanted

luciferase positive free islets isolated from L2G85 in C57BL/6 mice. Control mice with a saline injection and mice with 400 islets transplanted IP imaged at day 0 and day 7 post-transplantation, and the total flux values of mice based on image analysis.

After isolation from L2G85 mice, 400 free luciferase islets are transplanted into C57BL/6 mice. Control mice receive a saline injection (**Figure 4.6C**). Bioluminescence activation is achieved by injecting the mice with D-luciferin. Then, 15 minutes after D-luciferin injections, the mice are imaged using IVIS. On day 0, islets are visible at the injection site and in other areas of the IP cavity, indicating that the islets did not remain solely at the transplantation site (**Figure 4.6C**). There is no noticeable decrease in bioluminescence 1 week post-transplantation, showing a total flux of 5.58×10^6 p/s and 6×10^6 p/s on days 0 and 7, respectively. This suggests that the islets remain alive one week after transplantation, although the bioluminescent signal indicates that almost all the islets migrate to the lower region of the IP cavity. The movement of islets could be due to the mice standing on their hind legs leading to a migration of the islets downward over time.

4.3.7. Islet transplantation into syngeneic diabetic mouse model shows superior blood glucose control for core-shell hydrogel encapsulated islets

Islets isolated from C57BL/6 mice are transplanted into diabetic C57BL/6 mice to investigate if islets encapsulated in core-shell hydrogel microcapsules can enhance the treatment of T1D in a syngeneic diabetic mouse model. Initial experiments determine an IP injection of 150 mg/kg STZ is effective for diabetes induction. The transplantation procedure involves IP injection using an 18-gauge needle as shown in **Figure 4.6A** and **Figure 4.6B**.

It is determined that transplantation of approximately 1400 IEQ lowers blood glucose levels of mice compared to the negative control (diabetic mice without transplanted islets). The schematic in **Figure 4.7A** shows the timeline for the syngeneic transplantation, monitoring, and characterization process. The mice are considered diabetic after two consecutive days of blood glucose levels exceeding 300 mg/dL, which occurs approximately 5 days after STZ injection. Islet transplantations are carried out when the mice are between 8 and 12 weeks old[212,213]. The mice are anesthetized, and islets are transplanted using the method in **Figure 4.6B**. Blood glucose levels are monitored three times a week. These experiments include the use of four groups: diabetically induced mice transplanted with islets in core-shell hydrogel microcapsules, diabetically induced mice transplanted with islets in alginate microcapsules, diabetically induced mice without islet transplantation (negative control group), and normal mice that are not diabetically induced mice (positive control group).

The results indicate that core-shell hydrogel microcapsules outperform alginate microcapsules, resulting in lower blood glucose levels (**Figure 4.7B**). A significant difference in the area under the curve (**AUC**) between core-shell hydrogel microcapsules and alginate microcapsules as well as the core-shell hydrogel and negative control (**Figure 4.7C**) is observed.

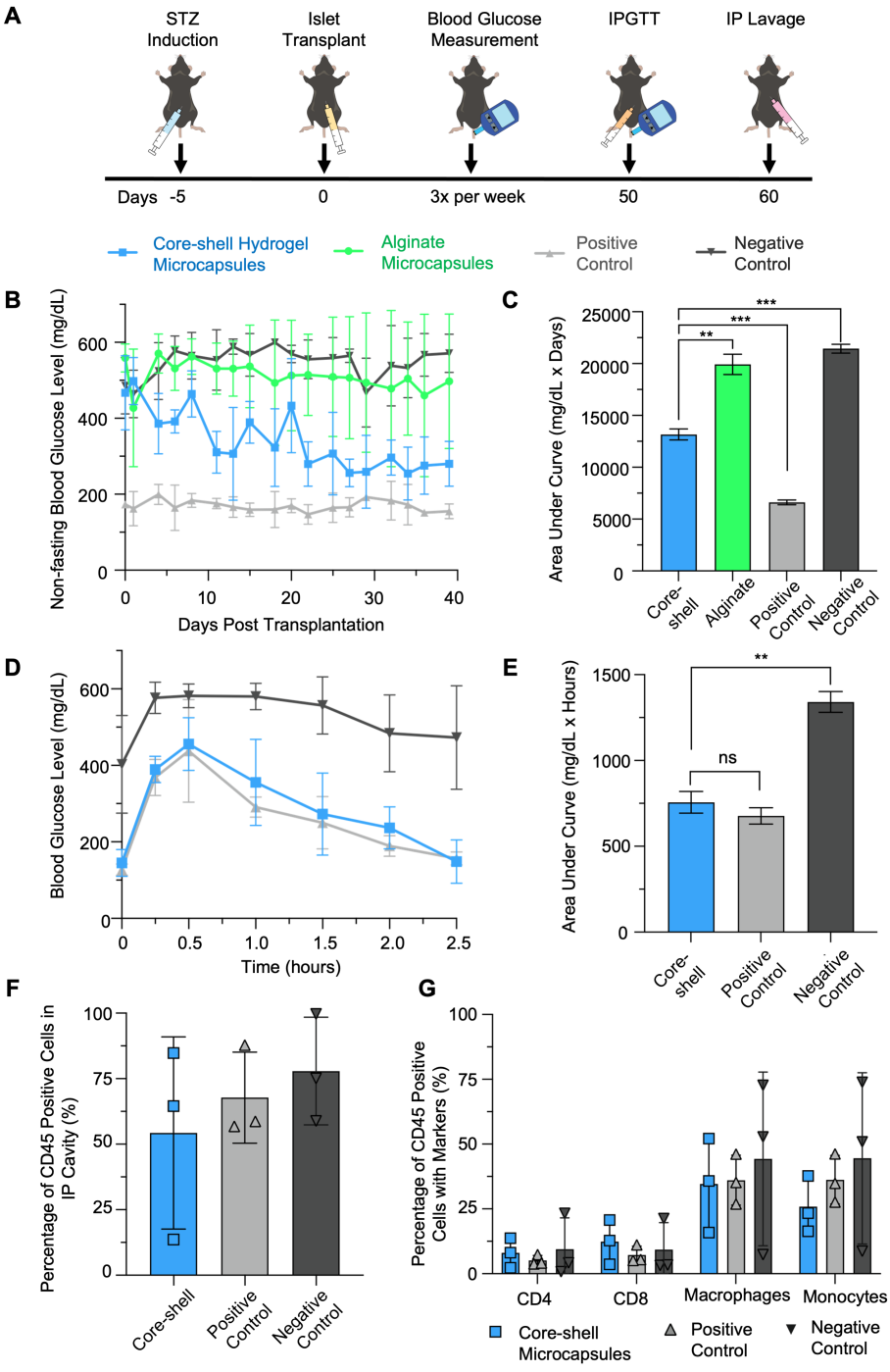

Figure 4.7. In vivo blood glucose transplantation, monitoring, and immune response quantification. (**A**) Schematic overview of the timeline for transplantation, blood glucose monitoring, and immune cell evaluation. (**B**) Non-fasting blood glucose levels of mice transplanted with alginate encapsulated islets or core-shell hydrogel encapsulated islets. n = 3. (**C**) AUC for graph **B** of mouse blood glucose levels over 40 days. (**D**) IPGTT for mice at approximately day 50. n= 3. (**E**) AUC for IPGTT graph.

(**F**) Percent of CD45 positive cells out of total cells collected from the IP cavity. n = 3. (**G**) Percent of CD45 positive cells with varying immune cell markers. n = 3. *p < 0.05, **p < 0.01, ***p < 0.001.

While the positive control is significantly lower than the core-shell hydrogel encapsulated islets, this could likely be improved by increasing the number of transplanted islets. These results are similar to other studies showing that the conventional homogeneous alginate microcapsules perform poorly during syngeneic transplantation compared with better engineered microcapsules[93].

The improved performance of core-shell hydrogel microcapsules can be attributed to multiple reasons, including islet interactions with the collagen in the core. Collagen was chosen because it is a major component of the ECM and has been found to be helpful for improving islet health and insulin secretion after transplantation[78,214]. Collagen type I is the most prevalently used type of collagen in tissue engineering and is used for islet encapsulation in part due to its abundance in the body and ability to form a stable gel at physiological conditions (temperature of 37ºC and neutral pH)[181,215,216]. Collagen can facilitate cell-cell interactions and adhesion with alginate, which is important for proper functioning[217]. Studies have also found that using a combination of collagen and alginate results in islets having high viability[181,218]. Alginate improves the stiffness of collagen, making it more like a tissue microenvironment because collagen on its own can have poor mechanical properties and alginate has been used to tune these properties[188,189].

The alginate microcapsules also contain, on average, more islets per microcapsule than the core-shell hydrogel microcapsules, as seen in **Figure 4.5E**. This is likely due to the difference in viscosity of the solutions, which leads to more

clumping in the lower viscosity alginate solution. During the scaling-up process, these differences are exacerbated and can lead to three or more islets in a microcapsule. The high viscosity of the collagen-based core ensures even distribution of islets, with most microcapsules containing one islet and some containing two. Studies show that islets clumping together in devices decreases the amount of oxygen that reaches them and can hinder insulin secretion. This potentially contributes to the superior performance of core-shell hydrogel microcapsules over alginate microcapsules[179,219].

At approximately 50 days post-transplantation, an IPGTT is conducted by injecting mice with a glucose solution (**Figure 4.7D**). The results show no significant difference in the AUC (**Figure 4.7E**) between the transplanted core-shell hydrogel encapsulated islets and the positive control group (non-diabetic mice), while a significant difference is observed between the core-shell hydrogel group and the negative control group (diabetic mice with no islets transplanted). These results indicate that the core-shell islets effectively respond to glucose at the same rate as healthy mice while lowering it more effectively than the negative control. The alginate mouse group is not measured because they died before day 50. For the negative control, approximately half of the mice die before day 50, and measurements are taken from the mice that were still healthy at 50 days.

4.3.8. Immune response to microcapsule transplantation

Transplantation of foreign materials can induce a host immune response, leading to eventual rejection of the islets[191,220,221]. At the conclusion of the in vivo experiments (around day 60), the immune response in the IP cavity is quantified. IP lavage is conducted, and the collected cells are stained and analyzed using flow

cytometry[191]. These cells are stained for immune cell markers, including CD45 as a general immune cell marker, CD11b for monocytes, F4/80 for macrophages, CD4 for helper T cells and regulatory T cells, and CD8 for cytotoxic T cells[222,223]. Flow cytometry data analysis is performed using FlowJo. Initial gating is performed to eliminate cell fragments and debris from the sample set.

As shown in **Figure 4.7F,** there are no significant differences in the percentages of CD45-positive cells between the groups, indicating that core-shell hydrogel microcapsules do not increase the proportion of leukocytes in the IP cavity. Further analysis shows the percentage of CD45 positive cells with CD4, CD8, monocyte, and macrophage markers. No significant differences are observed in the CD4 and CD8 staining percentages between the groups, suggesting that transplantation did not affect T cell responses (**Figure 4.7G**). Furthermore, there are no significant differences in the percentages of monocytes and macrophages among the groups. These findings suggest that core-shell hydrogel encapsulated islets do not increase the percentage of leukocytes in the IP cavity and do not alter the types of leukocytes present[191]. Given the positive in vivo results, it is recommended to assess these core-shell hydrogel microcapsules in allotransplantation and xenotransplantation studies to further explore their potential for preventing immune responses and treating diabetes in vivo.

The microcapsules could not be retrieved from the mice after the conclusion of in vivo experiments, possibly due to the lack of clumping that microcapsules experience, making it difficult to locate individual microcapsules. Moreover, individual microcapsules may have been hidden in the tissue and lower abdomen, making them even more challenging to identify. This is a limitation of this study. Ideally, the samples

could be retrieved and analyzed for immune cell buildup and fibrotic growth on the microcapsules. Additionally, the islets could be examined for cell viability and glucose responsiveness. This removal issue could be addressed by considering alternative transplantation areas, such as the epididymal fat pad or subcutaneous transplantation. Alternatively, microcapsules could be retrieved for quantification possibly at an earlier time point.

4.4 Conclusion

This research demonstrates the advantages of islet microencapsulation using a non-planar microfluidic device to fabricate core-shell hydrogel microcapsules. This microfluidic device not only allows for the use of collagen in the microcapsule core to create a more tissue-like microenvironment, but also enables on-chip microcapsule sorting. Using a deep learning-based detection system created in Chapter 3, islet-laden microcapsules are sorted into an aqueous-based extraction solution, removing them from the empty microcapsules and leading to a highly pure microcapsule sample when compared with non-selective extraction. In vitro, core-shell hydrogel encapsulated islets show improved viability compared with conventional homogeneous alginate microcapsules. Syngeneic core-shell hydrogel microencapsulated islet transplantation in a diabetic mouse shows improvements over traditional alginate microcapsules, lowering the blood glucose levels over a 40 day time period and successfully responding to glucose 50 days post-transplantation. These findings highlight the potential of core-shell hydrogel microcapsules as a promising tool for islet transplantation. By continuing to explore these areas, the field of islet transplantation can move closer to providing more effective treatments for type 1 diabetes.

Chapter 5 : Nanoencapsulation of Hydrophobic Antioxidant for Enhanced Delivery into Islets and Improved Islet Viability

5.1 Introduction

Islet transplantation is a promising treatment for type 1 diabetes, but the islet isolation process can damage tissue, reducing viability and increasing susceptibility to cell death and functional decline over time. Furthermore, islets undergo post-transplantation hypoxia, which can result in the death of up to 70% of islets[21,22]. It is crucial to maintain highly viable and healthy islets to ensure continued blood glucose regulation post-transplantation. During the isolation process, islets are removed from their native pancreatic environment, blood vessels, and their source of nutrients and oxygen [224]. These events can lead to the generation of reactive oxygen species (**ROS**), oxidative stress, and eventually apoptosis[225,226]. In addition to cell death from post-transplantation oxidative stress, immune rejection also leads to reduced islet function[152,227]. Given the precious nature of islets, extensive research involving the use of antioxidants has been conducted to mitigate this issue using antioxidants with promising outcomes. However, some antioxidants that could be highly beneficial for treatment are hydrophobic at physiological pH, making their uptake into islets challenging and often necessitating the use of organic solvents such as dimethyl sulfoxide (**DMSO**) that may harm islet health[228].

Bilirubin, a potent antioxidant, has long been recognized for its potential to combat oxidative stress. It has been shown to reduce oxidative damage and enhance cell viability under various conditions[229,230]. Bilirubin also upregulates the expression

of anti-apoptotic protective genes, including heme oxygenase (**HO-1**) and B-cell lymphoma 2 (**BCL-2**)[154,231]. In addition to its role in mitigating the harmful effects of ROS, bilirubin exhibits anti-inflammatory properties, suppressing the release of damage-associated molecular patterns (**DAMPs**) and cytokines[151,152,231]. It downregulates pro-apoptotic genes, preventing the release of cytokines such as tumor necrosis factor-alpha (**TNF-α**) and Interleukin-1 beta (**IL-1β**) which help prevent immune rejection ending in islet death. However, the full therapeutic potential of bilirubin is hindered due to its hydrophobic nature when dissolved in aqueous solution like culture medium which makes it difficult to be taken up by cells. Bilirubin has been investigated in multiple studies for its protective effects on islets[151,232]. Due to its hydrophobic and insoluble nature at physiological pH, bilirubin nanoparticles are used to improve its effects on islets by enhancing uptake[154,228]. However, the extent to which nanoparticles facilitate bilirubin penetration into islets has not yet been thoroughly investigated.

Curcumin, a polyphenolic compound derived from turmeric, is another molecule that has demonstrated antioxidant and anti-inflammatory effects, making it a promising candidate for improving the outcomes of islet transplantation[233-235]. Like bilirubin, curcumin can scavenge ROS, modulate immune responses, reducing cell damage[234,236]. Research shows that curcumin has protective effects on islets, and micelle-encapsulated curcumin was shown to increase curcumin uptake in vitro in an insulinoma cell line[237]. Another study found that nanoencapsulated curcumin decreases damage to islets caused by STZ in vivo[238]. Although curcumin has been shown to have

protective effects on islets, the effects of curcumin nanoparticles on islets under hypoxia in vitro have not yet been investigated.

Poly(lactic-co-glycolic acid) (**PLGA**) is a copolymer composed of polylactic acid (**PLA**) and polyglycolic acid (**PGA**) approved by the U.S. Food and Drug Administration (**FDA**) for drug delivery and is widely used to encapsulate and deliver molecules and drugs into cells[239-241]. It is biocompatible, biodegradable, and its release profiles can be adjusted by the ratio of PLG to PGA[242]. Pluronic F-127 (**PF-127**) is a triblock copolymer composed of poly(ethylene oxide)-b-poly(propylene oxide)-b-poly(ethylene oxide) (PEO-PPO-PEO) that is also FDA approved for pharmaceutical use[243-245]. PF-127 is a surfactant and forms micelles in oil-in-water emulsions with hydrophobic cores[246,247]. Research has found that using PLGA and PF-127 together leads to more stable and uniform nanoparticles than using either of them on their own[248]. Chitosan, a naturally occurring polymer derived from crustacean shells, has been shown to enhance nanoparticle uptake into cells. Chitosan can increase nanoparticle stability and charge, as well as adhere to glycoproteins, thereby improving cellular uptake[249-252]. The use of these polymers to encapsulate hydrophobic molecules has the potential to help improve their uptake into cells.

This chapter investigates the nanoencapsulation of hydrophobic antioxidants in PF-127-PLGA (PFP) nanoparticles coated with chitosan to evaluate its potential to enhance their uptake by cells. Our data demonstrates that PFP-chitosan nanoparticles effectively penetrate MCF-7 cells, insulinoma cells, and islets, significantly increasing antioxidant uptake compared to free hydrophobic molecules. Furthermore, our results

indicate that bilirubin and curcumin reduce apoptosis in islets exposed to hypoxia in vitro.

5.2 Materials and methods

Materials for cell culture were purchased from Thermo Fisher Scientific and chemicals were obtained from Sigma unless otherwise stated.

5.2.1. Cell culture

Normoxic cell culture was conducted at 37°C in a humidified incubator with 5% CO_2. MCF-7 cells were cultured in DMEM supplemented with 10% heat inactivated FBS and 1% P/S. When the cells reached approximately 80% confluency, they were detached using 0.25% trypsin-EDTA. After washing twice with PBS at 200 g, the cells were counted using a hemocytometer for subsequent use. Beta-TC-6 cells from ATCC were cultured in DMEM supplemented with 15% FBS and 1% P/S. Upon reaching approximately 70% confluency, floating cells were collected and attached cells were detached using 0.25% trypsin-EDTA. Floating and attached cells were combined and washed twice with PBS by centrifuging at 200 g for 3 minutes. Cell counts were determined using a hemocytometer for further use.

5.2.2. Nanoparticle synthesis

A schematic illustration of the nanoparticle synthesis process can be seen in **Figure 5.1A**. First, 1 mg of bilirubin, 5 mg of Pluronic F-127 (PF-127), and 15 mg of PLGA 75:25 (polylactic acid: polyglycolic acid) were added to a 1.5 mL microcentrifuge tube. 1 mL of dichloromethane (**DCM**) was then added to the microcentrifuge tube. The mixture was sonicated in a Fisher Scientific Ultrasonic Bath

and pipetted until fully dissolved. The resulting solution was transferred to a scintillation vial, and an additional 1 mL of DCM was added, followed by another round of sonication in the Ultrasonic Bath.

A 2% poly(vinyl alcohol) (**PVA**) solution (30 to 70 kDa) was created by dissolving PVA in water by continuously stirring over 3 hours at 80 °C. In another scintillation vial, 6 mL of the 2% PVA solution was prepared. The polymer/DCM solution was then added dropwise to the PVA solution using a 2 mL serological pipette. The resulting mixture was sonicated using a Branson 450 Digital Sonifier at 22% power for 1 minute to create an oil in water emulsion.

The solution was then transferred into a 250 mL round-bottom flask and placed on a Heidolph (Schwabach, Germany) Hei-VAP rotary evaporator with a rotation speed of 60 rpm and a temperature of 37 °C for 1 hour. Afterward, the solution was divided into 1.5 mL microcentrifuge tubes and centrifuged at 17,500 g for 10 minutes. The supernatant was aspirated off and nanoparticles were resuspended in DI water and centrifuged again at 17,500 g for 10 minutes.

The nanoparticles were resuspended in 2 mL of DI water and transferred to a scintillation vial. Here, 3 mL of a chitosan coating solution was added. The chitosan solution was prepared by dissolving 30 g of low molecular weight (50 kDa to 190 kDa) chitosan in 40 mL of 2% PVA containing 170 µL of acetic acid. The nanoparticles and coating solution were stirred overnight on a stir plate. Subsequently, the solution was filtered through a 45 µm syringe filter to eliminate excess chitosan. Finally, it was transferred to 1.5 mL microcentrifuge tubes, centrifuged at 17,500 g, and resuspended in DI water twice. For curcumin nanoparticle synthesis the same process was used,

starting with the addition of 1 g of curcumin to the initial polymer solution. The same steps were repeated for coumarin 6 nanoparticles, except for adding 0.5 g of coumarin 6 to the initial polymer solution.

5.2.3. Nanoparticle characterization

Size, zeta potential, and polydispersity index (**PDI**) were characterized using a Malvern Panalytical (Malven, United Kington) Nano-ZS Zetasizer. A Spark Multiplate Reader was used to quantify concentrations of bilirubin, curcumin, and coumarin 6. Absorbances of 454 nm and 425 nm were used for quantifying bilirubin and curcumin, respectively. A fluorescent excitation wavelength of 457 nm and an emission wavelength of 501 nm were used to quantify coumarin 6 concentrations.

Bilirubin release experiments were performed by suspending bilirubin nanoparticles in 1 mL of a 10% FBS in PBS solution in a 1.5 mL microcentrifuge at a concentration of 20 μM bilirubin. The microcentrifuge tubes were then placed in a water bath at 37°C. At each designated time point, the nanoparticle suspension was centrifuged at 17,500 g, and the top 800 μL of the solution was collected and replaced with 800 μL of fresh 10% FBS in PBS solution. The nanoparticles were resuspended and returned to the water bath. After 72 hours of release, the nanoparticles remaining in the microcentrifuge tubes were dissolved in DMSO to determine the amount of unreleased bilirubin. Bilirubin released over time was quantified using a Spark Multimode Microplate Reader.

Transmission electron microscope (**TEM**) nanoparticle imaging was performed by adding one drop of 100 μg/mL nanoparticle suspension to a 200-mesh Ted Pella (Redding, CA, USA) copper grid. The nanoparticles were stained with a 2% uranyl

acetate solution washed with DI water. After drying in a chemical fume hood, imaging was conducted using a JEOL (Akishima, Tokyo, Japan) JEM 2100 LaB6 TEM.

Nanoparticles were freeze-dried to determine encapsulation efficiency and loading content. They were placed in 1.5 mL microcentrifuge tubes and in a -80°C freezer for an hour. Next, they were removed from the freezer, and a hole was poked in the top of the microcentrifuge tube using a 20-gauge needle to allow moisture to escape. They were then placed in a 50 mL conical centrifuge tubes, and a Kimwipe was placed on top of the 50 mL conical centrifuge tube (without a cap) and secured with a rubber band to allow moisture to escape. The 50 mL conical centrifuge tubes were subsequently placed in a Labconco FreeZone 6 L Console Freeze Dryer using the settings of -80°C and 0.230 mbar for a minimum of 36 hours. The encapsulation efficiency and loading content were determined by weighing the lyophilized nanoparticles, dissolving them in DMSO, and quantifying antioxidant concentrations using a Spark Multimode Microplate Reader. Freeze dried nanoparticles were only used for nanoparticle characterization, and all other experiments were conducted using freshly synthesized nanoparticles.

5.2.4. Bilirubin nanoparticle uptake into MCF-7 and Beta-TC-6 cells

MCF-7 cells were cultured as described in 5.2.1. To prepare the culture slides, 12 mm round glass coverslips were coated with a 1:100 dilution of 3.82 mg/mL type I collagen (Corning) in PBS for 30 minutes. Subsequently, MCF-7 cells were seeded onto the slides at a concentration of 30 x 10^4 cells/mL and cultured overnight in a humidified incubator at 37ºC with 5% CO_2. Cells were then cultured with media containing 20μM free bilirubin or 20μM nanoencapsulated bilirubin for 3 hours in a

humidified incubator at 37ºC with 5% CO_2. Cells were washed with PBS and incubated with Lysotracker Red DND-99 (Thermo Fisher Scientific) at a dilution of 1:500 in media for 30 minutes. Cells were then washed again with PBS and fixed using 4% paraformaldehyde (**PFA**) in PBS for 15 minutes. Cells were then washed again with PBS and stained with DAPI was added at a 1:1000 dilution in PBS for 10 minutes. The cells were washed with PBS and mounted on a 25 mm x 75 mm x 1 mm microscope slide for imaging using CC/Mount mounting medium, and imaged using a Zeiss LSM 710 confocal microscope. An excitation of 488 nm and emission range of 500-560 nm were used to image bilirubin. Beta-TC-6 cells were added to collagen-coated slides at a concentration of 12 x 10^4 cells/mL and cultured in a humidified incubator at 37ºC with 5% CO_2 for 3 days before uptake experiments. All other procedures remained consistent with those used for the MCF-7 cells.

5.2.5. Islet isolation

Islets were isolated using the methods described in Chapter 4. In brief, islets were isolated from C57BL/6 mice using a collagenase solution consisting of 1.5 mg/mL collagenase D and 2 mg/mL BSA in HBSS. After perfusion of the pancreas, the tissue was digested, and a gradient of histopaque was used to separate the islets from other pancreatic tissue. The isolated islets were cultured in RPMI supplemented with 10% heat inactivated FBS and 1% P/S.

5.2.6. Nanoparticle penetration islets

Approximately 50 islets per well were placed in a 24-well ultralow attachment plate and incubated with media containing 8 µM free coumarin 6, 8 µM

nanoencapsulated coumarin 6, or no coumarin 6 for 6 hours. Islets were washed twice with media by centrifugation at 70g. The islets were fixed for 30 minutes using 4% PFA and placed in a 20% sucrose solution overnight.

A mold for cryosectioning samples was created by cutting a circle with a diameter of 10 mm out of a 30 mm x 20 mm by 5 mm slab of PDMS and placing it on a 25 mm x 75 mm x 1 mm microscope slide. PDMS slabs were made using the methods described in Chapter 3. The islets were pipetted onto the glass slide and placed in a -80°C freezer for 5 minutes. The slide was removed from the freezer, and Sakura Finetek (Torrance, CA, USA) Tissue-Tek O.C.T. compound was added on top of the islets to fill the PDMS mold. The mold was then placed back in the -80°C freezer for 20 minutes.

The islets were cryosectioned using a Leica Biosystems (Heidelberger, Germany) CM1950 Cryostat to obtain 8 μm thick slices. These slices were collected onto Electron Microscopy Sciences (Hatfield, PA, USA) Millennia 2.0 Adhesion microscope slides. The slices were stained with a 1:1000 dilution of DAPI in PBS and incubated at room temperature for 10 minutes. Afterward, the slices were washed twice with PBS, and a cover slip was added using CC/Mount. Finally, the slices were imaged using a Zeiss LSM 710 microscope using fluorescence microscopy. Blue fluorescence was used for DAPI staining, and green fluorescence was used for coumarin 6.

5.2.7. Annexin V staining

The effects of antioxidant nanoparticles on islets after hypoxic incubation were examined by isolating islets and placing them in a 24-well ultralow attachment plate with various concentrations of free or nanoencapsulated antioxidants in 500 μL of

media. After 6 hours of incubation, the islets were washed with RPMI media and fresh media (without antioxidants) was added. Islets were then transferred to an incubator with 1% O_2 and 5% CO_2 for 12 hours. Subsequently, the islets were removed and placed into a normoxic incubator with 21% O_2 and 5% CO_2 for 48 hours. Staining was performed using a BD Pharmingen Annexin V-FITC Fluorescence Microscopy Kit. Approximately 20 islets were placed in a 1.5 mL microcentrifuge tube and stained per the kit instructions. Islets were washed twice with PBS and once with annexin V buffer by centrifuging at 200 g for 3 minutes. Then 200 µL of a 1:10 dilution of FITC annexin V in annexin V buffer was added to the sample and the cells were incubated for 30 minutes at room temperature. They were subsequently washed twice with annexin buffer by centrifuging at 200 g and placed in a 24-well plate. The islets were then imaged using green fluorescence, and images were analyzed for fluorescence intensity using ImageJ.

5.2.8. Statistical analysis

For the statistical analysis, data was analyzed using GraphPad Prism. Student's two-tailed t-test assuming equal variance was used. Data is presented as mean ± standard deviation. A *p value* less than 0.05 is considered statistically significant.

5.3 Results and discussion

5.3.1. Bilirubin nanoparticle synthesis and characterization

The schematic diagram in **Figure 5.1A** shows the nanoparticle synthesis process using an oil-in-water single emulsion technique, followed by chitosan coating[253]. Nanoparticles are coated with chitosan to help increase their uptake into

cells[154,252,254]. Morphology of chitosan coated nanoparticles is confirmed through TEM imaging (**Figure 5.1B**).

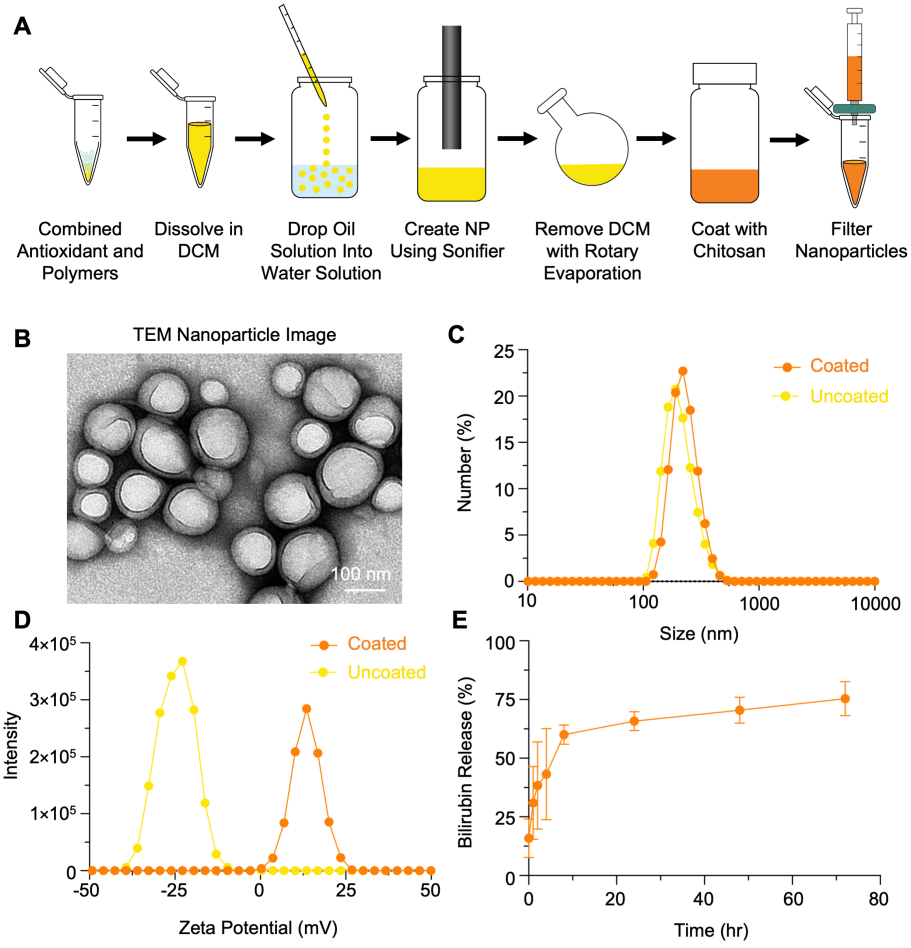

Figure 5.1. Overview of nanoparticle synthesis process and bilirubin nanoparticle characterization. (**A**) Schematic illustrating the nanoparticle synthesis process. The antioxidant is first mixed with polymers, followed by dissolution in DCM. This solution is then added dropwise to a water based PVA solution, and nanoparticles are generated using a sonifier. The sample undergoes rotary evaporation to remove the DCM. Then, the nanoparticles are coated overnight with chitosan, filtered, and characterized. (**B**) TEM image of a bilirubin chitosan coated PFP nanoparticles. (**C**) Representative size distribution of bilirubin PFP nanoparticles with and without chitosan coating. (**D**) Representative zeta potential measurement of bilirubin PFP nanoparticles with and without chitosan coating. (**E**) Release data of chitosan-coated bilirubin nanoparticles. n = 3 independent runs.

Figure 5.1C and **Figure 5.1D** show representative examples of the size and zeta potential measurements of PFP bilirubin nanoparticles with and without chitosan coating. After coating and filtering to remove excess chitosan, the nanoparticle size increases from 173.3 ± 21.9 nm to 187.1± 16.2 nm and the PDI decreases from 0.315 ± 0.052 to 0.113 ± 0.015 (**Table 5.1**). Notably, the chitosan coating does not significantly increase the size of the nanoparticles ($p = 0.4290$). The chitosan coating increases the nanoparticle charge from -26.61 ± 3.61 mV to 8.49 ± 1.09 mV, making it a slightly positive change which and favorable for nanoparticle penetration into cells[154,252,254,255]. The loading content of the coated nanoparticles is 1.44 ± 0.35%, and the encapsulation efficiency is 20.49 ± 0.10%.

Table 5.1. Bilirubin Nanoparticle Characterization

Chitosan Coating	Size (nm)	Zeta Potential (mV)	Polydispersity Index
Uncoated	173.3 ± 21.9	-26.61 ± 3.61	0.315 ± 0.052
Coated	187.1 ± 16.2	8.49 ± 1.09	0.113 ± 0.015

Studies have demonstrated that bilirubin's binding properties with albumin can impact its release from nanoparticles[154,256]. To mimic the conditions for in vitro nanoparticle uptake, release experiments were conducted using a medium of 10% FBS in PBS. **Figure 5.1E** shows the release of bilirubin for the chitosan coated nanoparticles over 72 hours. After 72 hours, ~ 75% of the bilirubin is released into the medium.

5.3.2. Curcumin nanoparticle synthesis and characterization

Curcumin is encapsulated using the same formulation and synthesis method as bilirubin. As shown in **Table 5.2**, the curcumin PFP-chitosan nanoparticles have an

average size, zeta potential, and PDI of 210.3 ± 15.5 nm, -36.36 ± 4.76 mV, and 0.056 ± 0.016, respectively, before coating. After coating, they have an average size of 224.3 ± 33.6 nm, an average zeta potential of 3.24 ± 0.41 mV, and an average PDI of 0.105 ± 0.136. They have an encapsulation efficiency of 22.38 ± 12.43% and a loading content of 1.14 ± 0.52%.

Table 5.2 Curcumin Nanoparticle Characterization

Chitosan Coating	Size (nm)	Zeta Potential (mV)	Polydispersity Index
Uncoated	210.3 ± 15.5	-36.36 ± 4.76	0.056 ± 0.016
Coated	224.3 ± 33.6	3.24 ± 0.41	0.105 ± 0.136

5.3.3. Nanoencapsulation of bilirubin improves uptake into MCF-7 and Beta-TC-6 cells

Bilirubin PFP-chitosan uptake of nanoparticles into cells is evaluated and compared with free bilirubin to determine if nanoencapsulation helps improve antioxidant uptake into cells. Fluorescence imaging can be used to confirm bilirubin uptake into cells due to its autofluorescence[256,257]. MCF-7 cells are incubated with media containing 20 μM free bilirubin or 20 μM nanoencapsulated bilirubin for 3 hours. The cells are stained for nuclei with DAPI and for endo-lysosomes with lysotracker to determine if bilirubin colocalizes with endo-lysosomes, showing nanoparticle uptake and intracellular delivery[258]. As shown in **Figure 5.2A**, the fluorescence signal of bilirubin is much stronger in the nanoencapsulated bilirubin group than in the free bilirubin group and the control group.

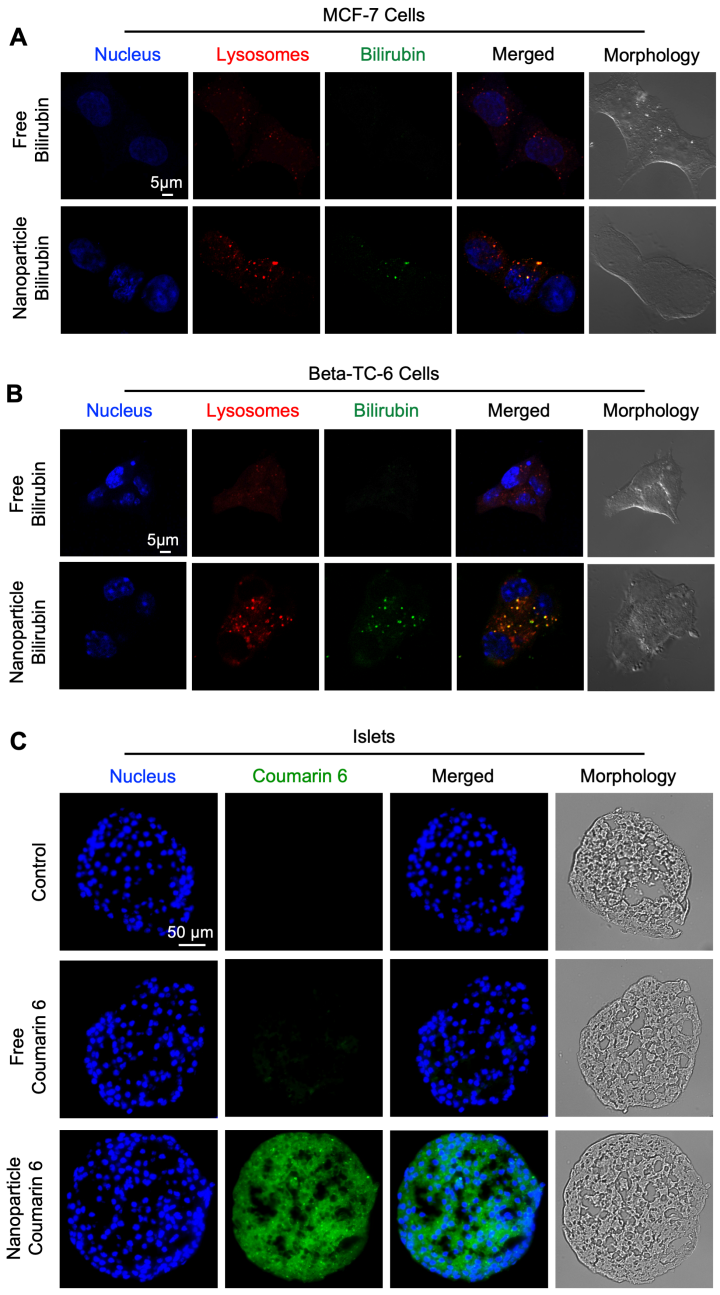

Figure 5.2. Bilirubin nanoparticle uptake into MCF-7, Beta-TC-6 cells, and Islets. (**A**) Representative images illustrating the uptake of 20 μM free bilirubin and 20 μM bilirubin PFP-chitosan nanoparticles into MCF-7 cells, stained for the nucleus and lysosomes. (**B**) Representative images illustrating the uptake of 20 μM free bilirubin and 20 μM bilirubin PFP-chitosan nanoparticles into Beta-TC-6 cells stained for the nucleus and lysosomes. (**C**) Representative images of cryosectioned slices of islets after incubation with media containing no coumarin 6, 8μM free coumarin 6, or 8μM coumarin 6 PFP-chitosan nanoparticles.

The bilirubin is colocalized with lysosomes, as indicated by the overlapping red and green signals resulting in yellow in **Figure 5.2A**[154]. Next, bilirubin uptake into Beta-TC-6 cells is evaluated. Beta-TC-6 cells are an insulinoma cell line derived from a pancreatic tumor in a mouse and have characteristics mimicking islet cells including insulin secretion and aggregation[259,260]. The same uptake procedure used for the MCF-7 cells is conducted using Beta-TC-6 cells. The results are shown in **Figure 5.2B**. Images also show higher fluorescence for nanoencapsulated bilirubin and colocalization with lysosomes. Consistency in results across cell lines confirms that PFP-chitosan nanoparticles facilitate bilirubin uptake into cells.

5.3.4. Nanoencapsulation of coumarin 6 improves its penetration into islets

Experiments are conducted using islets to assess the penetration of nanoparticles and free bilirubin within islets. Due to the comparatively weak fluorescence of bilirubin, coumarin 6 is used for imaging purposes instead, as it is similarly hydrophobic compared with bilirubin and curcumin but has stronger fluorescence[261,262]. Coumarin 6 has a molecular weight of 350.43 g/mol, which is close to the molecular weight of curcumin (368.38 g/mol) and in the same range of bilirubin's molecular weight (584.66 g/mol).

The same process used for fabricating bilirubin PFP-chitosan and curcumin PFP-chitosan nanoparticles is used for coumarin 6 PFP-chitosan nanoparticles. Coumarin 6 PFP-chitosan nanoparticles have an average size of ~ 190 nm and a zeta potential of ~ 5.3 mV, similar to the curcumin and bilirubin PFP-chitosan nanoparticles. Islets are incubated with media containing 8 μM nanoencapsulated coumarin 6, and free coumarin 6, or no coumarin 6 for 6 hours. Subsequently, the islets are

cryosectioned, placed on slides, and stained with DAPI. Imaging is performed using green and blue fluorescence for DAPI and coumarin 6, respectively. The results show that nanoencapsulated coumarin 6 exhibits much stronger fluorescence than free coumarin 6 and the control group and can penetrate throughout the islets (**Figure 5.2C**). Cryosectioning enables the assessment of slices from the center of the islets, confirming the dispersion of coumarin 6 throughout the islets. This delivery mechanism shows promising potential in preventing post-isolation cell death and the formation of necrotic islet cores[207,224].

5.3.5. Treating islets with nanoencapsulated antioxidants reduces apoptosis caused by hypoxic stress conditions in vitro

Antioxidant impact on islet apoptosis is evaluated in vitro using a hypoxic incubation model. Antioxidant concentrations ranging from 5 μM to 40 μM are selected, as these concentrations are considered physiologically relevant for both bilirubin and curcumin[154,228,237]. Islets are incubated with media containing free antioxidants, nanoencapsulated antioxidants, or no antioxidants (hypoxic control) for 6 hours and then placed in an incubator containing 1% O_2. The normoxic control group is continuously incubated at 21% O_2.

Annexin V staining is used to detect apoptosis in cells by binding with phosphatidylserine (**PS**). During apoptosis, phosphatidylserine (PS) translocases from the cytoplasmic side of the plasma membrane to the cell surface[211]. Treatment with both bilirubin and curcumin cause an overall decrease in annexin V staining compared with the hypoxic control (islets that underwent incubation in 1% O_2 with no antioxidant

treatment). As shown in **Figure 5.3A**, both bilirubin and curcumin reduce apoptosis compared with the negative control.

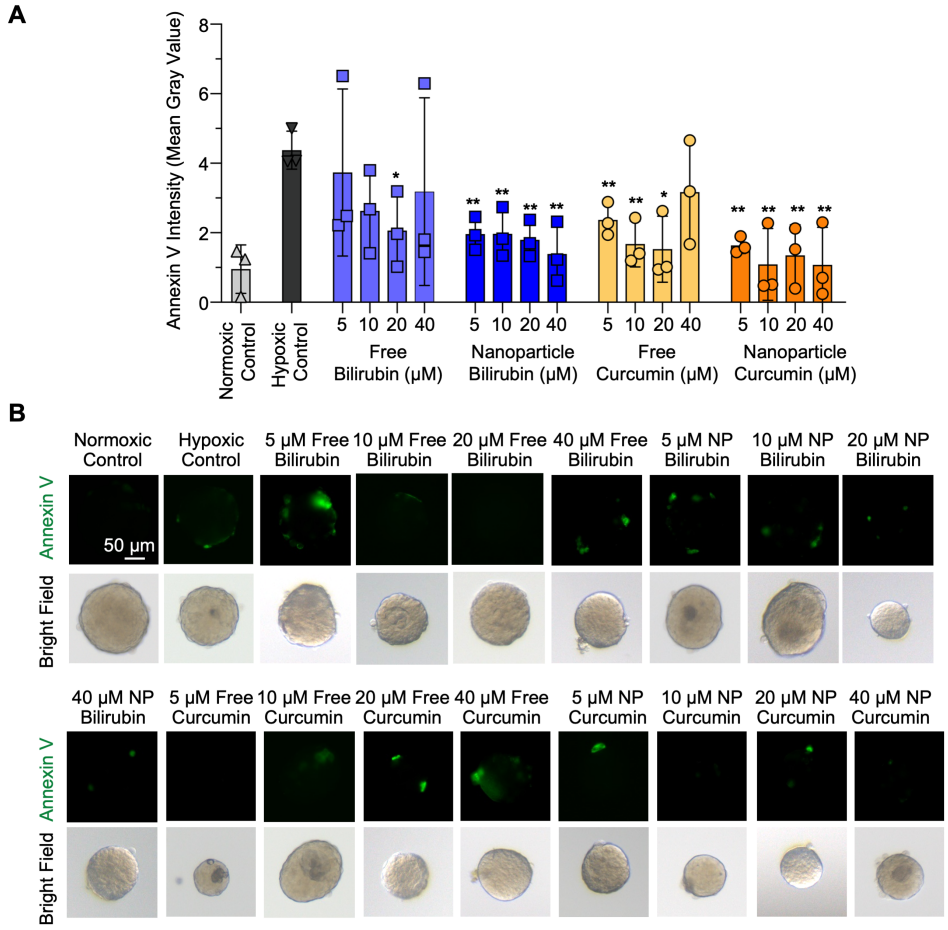

Figure 5.3. Annexin V staining after hypoxic incubation of antioxidant treated islets. (**A**) Fluorescence quantification (mean gray value) for annexin V staining of antioxidant treated islets and control islets after hypoxic incubation. n = 3 independent runs with approximately 7 IEQ per trial evaluated. *$p < 0.05$ and **$p < 0.01$ compared with hypoxic control. (**B**) Representative images of antioxidant treated islets and control islets stained with annexin V after hypoxic incubation.

The 20 μM concentration of free bilirubin exhibits a significant reduction in fluorescence, and all concentrations of nanoencapsulated bilirubin show a significant decrease in fluorescence. This could be attributed to the increased uptake of bilirubin

and its prolonged release over 60 hours, in contrast to free bilirubin. Curcumin also significantly reduces apoptosis in islets. All concentrations of free curcumin, except for 40 μM, as well as all concentrations of nanoencapsulated curcumin, exhibit significantly reduced staining. These results suggest that both free and nanoencapsulated curcumin prevent apoptosis in islets, and the nanoparticles may not significantly enhance this effect at the tested concentrations. Considering the increased uptake and sustained release facilitated by the nanoparticles, it is possible that curcumin's effectiveness in preventing apoptosis could be achieved at lower concentrations. Representative images of islets stained with annexin V and bright field images of the islets used for image analysis are presented in **Figure 5.3B**. Islets incubated with nanoencapsulated bilirubin and curcumin, as well as lower concentrations of free curcumin show little to no annexin V staining, reflecting the fluorescence quantification in **Figure 5.3A**.

These results are consistent with findings from other studies. Studies have shown that bilirubin improves cell viability and reduces the effects of ROS compared to the hypoxic control, with only minor differences between nanoencapsulated and free bilirubin in vitro [154,228]. This may be due to bilirubin binding with albumin in culture medium, which could improve its uptake[28]. Similarly, nanoencapsulated curcumin has demonstrated increased uptake in insulinoma cell lines and an overall reduction in apoptotic markers compared to the hypoxic control, with only minor differences between encapsulated and free curcumin in vitro[237,238]. However, significant differences between free and nanoencapsulated antioxidants are observed in these studies during in vivo experiments. This emphasizes the need for further evaluation of

these PFP-chitosan antioxidant nanoparticles and their potential for future in vivo testing.

5.4 Conclusion

In this study, bilirubin and curcumin PFP-chitosan nanoparticles are successfully fabricated and characterized. Bilirubin PFP-chitosan nanoparticles are successfully taken up into MCF-7 and Beta-TC-6 cells, outperforming free bilirubin. Similarly, coumarin 6 PFP-chitosan nanoparticles created using the same synthesis method as the antioxidant nanoparticles have improved dispersion within islets when compared to free coumarin 6. Notably, our research shows that nanoparticle encapsulation results in penetration and dispersion of hydrophobic molecules throughout islets, a novel observation in this study. Uptake experiments show that both bilirubin and curcumin nanoparticles demonstrate protective effects on islets during incubation under hypoxic stress, reducing apoptosis. Future research should further characterize the effects of these antioxidants and antioxidant nanoparticles on islets, both through in vitro hypoxia experiments and through in vivo experiments.

Chapter 6 : Conclusions

In this dissertation, we address multiple issues that hinder the success of isolated microencapsulated islet transplantation for type 1 diabetes treatment. To tackle the problem of empty microcapsules occupying space during islet transplantation, we successfully develop an on-chip deep learning-based sorting system that efficiently separates aggregate-laden microcapsules from empty microcapsules without the need for cell labeling and then apply it to sorting islet-laden core-shell hydrogel microcapsules resulting in a highly pure microcapsule sample. To improve the design of microcapsules, we design a non-planar microfluidic device that can fabricate core-shell hydrogel microcapsules. In a syngeneic diabetic mouse model, islets encapsulated in core-shell hydrogel microcapsules control mouse blood glucose levels significantly better than conventional homogeneous alginate microcapsules. To protect islets from the effects of post-transplantation hypoxia, we fabricate PFP-chitosan nanoparticles that effectively encapsulate hydrophobic antioxidants, leading to increased antioxidant uptake into insulinoma cells and penetration into islets. We also find that enriching islets with free or nanoparticle forms of curcumin and bilirubin reduces apoptosis in islets exposed to hypoxic stress. These findings hold promise for future studies and potential clinical applications of these technologies for type 1 diabetes treatment.

Chapter 7 : Future Research Directions

7.1 Deep learning-based on-chip detection and selective extraction

In this dissertation, a deep learning-based detection and sorting system is developed that successfully sorts both aggregate and islet-laden microcapsules from empty microcapsules. Applying the aggregate model for islet sorting on a non-planar microfluidic chip (Chapter 4) resulted in a lower detection efficiency (80%) and purity (70%) of islet-laden microcapsules compared with the detection efficiency (100%) and purity (90%) for the aggregate-laden microcapsules fabricated on a planar microfluidic device (Chapter 3).

In this dissertation, a deep learning-based detection and sorting system is developed that successfully sorts both aggregate and islet-laden microcapsules from empty microcapsules. Applying the aggregate model for islet sorting on a non-planar microfluidic chip (Chapter 4) resulted in a lower detection efficiency (80%) and purity (70%) of islet-laden microcapsules compared with the detection efficiency (100%) and purity (90%) for the aggregate-laden microcapsules fabricated on a planar microfluidic device (Chapter 3).

To improve the detection and extraction efficiency and purity, the detection model can be retrained using images of encapsulated islets in a non-planar microfluidic device. The model's training dataset could also be expanded to encompass a broader range of sample images, particularly those with increased debris that occurs when scaling up the encapsulation to include hundreds of islets. The model could also be trained with images of islets that are partially in the detection region to improve detection efficiency. The detection of islets in microcapsules also faces limitations as

images are captured at a fixed distance from the microfluidic device. As a result, out-of-focus islets may be missed. In future experiments, it would be beneficial to explore systems capable of capturing images at different depths within the microchannel.

In addition, a line scanning camera may be used to improve detection efficiency and increase the system's speed. Line scanning has been used in industrial settings for fast object detection and sorting of objects on conveyor belts, and in combination with CNNs for high-speed imaging[263-265]. This could increase the detection efficiency and system speed, allowing more islets to be encapsulated in a shorter period. As deep learning systems continue to progress, the use of more advanced pre-trained models will enable the processing of higher-quality images at a faster rate[266]. T Combining high speed processing and high-resolution images should improve detection and extraction outcomes.

Extraction mechanisms other than DEP can also be investigated. Standing acoustic waves (**SAW**) have been shown to sort microparticles and droplets accurately and quickly on a microfluidic device[99,267,268]. This application of SAW could not only improve sample purity but also faster sorting allows for quicker islet encapsulation, which can help scale up the system for more extensive studies.

This non-planar microfluidic encapsulation system could have applications for encapsulating and sorting other tissues, such as ovarian follicles[95]. Furthermore, it can potentially be used for sorting islets of varying sizes and qualities, for example, identifying and sorting healthy islets out from damaged islets or islets with necrotic cores. Ultimately, this system shows promise for a wide range of biomedical and research applications, including and beyond islet transplantation.

7.2 Encapsulation and transplantation of islet-laden core-shell hydrogel microcapsule

In Chapter 4, islets are successfully encapsulated in core-shell hydrogel microcapsules using a non-planar microfluidic device. Encapsulation in core-shell microcapsules results in significantly improved blood glucose regulation in a syngeneic transplantation diabetic mouse model compared to conventionally used homogeneous alginate microcapsules. The transplanted microcapsules also do not increase the percentage of immune cells in the IP cavity, indicating that they are non-immunogenic. Allogenic and xenogeneic diabetic mouse models should be tested to evaluate how well the microcapsules protect islets in models with a higher immune response. Islets isolated from BALB/c mice (allogenic) and Sprague Dawley rats (xenogeneic) can be transplanted into diabetic C57BL/6 mice[88,191,269]. These models can provide valuable insights into islet transplantation outcomes by characterizing the immune response and its impact on graft rejection.

Luciferase islet transplantation can be used to assess the viability and location of islets over time. Preliminary observations in this research show that transplanted luciferase islets stop exhibiting bioluminescence a few weeks after transplantation in C57BL/6 mice, likely due to immune response and subsequent islet rejection. These results align with findings from other studies[93,270]. For further investigation, core-shell hydrogel encapsulated and alginate hydrogel encapsulated luciferase islets can be transplanted into C57BL/6 mice and monitored over several months to assess islet health and rejection over time.

Further in vitro testing can explore the potential benefits of added alternative extracellular matrix materials, such as different types of collagens and laminin, to the core of core-shell hydrogen microcapsules, assessing their impact on insulin production and cell viability over time[78,214,271]. Incorporating decellularized extracellular matrix derived from islets or pancreatic tissue into the microcapsules's core could also be an area of exploration, as well as creating biomimetic microcapsules by adding stromal cells into the microcapsule interior.

Mesenchymal stem cells (MSCs) offer an additional way to help mitigate immune response. Previous studies have demonstrated their ability to diminish immune responses when co-transplanted with islets[272,273]. In future investigations, MSCs can be incorporated into the core and/or shell of the microcapsules to assess immune response modulation.

Alternate transplantation locations can be investigated, including the epididymal fat pad or the omentum. Other transplantation areas may require a reduced number of islets to treat diabetes, as they are more highly vascularized than the IP cavity[93,269,274]. Furthermore, the transplanted islets could be removed after transplantation to assess fibrotic growth and immune cell buildup on the islets and to perform GSIS, viability staining, and immunostaining.

In the future, alternative methods for tracking islets over time, such as using superparamagnetic iron oxide nanoparticles (SPIONs), could be considered[275]. Preliminary studies showed that chitosan-coated SPIONs could be effectively taken up by islets, as found in other studies[276,277]. This approach offers a promising way of

tracking the location of islets over time, potentially finding applications in clinical settings in the future.

Future studies may also explore the potential of cryopreserving core-shell microencapsulated islets. Since islets are isolated from deceased donors, the time lapse between isolation and transplantation decreases cell viability. Using cryopreservation for islet storage could allow for increased time between isolation and transplantation, opening more transplantation opportunities. Islets have been successfully cryopreserved in alginate microcapsules[278]. Notably, alginate microcapsules crosslinked with $CaCl_2$ have also been shown to decrease the amount of cryoprotectant required for vitrification (i.e., cooling to cryogenic temperature without ice formation), improving the cell cryopreservation process[279,280]. Using low cryoprotectant vitrification in combination with core-shell microencapsulation of islets could significantly enhance the islet cryopreservation process, leading to improved transplantation outcomes.

7.3 Protective effects of antioxidant nanoparticle islets

In Chapter 5, we find that PFP-chitosan nanoparticles improve the uptake of hydrophobic molecules into insulinoma cells and islets. Preliminary hypoxia studies show pretreating islets with bilirubin and curcumin leads to decreased apoptosis after hypoxic incubation. Future studies can further characterize the effects of free and nanoparticle antioxidants on islet health, including examining viability, necrosis, and insulin secretion. Studies can then be conducted in vivo in a diabetic mouse model, examining the effects of pretreating islets with antioxidant nanoparticles before transplantation and intravenous injection of antioxidant nanoparticles, which have

shown positive effects on diabetes treatment[228,238]. Furthermore, this approach could be combined with islet microencapsulation, potentially incorporating nanoparticles inside the microcapsules before transplantation.

Studies show that bilirubin and curcumin have anti-inflammatory properties and reduce immune response[228,234]. The PFP-chitosan antioxidant nanoparticles could be tested using in vitro co-culture with immune cells and in vivo to observe the immune response in an allogenic or xenogeneic mouse model.

Appendix: Supplementary Video Captions

Supplemental Video 3.1. Deep learning-enabled label-free detection and selective extraction of a cell aggregate-laden microcapsule at full speed. A green box in the detection region indicates no cell aggregate-laden microcapsule is detected and a red box indicates a cell aggregate-laden microcapsule detected. The format of the timer on the bottom left corner of the video is in minutes: seconds. milliseconds.

Supplemental Video 3.2. Deep learning-enabled label-free detection and extraction of a cell aggregate-laden microcapsule with reduced video speed to view extraction more clearly. The video runs at full speed when no cell aggregate-laden microcapsule is detected and slows down to 10% of full speed when a cell aggregate-laden microcapsule is detected. The green box in the detection region indicates no cell aggregate-laden microcapsule is detected and the red box indicates a cell aggregate-laden microcapsule is detected. The format of the timer on the bottom left corner of the video is in minutes: seconds. milliseconds.

Supplemental Video 4.1. Video of islet-laden microcapsule extracted from the oil channel to the aqueous channel by manually turning on and off dielectrophoresis. The video is taken using phase contrast to visualize microcapsules. The format of the timer on the top right corner of the video is in minutes: seconds. milliseconds.

Supplemental Video 4.2. Video of islet-laden microcapsule extracted from the oil channel to the aqueous channel by manually turning on and off dielectrophoresis. The

video is taken using bright field. The format of the timer on the top right corner of the video is in minutes: seconds. milliseconds.

Supplemental Video 4.3. Video of deep learning-enabled label-free detection and extraction of islet-laden microcapsules using deep-learning detection model and dielectrophoresis. A green box in the detection region indicates no islet-laden microcapsule present, and the red box indicates an islet-laden microcapsule present. The format of the timer on the top right

corner of the video is in minutes: seconds. milliseconds.

Supplemental Video 4.4. Video of deep learning-enabled label-free detection and extraction of islet-laden microcapsules using deep-learning detection model and dielectrophoresis slowed down to 10% speed for better visualization. A green box in the detection region indicates no islet-laden microcapsule present, and the red box indicates an islet-laden microcapsule present. The format of the timer on the top right corner of the video is in minutes: seconds. milliseconds.

Supplemental Video 4.5. Video of intraperitoneal islet transplantation into an anesthetized mouse using the needle transplantation method.

Publications and Conference Presentations

Peer-reviewed Journal Publications:

(1) **White, A. M.,** Zhang, Y., Shamul, J.G., Xu, J., Kwizera, E.A., Jiang, B., and He, X. Deep learning-enabled label-free on-chip detection and selective extraction of cell aggregate-laden hydrogel microcapsules. *Small* 2021; 2100491

(2) **White, A. M.**, James G. Shamul, Jiangsheng Xu, Samantha Stewart, Jonathan S. Bromberg, and Xiaoming He. Engineering Strategies to Improve Islet Transplantation for Type 1 Diabetes Therapy. *ACS Biomaterials Science & Engineering* 2020; 6: 2543-2562

(3) Ou, W., Stewart, S., **White, A.M.**, Kwizera, E., Xu, J., Fang, Y., Shamul, J., Xie, C., Nurudeen, S., Tirada, N., Lu, X., Tkaczuk, K., and He, X. In-situ cryo-immune engineering of tumor microenvironment with cold-responsive nanotechnology for cancer immunotherapy. *Nature Communications* 2023; 14: 392

(4) Jiang, B., **White, A.M.**, Ou, W., Van Belleghem, S., Stewart, S., Shamul, J.G., Rahaman, S.O., Fisher, J.P., and He, X. Noncovalent reversible binding-enabled facile fabrication of leak-free PDMS microfluidic devices without plasma treatment for convenient cell loading and retrieval. *Bioactive Materials* 2022; 16: 346-358

(5) Xu, J., Liu, Y., Liu, S., Ou, W., **White, A.M.**, Stewart, S., Tkaczuk, K.H.R., Ellis, L.M., Wan, J., Lu, X., and He, X. Metformin bicarbonate-mediated efficient RNAi for precise targeting of TP53 deficiency in colon and rectal cancers. *Nano Today* 2022; 43: 101406

(6) Kwizera, E.A., Sun, M., **White, A.M.**, Li, J., and He, X. Methods of generating dielectrophoretic force for microfluidic manipulation of bioparticles. ACS Biomaterials Science & Engineering 2021; 7: 2403-2063

(7) Wang, H., Liang, Y., Yin, Y.,Zhang, J., Su, W., **White, A.M.**, Jiang, B., Xu, J., Zhang, Y., Stewart, S., Lu, X., and He, X. Carbon nano-onion-mediated dual targeting of P-selectin and P-glycoprotein to overcome cancer drug resistance. *Nature Communications* 2021; 12: 312

(8) Xu, J., Shamul, J.G., Staten, N.A., **White, A.M.**, Jiang, B., and He, X. Bioinspired 3D culture in nanoliter hyaluronic acid-rich core-shell hydrogel microcapsules isolates highly pluripotent human iPSCs. Small 2021; 2102219

Conference Presentations:

(1) **White, A.M.** and He, X. "Deep Learning-enabled Label-free On-chip Detection and Selective Extraction of Cell Aggregate-laden Hydrogel Microcapsules" (Poster Presentation, Society for Biomaterials Annual Meeting and Exposition, April 2023, San Diego, CA).

(2) **White, A.M.,** Zhang, Y., Shamul, J.G., and He, X. "Deep Learning-Enabled Label-Free On-chip Detection and Selective Extraction of Cell Aggregate-Laden Microcapsules" (Oral Presentation, Summer Biomechanics, Bioengineering, and Biotransport Conference, June 2021, Virtual).

(3) **White, A.M.,** Zhang, Y., Shamul, J.G., and He, X. "Deep Learning Enables Label-Free On-Chip Identification and Selective Extraction of Cells" (Oral Presentation, Biomedical Engineering Society Meeting, October 2019, Philadelphia, PA).

(4) **White, A.M.,** Zhang, Y., Shamul, J.G., and He, X. “Deep Learning Assisted Label-Free On-Chip Selective Extraction of Single-Cell-Laden Droplets from Oil Into Aqueous Solution with Dielectrophoresis” (Oral Presentation, Summer Biomechanics, Bioengineering, and Biotransport Conference, June 2019, Seven Springs, PA).

Bibliography

1 Health, C. U. d. o. & Human, S. National Diabetes Statistics Report, 2020 Estimates of Diabetes and Its Burden in the United States. 2-2 (2020).

2 2017 Diabetes Report Card. (2017).

3 Roep, B. O. The role of T-cells in the pathogenesis of Type 1 diabetes: From cause to cure. *Diabetologia* **46**, 305-321 (2003). https://doi.org/10.1007/s00125-003-1089-5

4 World Health, O. Global Report on Diabetes. Report No. 978 92 4 156525 7, 88-88 (2016).

5 Cdc. Estimates of Diabetes and Its Burden in the United States Fast Facts on Diabetes Number with diabetes Total By sex National Diabetes Statistics Report, 2014. (2014).

6 Cryer, P. E. Vol. 117 868-870 (American Society for Clinical Investigation, 2007).

7 Shapiro, A. M. J., Pokrywczynska, M. & Ricordi, C. Clinical pancreatic islet transplantation. *Nature Reviews Endocrinology* **13**, 268-277 (2016). https://doi.org/10.1038/nrendo.2016.178

8 National Diabetes Information Clearinghouse of the National Institute of, D., Digestive & Kidney diseases of the, U. S. A. 1-6 (2014).

9 Vardanyan, M., Parkin, E., Gruessner, C. & Rodriguez Rilo, H. L. Pancreas vs. islet transplantation: A call on the future. *Current Opinion in Organ Transplantation* **15**, 124-130 (2010). https://doi.org/10.1097/MOT.0b013e32833553f8

10 Wilson, J. T. & Chaikof, E. L. Challenges and emerging technologies in the immunoisolation of cells and tissues. *Advanced Drug Delivery Reviews* **60**, 124-145 (2008). https://doi.org/10.1016/j.addr.2007.08.034

11 White, A. M. *et al.* Engineering Strategies to Improve Islet Transplantation for Type 1 Diabetes Therapy. *ACS Biomaterials Science & Engineering* **6**, 2543-2562 (2020). https://doi.org/10.1021/acsbiomaterials.9b01406

12 Calafiore, R. Vol. 3 201-205 (Taylor & Francis, 2003).

13 Ma, M. *et al.* Core-Shell Hydrogel Microcapsules for Improved Islets Encapsulation. *Advanced Healthcare Materials* **2**, 667-672 (2013). https://doi.org/10.1002/adhm.201200341

14 Agarwal, P. *et al.* A Biomimetic Core-Shell Platform for Miniaturized 3D Cell and Tissue Engineering. *Particle and Particle Systems Characterization* **32**, 809-816 (2015). https://doi.org/10.1002/ppsc.201500025

15 Huang, H. *et al.* Stiffness-Independent Highly Efficient On-Chip Extraction of Cell-Laden Hydrogel Microcapsules from Oil Emulsion into Aqueous Solution by Dielectrophoresis. *Small* **11**, 5369-5374 (2015). https://doi.org/10.1002/smll.201501388

16 Sun, M., Durkin, P., Li, J., Toth, T. L. & He, X. Label-Free On-Chip Selective Extraction of Cell-Aggregate-Laden Microcapsules from Oil into Aqueous Solution with Optical Sensor and Dielectrophoresis. *ACS Sens* **3**, 410-417 (2018). https://doi.org/10.1021/acssensors.7b00834

17 White, A. M. *et al.* Deep Learning-Enabled Label-Free On-Chip Detection and Selective Extraction of Cell Aggregate-Laden Hydrogel Microcapsules. *Small*, 2100491 (2021). https://doi.org/10.1002/smll.202100491
18 Vaithilingam, V., Bal, S. & Tuch, B. E. Encapsulated islet transplantation: Where do we stand? *Review of Diabetic Studies* **14**, 51-78 (2017). https://doi.org/10.1900/RDS.2017.14.51
19 Vaithilingam, V. & Tuch, B. E. Islet transplantation and encapsulation: an update on recent developments. *The review of diabetic studies : RDS* **8**, 51-67 (2011). https://doi.org/10.1900/RDS.2011.8.51
20 Shi, Y. *et al.* Immune-Protective Formulations and Process Strategies for Improved Survival and Function of Transplanted Islets. *Front Immunol* **13**, 923241 (2022). https://doi.org/10.3389/fimmu.2022.923241
21 Adin, C. A. *et al.* Physiologic doses of bilirubin contribute to tolerance of islet transplants by suppressing the innate immune response. *Cell Transplantation* **26**, 11-21 (2017). https://doi.org/10.3727/096368916X692096
22 Wang, Z. *et al.* Formulation strategies to provide oxygen-release to contrast local hypoxia for transplanted islets. *Eur J Pharm Biopharm* **187**, 130-140 (2023). https://doi.org/10.1016/j.ejpb.2023.04.015
23 Shapiro, A. M. J. State of the art of clinical islet transplantation and novel protocols of immunosuppression. *Current Diabetes Reports* **11**, 345-354 (2011). https://doi.org/10.1007/s11892-011-0217-8
24 Weber, C. J., Safley, S., Hagler, M. & Kapp, J. Evaluation of graft-host response for various tissue sources and animal models. *Annals of the New York Academy of Sciences* **875**, 233-254 (1999). https://doi.org/10.1111/j.1749-6632.1999.tb08507.x
25 Souza, Y. E. D. M. D. *et al.* Islet transplantation in rodents: do encapsulated islets really work? *Arquivos de Gastroenterologia* **48**, 146-152 (2011). https://doi.org/10.1590/s0004-28032011000200011
26 Eberhard, D., Kragl, M. & Lammert, E. 'Giving and taking': Endothelial and β-cells in the islets of Langerhans. *Trends in Endocrinology and Metabolism* **21**, 457-463 (2010). https://doi.org/10.1016/j.tem.2010.03.003
27 Steiner, D. J., Kim, A., Miller, K. & Hara, M. Pancreatic islet plasticity: interspecies comparison of islet architecture and composition. *Islets* **2**, 135-145 (2010). https://doi.org/10.4161/isl.2.3.11815
28 Jo, J., Moo, Y. C. & Koh, D. S. Size distribution of mouse Langerhans islets. *Biophysical Journal* **93**, 2655-2666 (2007). https://doi.org/10.1529/biophysj.107.104125
29 Marichal, P. I. t. V. & M. Vol. 654 1-19 (Springer, Dordrecht, 2010).
30 Mittal, S., Johnson, P. & Friend, P. Pancreas transplantation: Solid organ and islet. *Cold Spring Harbor Perspectives in Medicine* **4**, a015610-a015610 (2014). https://doi.org/10.1101/cshperspect.a015610
31 Ludwig, B. *et al.* Transplantation of human islets without immunosuppression. *Proceedings of the National Academy of Sciences of the United States of America* **110**, 19054-19058 (2013). https://doi.org/10.1073/pnas.1317561110

32 De Vos, P., De Haan, B., Pater, J. & Van Schilfgaarde, R. Association between capsule diameter, adequacy of encapsulation, and survival of microencapsulated rat islet allografts. *Transplantation* **62**, 893-899 (1996). https://doi.org/10.1097/00007890-199610150-00004
33 Beck, J. *et al.* Islet Encapsulation: Strategies to Enhance Islet Cell Functions. *Tissue Engineering* **13**, 589-599 (2007). https://doi.org/10.1089/ten.2006.0183
34 Kaddis, J. S. *et al.* Human pancreatic islets and diabetes research. *JAMA* **301**, 1580-1587 (2009). https://doi.org/10.1001/jama.2009.482
35 Valdés-González, R. A. *et al.* Xenotransplantation of porcine neonatal islets of Langerhans and Sertoli cells: a 4-year study. *European Journal of Endocrinology* **153**, 419-427 (2005). https://doi.org/10.1530/eje.1.01982
36 Morozov, V. A. *et al.* No PERV transmission during a clinical trial of pig islet cell transplantation. *Virus Research* **227**, 34-40 (2017). https://doi.org/10.1016/j.virusres.2016.08.012
37 Duvivier-Kali, V. F., Omer, A., Lopez-Avalos, M. D., O'Neil, J. J. & Weir, G. C. Survival of Microencapsulated Adult Pig Islets in Mice In Spite of an Antibody Response. *American Journal of Transplantation* **4**, 1991-2000 (2004). https://doi.org/10.1111/j.1600-6143.2004.00628.x
38 Elliott, R. B. *et al.* Live encapsulated porcine islets from a type 1 diabetic patient 9.5 yr after xenotransplantation. *Xenotransplantation* **14**, 157-161 (2007). https://doi.org/10.1111/j.1399-3089.2007.00384.x
39 Kelly, W. D., Lillehei, R. C., Merkel, F. K., Idezuki, Y. & Goetz, F. G. Allotransplantation of the pancreas and duodenum along with the kidney in diabetic nephropathy. *Surgery* **61**, 827-837 (1967). https://doi.org/10.1097/00007890-196801000-00034
40 Lillehei, R. C., Simmons, R. L., Najarian, J. S. & Goetz, F. C. Pancreatico-duodenal and renal allotransplantation in juvenile onset, insulin dependent, diabetes mellitus with terminal nephropathy. *Langenbecks Archiv für Chirurgie* **326**, 88-105 (1970). https://doi.org/10.1007/BF01238573
41 Moassesfar, S. *et al.* A Comparative Analysis of the Safety, Efficacy, and Cost of Islet Versus Pancreas Transplantation in Nonuremic Patients with Type 1 Diabetes. *American Journal of Transplantation* **16**, 518-526 (2016). https://doi.org/10.1111/ajt.13536
42 Karl, R. C., Scharp, D. W., Ballinger, W. F. & Lacy, P. E. Transplantation of insulin-secreting tissues. *Gut* **18**, 1062-1072 (1977). https://doi.org/10.1136/gut.18.12.1062
43 Shapiro, A. M. M. J. *et al.* International trial of the Edmonton protocol for islet transplantation. *New England Journal of Medicine* **355**, 1318-1330 (2006). https://doi.org/10.1056/NEJMoa061267
44 Anazawa, T., Okajima, H., Masui, T. & Uemoto, S. Current state and future evolution of pancreatic islet transplantation. *Annals of Gastroenterological Surgery* **3**, 34-42 (2019). https://doi.org/10.1002/ags3.12214
45 Lehmann, R. *et al.* Glycemic control in simultaneous islet-kidney versus pancreas-kidney transplantation in type 1 diabetes: A prospective 13-year follow-up. *Diabetes Care* **38**, 752-759 (2015). https://doi.org/10.2337/dc14-1686

46 Shapiro, A. M. J. *et al.* Islet Transplantation in Seven Patients with Type 1 Diabetes Mellitus Using a Glucocorticoid-Free Immunosuppressive Regimen. *New England Journal of Medicine* **343**, 230-238 (2000). https://doi.org/10.1056/NEJM200007273430401
47 Iacovacci, V., Ricotti, L., Menciassi, A. & Dario, P. The bioartificial pancreas (BAP): Biological, chemical and engineering challenges. *Biochemical Pharmacology* **100**, 12-27 (2016). https://doi.org/10.1016/j.bcp.2015.08.107
48 Kumagai-Braesch, M. *et al.* The theracyte™ device protects against islet allograft rejection in immunized hosts. *Cell Transplantation* **22**, 1137-1146 (2013). https://doi.org/10.3727/096368912X657486
49 Barkai, U. *et al.* Enhanced Oxygen Supply Improves Islet Viability in a New Bioartificial Pancreas. *Cell Transplantation* **22**, 1463-1476 (2013). https://doi.org/10.3727/096368912X657341
50 White, A. M. *et al.* Engineering Strategies to Improve Islet Transplantation for Type 1 Diabetes Therapy. *ACS Biomaterials Science and Engineering* **6** (2020). https://doi.org/10.1021/acsbiomaterials.9b01406
51 Desai, T. A., West, T., Cohen, M., Boiarski, T. & Rampersaud, A. *Nanoporous microsystems for islet cell replacement*. Vol. 56 (2004).
52 Banaszak, L. J. 1-5 (2000).
53 Desai, T. & Shea, L. D. Advances in islet encapsulation technologies. *Nature Reviews Drug Discovery* **16**, 338-350 (2017). https://doi.org/10.1038/nrd.2016.232
54 O'Shea, G. M. & Sun, A. M. Encapsulation of rat islets of Langerhans prolongs xenograft survival in diabetic mice. *Diabetes* **35**, 943-946 (1986). https://doi.org/10.2337/diab.35.8.943
55 Klein, J., Stock, J. & Vorlop, K. D. Pore size and properties of spherical Ca-alginate biocatalysts. *European Journal of Applied Microbiology and Biotechnology* **18**, 86-91 (1983). https://doi.org/10.1007/BF00500829
56 Stewart, W. W. & Swaisgood, H. E. Characterization of calcium alginate pore diameter by size-exclusion chromatography using protein standards. *Enzyme and Microbial Technology* **15**, 922-927 (1993). https://doi.org/10.1016/0141-0229(93)90167-Z
57 Sachan, N., Pushkar, S., Jha, A. & Bhattcharya, A. Sodium alginate: the wonder polymer for controlled drug delivery. *Journal of pharmacy research* **2**, 1191-1199 (2009).
58 Lee, K. Y. & Mooney, D. J. Alginate: Properties and biomedical applications. *Progress in Polymer Science (Oxford)* **37**, 106-126 (2012). https://doi.org/10.1016/j.progpolymsci.2011.06.003
59 Mallett, A. G. & Korbutt, G. S. Alginate Modification Improves Long-Term Survival and Function of Transplanted Encapsulated Islets. *Tissue Engineering Part A* **15**, 1301-1309 (2008). https://doi.org/10.1089/ten.tea.2008.0118
60 Donati, I. *et al.* New hypothesis on the role of alternating sequences in calcium-alginate gels. *Biomacromolecules* **6**, 1031-1040 (2005). https://doi.org/10.1021/bm049306e

61 Haug, A. *et al.* Selectivity of Some Anionic Polymers for Divalent Metal Ions. *Acta Chemica Scandinavica* **24**, 843-854 (1970). https://doi.org/10.3891/acta.chem.scand.24-0843
62 Smidsrød, O. Molecular basis for some physical properties of alginates in the gel state. *Faraday Discussions of the Chemical Society* **57**, 263-274 (1974). https://doi.org/10.1039/DC9745700263
63 Vériter, S. *et al.* In vivo selection of biocompatible alginates for islet encapsulation and subcutaneous transplantation. *Tissue Engineering - Part A* **16**, 1503-1513 (2010). https://doi.org/10.1089/ten.tea.2009.0286
64 Vegas, A. J. *et al.* Long-term glycemic control using polymer-encapsulated human stem cell-derived beta cells in immune-competent mice. *Nature Medicine* **22**, 306-311 (2016). https://doi.org/10.1038/nm.4030
65 Thanos, C. G. *et al.* Intraperitoneal stability of alginate-polyornithine microcapsules in rats: an FTIR and SEM analysis. *Biomaterials* **27**, 3570-3579 (2006). https://doi.org/10.1016/j.biomaterials.2006.01.042
66 Peirone, M. A., Delaney, K., Kwiecin, J., Fletch, A. & Chang, P. L. Delivery of recombinant gene product to canines with nonautologous microencapsulated cells. *Hum Gene Ther* **9**, 195-206 (1998). https://doi.org/10.1089/hum.1998.9.2-195
67 Stockley, T. L., Robinson, K. E., Delaney, K., Ofosu, F. A. & Chang, P. L. Delivery of recombinant product from subcutaneous implants of encapsulated recombinant cells in canines. *J Lab Clin Med* **135**, 484-492 (2000). https://doi.org/10.1067/mlc.2000.106804
68 Wang, T. *et al.* An encapsulation system for the immunoisolation of pancreatic islets. *Nat Biotechnol* **15**, 358-362 (1997). https://doi.org/10.1038/nbt0497-358
69 Tuch, B. E. *et al.* Safety and viability of microencapsulated human islets transplanted into diabetic humans. *Diabetes Care* **32**, 1887-1889 (2009). https://doi.org/10.2337/dc09-0744
70 Calafiore, R. & Basta, G. Clinical application of microencapsulated islets: actual prospectives on progress and challenges. *Adv Drug Deliv Rev* **67-68**, 84-92 (2014). https://doi.org/10.1016/j.addr.2013.09.020
71 Weber, L. M., He, J., Bradley, B., Haskins, K. & Anseth, K. S. PEG-based hydrogels as an in vitro encapsulation platform for testing controlled β-cell microenvironments. *Acta Biomaterialia* **2**, 1-8 (2006). https://doi.org/10.1016/J.ACTBIO.2005.10.005
72 Weber, L. M., Lopez, C. G. & Anseth, K. S. Effects of PEG hydrogel crosslinking density on protein diffusion and encapsulated islet survival and function. *Journal of biomedical materials research. Part A* **90**, 720-729 (2009). https://doi.org/10.1002/jbm.a.32134
73 Weber, L. M., Cheung, C. Y. & Anseth, K. S. Multifunctional Pancreatic Islet Encapsulation Barriers Achieved Via Multilayer PEG Hydrogels. *Cell Transplantation* **16**, 1049-1057 (2008).
74 Su, J., Hu, B. H., Lowe, W. L., Kaufman, D. B. & Messersmith, P. B. Anti-inflammatory peptide-functionalized hydrogels for insulin-secreting cell

encapsulation. *Biomaterials* **31**, 308-314 (2010). https://doi.org/10.1016/j.biomaterials.2009.09.045

75 Teramura, Y., Kaneda, Y. & Iwata, H. Islet-encapsulation in ultra-thin layer-by-layer membranes of poly(vinyl alcohol) anchored to poly(ethylene glycol)-lipids in the cell membrane. *Biomaterials* **28**, 4818-4825 (2007). https://doi.org/10.1016/j.biomaterials.2007.07.050

76 Stendahl, J. C., Kaufman, D. B. & Stupp, S. I. Extracellular Matrix in Pancreatic Islets: Relevance to Scaffold Design and Transplantation. (2009).

77 Llacua, L. A., de Haan, B. J. & de Vos, P. Laminin and collagen IV inclusion in immunoisolating microcapsules reduces cytokine-mediated cell death in human pancreatic islets. *Journal of Tissue Engineering and Regenerative Medicine* **12**, 460-467 (2018). https://doi.org/10.1002/term.2472

78 Weber, L. M. & Anseth, K. S. Hydrogel encapsulation environments functionalized with extracellular matrix interactions increase islet insulin secretion. *Matrix Biology* **27**, 667-673 (2008). https://doi.org/10.1016/J.MATBIO.2008.08.001

79 Chaimov, D. *et al.* Innovative encapsulation platform based on pancreatic extracellular matrix achieve substantial insulin delivery. (2016). https://doi.org/10.1016/j.jconrel.2016.07.045

80 Fukuda, Y. *et al.* Layer-by-layer cell coating technique using extracellular matrix facilitates rapid fabrication and function of pancreatic β-cell spheroids. *Biomaterials* **160**, 82-91 (2018). https://doi.org/10.1016/j.biomaterials.2018.01.020

81 Dimitrioglou, N., Kanelli, M., Papageorgiou, E., Karatzas, T. & Hatziavramidis, D. Paving the way for successful islet encapsulation. *Drug Discovery Today* **24**, 737-748 (2019). https://doi.org/10.1016/J.DRUDIS.2019.01.020

82 Lim, F. & Sun, A. M. Microencapsulated islets as bioartificial endocrine pancreas. *Science* **210**, 908-910 (1980). https://doi.org/10.1126/science.6776628

83 Rabanel, J.-M., Banquy, X., Zouaoui, H., Mokhtar, M. & Hildgen, P. Progress Technology in Microencapsulation Methods for Cell Therapy. *American Institute of Chemical Engineers Biotechnol. Prog* **25**, 946-963 (2009). https://doi.org/10.1021/bp.226

84 Wolters, G. H. J., Fritschy, W. M., Gerrits, D. & Van Schilfgaarde, R. A versatile alginate droplet generator applicable for microencapsulation of pancreatic islets. *Journal of Applied Biomaterials* **3**, 281-286 (1992). https://doi.org/10.1002/jab.770030407

85 Opara, E. C., McQuilling, J. P. & Farney, A. C. Microencapsulation of pancreatic islets for use in a bioartificial pancreas. *Methods in molecular biology (Clifton, N.J.)* **1001**, 261-266 (2013). https://doi.org/10.1007/978-1-62703-363-3_21

86 Liaudanskaya, V., Gasperini, L., Maniglio, D., Motta, A. & Migliaresi, C. Assessing the Impact of Electrohydrodynamic Jetting on Encapsulated Cell Viability, Proliferation, and Ability to Self-Assemble in Three-Dimensional

Structures. *Tissue Engineering Part C: Methods* **21**, 631-638 (2015). https://doi.org/10.1089/ten.tec.2014.0228
87 Omer, A. *et al.* Long-term normoglycemia in rats receiving transplants with encapsulated islets. *Transplantation* **79**, 52-58 (2005). https://doi.org/10.1097/01.TP.0000149340.37865.46
88 Ma, M. *et al.* Core-shell hydrogel microcapsules for improved islets encapsulation. *Advanced healthcare materials* **2**, 667-672 (2013). https://doi.org/10.1002/adhm.201200341
89 Tomei, A. A. *et al.* Device design and materials optimization of conformal coating for islets of Langerhans. *Proceedings of the National Academy of Sciences of the United States of America* **111**, 10514-10519 (2014). https://doi.org/10.1073/pnas.1402216111
90 Manzoli, V. *et al.* Immunoisolation of murine islet allografts in vascularized sites through conformal coating with polyethylene glycol. *Am J Transplant* **18**, 590-603 (2018). https://doi.org/10.1111/ajt.14547
91 Weibel, D. B., DiLuzio, W. R. & Whitesides, G. M. Microfabrication meets microbiology. *Nature Reviews Microbiology* **5**, 209-218 (2007). https://doi.org/10.1038/nrmicro1616
92 Seemann, R., Brinkmann, M., Pfohl, T. & Herminghaus, S. Droplet based microfluidics. *Reports on Progress in Physics* **75**, 016601-016601 (2012). https://doi.org/10.1088/0034-4885/75/1/016601
93 Weaver, J. D. *et al.* Synthetic poly(ethylene glycol)-based microfluidic islet encapsulation reduces graft volume for delivery to highly vascularized and retrievable transplant site. *American Journal of Transplantation* **19**, 1315-1327 (2019). https://doi.org/10.1111/ajt.15168
94 Headen, D. M., Aubry, G., Lu, H. & García, A. J. Microfluidic-based generation of size-controlled, biofunctionalized synthetic polymer microgels for cell encapsulation. *Advanced Materials* **26**, 3003-3008 (2014). https://doi.org/10.1002/adma.201304880
95 Choi, J. K., Agarwal, P., Huang, H., Zhao, S. & He, X. The crucial role of mechanical heterogeneity in regulating follicle development and ovulation with engineered ovarian microtissue. *Biomaterials* **35**, 5122-5128 (2014). https://doi.org/10.1016/j.biomaterials.2014.03.028
96 Huang, H. *et al.* Generation and manipulation of hydrogel microcapsules by droplet-based microfluidics for mammalian cell culture. *Lab Chip* **17**, 1913-1932 (2017). https://doi.org/10.1039/C7LC00262A
97 Agarwal, P. *et al.* Microfluidics Enabled Bottom-Up Engineering of 3D Vascularized Tumor for Drug Discovery. *ACS Nano* **11**, 6691-6702 (2017). https://doi.org/10.1021/acsnano.7b00824
98 Tendulkar, S. *et al.* A scalable microfluidic device for the mass production of microencapsulated islets. *Transplantation Proceedings* **43**, 3184-3187 (2011). https://doi.org/10.1016/j.transproceed.2011.10.023
99 Nam, J., Lim, H., Kim, C., Yoon Kang, J. & Shin, S. Density-dependent separation of encapsulated cells in a microfluidic channel by using a standing surface acoustic wave. *Biomicrofluidics* **6**, 024120-024120 (2012). https://doi.org/10.1063/1.4718719

100 Sciambi, A. & Abate, A. R. Accurate microfluidic sorting of droplets at 30 kHz. *Lab on a Chip* **15**, 47-51 (2015). https://doi.org/10.1039/c4lc01194e
101 He, X. Microfluidic Encapsulation of Ovarian Follicles for 3D Culture. *Ann Biomed Eng* **45**, 1676-1684 (2017). https://doi.org/10.1007/s10439-017-1823-7
102 He, X. Microfluidic Encapsulation of Ovarian Follicles for 3D Culture. *Annals of Biomedical Engineering* **45**, 1676-1684 (2017). https://doi.org/10.1007/s10439-017-1823-7
103 O'Neill, P. R., Karunarathne, W. K. A., Kalyanaraman, V., Silvius, J. R. & Gautama, N. G-protein signaling leverages subunit-dependent membrane affinity to differentially control βγ translocation to intracellular membranes. *Proceedings of the National Academy of Sciences of the United States of America* **109**, 20784-20784 (2012). https://doi.org/10.1073/pnas.1205345109
104 Gossett, D. R. *et al.* Inertial manipulation and transfer of microparticles across laminar fluid streams. *Small* **8**, 2757-2764 (2012). https://doi.org/10.1002/smll.201200588
105 Pariset, E. *et al.* Particle Separation: Anticipating Cutoff Diameters in Deterministic Lateral Displacement (DLD) Microfluidic Devices for an Optimized Particle Separation (Small 37/2017). *Small* **13** (2017). https://doi.org/10.1002/smll.201770201
106 Tran, T. S. H., Ho, B. D., Beech, J. P. & Tegenfeldt, J. O. Open channel deterministic lateral displacement for particle and cell sorting. *Lab on a Chip* **17**, 3592-3600 (2017). https://doi.org/10.1039/c7lc00707h
107 Wong, E. H. M., Rondeau, E., Schuetz, P. & Cooper-White, J. A microfluidic-based method for the transfer of biopolymer particles from an oil phase to an aqueous phase. *Lab on a Chip* **9**, 2582-2590 (2009). https://doi.org/10.1039/b903774h
108 Agresti, J. J. *et al.* Ultrahigh-throughput screening in drop-based microfluidics for directed evolution. *Proceedings of the National Academy of Sciences of the United States of America* **107**, 4004-4009 (2010). https://doi.org/10.1073/pnas.0910781107
109 Cao, Z. *et al.* Droplet sorting based on the number of encapsulated particles using a solenoid valve. *Lab on a Chip* **13**, 171-178 (2013). https://doi.org/10.1039/c2lc40950j
110 Webb, S. Deep learning for biology. *Nature* **554**, 555-557 (2018). https://doi.org/10.1038/d41586-018-02174-z
111 Lin, X. *et al.* All-optical machine learning using diffractive deep neural networks. *Science* **361**, 1004-1008 (2018). https://doi.org/10.1126/science.aat8084
112 Christiansen, E. M. *et al.* In Silico Labeling: Predicting Fluorescent Labels in Unlabeled Images. *Cell* **173**, 792-803.e719 (2018). https://doi.org/10.1016/j.cell.2018.03.040
113 Wu, Y. & Shroff, H. Faster, sharper, and deeper: structured illumination microscopy for biological imaging. *Nature Methods* **15**, 1011-1019 (2018). https://doi.org/10.1038/s41592-018-0211-z

114 Zhang, P. *et al.* Analyzing complex single-molecule emission patterns with deep learning. *Nature Methods* **15**, 913-916 (2018). https://doi.org/10.1038/s41592-018-0153-5
115 Adamson, A. S. & Smith, A. Machine learning and health care disparities in dermatology. *JAMA Dermatology* **154**, 1247-1248 (2018). https://doi.org/10.1001/jamadermatol.2018.2348
116 Lin, T. Y. *et al.* PART 5 edn 740-755.
117 Schmidhuber, J. Deep Learning in neural networks: An overview. *Neural Networks* **61**, 85-117 (2015). https://doi.org/10.1016/j.neunet.2014.09.003
118 LeCun, Y., Bengio, Y. & Hinton, G. Deep learning. *Nature* **521**, 436-444 (2015). https://doi.org/10.1038/nature14539
119 Heo, Y. J., Lee, D., Kang, J., Lee, K. & Chung, W. K. Real-time Image Processing for Microscopy-based Label-free Imaging Flow Cytometry in a Microfluidic Chip. *Scientific Reports* **7**, 1-9 (2017). https://doi.org/10.1038/s41598-017-11534-0
120 Zhang, Z. *et al.* Evaluation of machine learning–driven automated Kleihauer-Betke counting: A method comparison study. *International Journal of Laboratory Hematology* (2020). https://doi.org/10.1111/ijlh.13380
121 Anagnostidis, V. *et al.* Deep learning guided image-based droplet sorting for on-demand selection and analysis of single cells and 3D cell cultures. *Lab on a Chip* **20**, 889-900 (2020). https://doi.org/10.1039/d0lc00055h
122 Girault, M. *et al.* An on-chip imaging droplet-sorting system: A real-time shape recognition method to screen target cells in droplets with single cell resolution. *Scientific Reports* **7** (2017). https://doi.org/10.1038/srep40072
123 Chu, A. *et al.* Automated detection and sorting of microencapsulation: Via machine learning. *Lab on a Chip* **19**, 1808-1817 (2019). https://doi.org/10.1039/c8lc01394b
124 Ludwig, B. *et al.* Favorable outcome of experimental islet xenotransplantation without immunosuppression in a nonhuman primate model of diabetes. *Proceedings of the National Academy of Sciences of the United States of America* **114**, 11745-11750 (2017). https://doi.org/10.1073/pnas.1708420114
125 Farina, M. *et al.* 3D Printed Vascularized Device for Subcutaneous Transplantation of Human Islets. *Biotechnology Journal* **12** (2017). https://doi.org/10.1002/biot.201700169
126 Bromberg, J. S. Islet implantation in a pocket. *Nature Biotechnology* **33**, 493-494 (2015). https://doi.org/10.1038/nbt.3216
127 Marchioli, G. *et al.* Fabrication of three-dimensional bioplotted hydrogel scaffolds for islets of Langerhans transplantation. *Biofabrication* **7**, 25009-25009 (2015). https://doi.org/10.1088/1758-5090/7/2/025009
128 Song, S. *et al.* An intravascular bioartificial pancreas device (iBAP) with silicon nanopore membranes (SNM) for islet encapsulation under convective mass transport. *Lab on a Chip* **17**, 1778-1792 (2017). https://doi.org/10.1039/c7lc00096k
129 Nauta, A. J. & Fibbe, W. E. Immunomodulatory properties of mesenchymal stromal cells. *Blood* **110**, 3499-3506 (2007). https://doi.org/10.1182/blood-2007-02-069716

130 Ito, T. *et al.* Mesenchymal stem cell and islet co-transplantation promotes graft revascularization and function. *Transplantation* **89**, 1438-1445 (2010). https://doi.org/10.1097/TP.0b013e3181db09c4
131 Ben Nasr, M. *et al.* Co-transplantation of autologous MSCs delays islet allograft rejection and generates a local immunoprivileged site. *Acta Diabetologica* **52**, 917-927 (2015). https://doi.org/10.1007/s00592-015-0735-y
132 Vaithilingam, V. *et al.* Co-encapsulation and co-transplantation of mesenchymal stem cells reduces pericapsular fibrosis and improves encapsulated islet survival and function when allografted. *Scientific Reports* **7**, 10059-10059 (2017). https://doi.org/10.1038/s41598-017-10359-1
133 Yonekawa, Y. *et al.* Effective islet isolation method with extremely high islet yields from adult pigs. *Cell Transplantation* **14**, 757-762 (2005). https://doi.org/10.3727/000000005783982512
134 Dufrane, D. *et al.* Parameters favouring successful adult pig islet isolations for xenotransplantation in pig-to-primate models. *Xenotransplantation* **13**, 204-214 (2006). https://doi.org/10.1111/j.1399-3089.2006.00275.x
135 Qi, M. *et al.* The Choice of Enzyme for Human Pancreas Digestion Is a Critical Factor for Increasing the Success of Islet Isolation. *Transplantation Direct* **1**, 1-9 (2015). https://doi.org/10.1097/txd.0000000000000522
136 Li, D. S., Yuan, Y. H., Tu, H. J., Liang, Q. L. & Dail, L. J. A protocol for islet isolation from mouse pancreas. *Nature Protocols* **4**, 1649-1652 (2009). https://doi.org/10.1038/nprot.2009.150
137 Kendall, W. F. & Opara, E. C. Vol. 1479 175-189 (Humana Press, New York, NY, 2017).
138 Chadwick, D. R. *et al.* Human islet purification: a prospective comparison of Euro-Ficoll and bovine serum albumin density gradients. *Acta Diabetologica* **30**, 57-59 (1993). https://doi.org/10.1007/BF00572876
139 Min, T. *et al.* Superiority of Visipaque (Iodixanol)-Controlled Density Gradient Over Ficoll-400 in Adult Porcine Islet Purification. *Transplantation Proceedings* **42**, 1825-1829 (2010). https://doi.org/10.1016/J.TRANSPROCEED.2010.01.068
140 Zongyi, Y. *et al.* A rapid, efficient, & economic device & method for the isolation & purification of mouse islet cells. *PLoS ONE* **12**, e0171618-e0171618 (2017). https://doi.org/10.1371/journal.pone.0171618
141 Zhu, H. *et al.* Selection of Implantation Sites for Transplantation of Encapsulated Pancreatic Islets. *Tissue Engineering - Part B: Reviews* **24**, 191-214 (2018). https://doi.org/10.1089/ten.teb.2017.0311
142 Lee, S. H. *et al.* Human β-cell precursors mature into functional insulin-producing cells in an immunoisolation device: Implications for diabetes cell therapies. *Transplantation* **87**, 983-991 (2009). https://doi.org/10.1097/TP.0b013e31819c86ea
143 Liu, X. Y., Nothias, J. M., Scavone, A., Garfinkel, M. & Millis, J. M. Biocompatibility investigation of polyethylene glycol and alginate-poly-l-lysine for islet encapsulation. *ASAIO Journal* **56**, 241-245 (2010). https://doi.org/10.1097/MAT.0b013e3181d7b8e3

144 Sakata, N. *et al.* Strategy for clinical setting in intramuscular and subcutaneous islet transplantation. (2013). https://doi.org/10.1002/dmrr.2463
145 Elliott, R. B. *et al.* Intraperitoneal alginate-encapsulated neonatal porcine islets in a placebo-controlled study with 16 diabetic cynomolgus primates. *Transplantation proceedings* **37**, 3505-3508 (2005). https://doi.org/10.1016/j.transproceed.2005.09.038
146 Basta, G. *et al.* Long-term metabolic and immunological follow-up of nonimmunosuppressed patients with type 1 diabetes treated with microencapsulated islet allografts: Four cases. *Diabetes Care* **34**, 2406-2409 (2011). https://doi.org/10.2337/dc11-0731
147 Kriz, J. *et al.* A novel technique for the transplantation of pancreatic islets within a vascularized device into the greater omentum to achieve insulin independence. *American Journal of Surgery* **203**, 793-797 (2012). https://doi.org/10.1016/j.amjsurg.2011.02.009
148 Zhang, W. *et al.* A novel core-shell microcapsule for encapsulation and 3D culture of embryonic stem cells. *Journal of Materials Chemistry B* **1**, 1002-1009 (2013). https://doi.org/10.1039/c2tb00058j
149 He, X. Vol. 3 2692-2701 (NIH Public Access, 2017).
150 Davalli, A. M. *et al.* Vulnerability of islets in the immediate posttransplantation period: Dynamic changes in structure and function. *Diabetes* **45**, 1161-1167 (1996). https://doi.org/10.2337/diab.45.9.1161
151 Wang, H. *et al.* Bilirubin can induce tolerance to islet allografts. *Endocrinology* **147**, 762-768 (2006). https://doi.org/10.1210/en.2005-0632
152 Adin, C. A. *et al.* Physiologic Doses of Bilirubin Contribute to Tolerance of Islet Transplants by Suppressing the Innate Immune Response. *Cell Transplant* **26**, 11-21 (2017). https://doi.org/10.3727/096368916X692096
153 Adin, C. A., Croker, B. P. & Agarwal, A. Protective effects of exogenous bilirubin on ischemia-reperfusion injury in the isolated, perfused rat kidney. *American Journal of Physiology - Renal Physiology* **288**, F778-F784 (2005). https://doi.org/10.1152/ajprenal.00215.2004
154 Fullagar, B. *et al.* Nano-Encapsulation of Bilirubin in Pluronic F127-Chitosan Improves Uptake in beta Cells and Increases Islet Viability and Function after Hypoxic Stress. *Cell Transplant* **26**, 1703-1715 (2017). https://doi.org/10.1177/0963689717735112
155 M. Ramkumar, K. *et al.* The Impact of Oxidative Stress on Islet Transplantation and Monitoring the Graft Survival by Non-Invasive Imaging. *Current Medicinal Chemistry* **20**, 1127-1146 (2013). https://doi.org/10.2174/0929867311320090003
156 Cavallari, G. *et al.* Mesenchymal stem cells and islet cotransplantation in diabetic rats: improved islet graft revascularization and function by human adipose tissue-derived stem cells preconditioned with natural molecules. *Cell transplantation* **21**, 2771-2781 (2012). https://doi.org/10.3727/096368912X637046
157 Vaithilingam, V. *et al.* Effect of prolonged gelling time on the intrinsic properties of barium alginate microcapsules and its biocompatibility. *Journal*

of Microencapsulation **28**, 499-507 (2011). https://doi.org/10.3109/02652048.2011.586067
158 Bochenek, M. A. *et al.* Alginate encapsulation as long-term immune protection of allogeneic pancreatic islet cells transplanted into the omental bursa of macaques. *Nature Biomedical Engineering* **2**, 810-821 (2018). https://doi.org/10.1038/s41551-018-0275-1
159 Yang, H. K. *et al.* Long-term Efficacy and Biocompatibility of Encapsulated Islet Transplantation with Chitosan-Coated Alginate Capsules in Mice and Canine Models of Diabetes. *Transplantation* **100**, 334-343 (2016). https://doi.org/10.1097/TP.0000000000000927
160 Vaithilingam, V. *et al.* Beneficial effects of coating alginate microcapsules with macromolecular heparin conjugates-In vitro and in vivo study. *Tissue Engineering - Part A* **20**, 324-334 (2014). https://doi.org/10.1089/ten.tea.2013.0254
161 Zhang, J. *et al.* One-step fabrication of supramolecular microcapsules from microfluidic droplets. *Science* **335**, 690-694 (2012). https://doi.org/10.1126/science.1215416
162 Mao, A. S. *et al.* Programmable microencapsulation for enhanced mesenchymal stem cell persistence and immunomodulation. *Proceedings of the National Academy of Sciences of the United States of America* **116**, 15392-15397 (2019). https://doi.org/10.1073/pnas.1819415116
163 Zhang, W. & He, X. Microencapsulating and Banking Living Cells for Cell-Based Medicine. *Journal of Healthcare Engineering* **2**, 427-446 (2011). https://doi.org/10.1260/2040-2295.2.4.427
164 Choi, J. K., Agarwal, P., Huang, H., Zhao, S. & He, X. The crucial role of mechanical heterogeneity in regulating follicle development and ovulation with engineered ovarian microtissue. *Biomaterials* **35**, 5122-5128 (2014). https://doi.org/10.1016/j.biomaterials.2014.03.028
165 Zhao, S. *et al.* Bioengineering of injectable encapsulated aggregates of pluripotent stem cells for therapy of myocardial infarction. *Nature Communications* **7**, 1-12 (2016). https://doi.org/10.1038/ncomms13306
166 Shang, L., Cheng, Y. & Zhao, Y. Emerging Droplet Microfluidics. *Chemical Reviews* **117**, 7964-8040 (2017). https://doi.org/10.1021/acs.chemrev.6b00848
167 Huang, H. & He, X. Fluid displacement during droplet formation at microfluidic flow-focusing junctions. *Lab on a Chip* **15**, 4197-4205 (2015). https://doi.org/10.1039/c5lc00730e
168 Collins, D. J., Neild, A., DeMello, A., Liu, A. Q. & Ai, Y. The Poisson distribution and beyond: Methods for microfluidic droplet production and single cell encapsulation. *Lab on a Chip* **15**, 3439-3459 (2015). https://doi.org/10.1039/c5lc00614g
169 De Groot, M. *et al.* Rat islet isolation yield and function are donor strain dependent. *Laboratory Animals* **38**, 200-206 (2004). https://doi.org/10.1258/002367704322968885
170 He, X. & Toth, T. L. In vitro culture of ovarian follicles from Peromyscus. *Seminars in Cell and Developmental Biology* **61**, 140-149 (2017). https://doi.org/10.1016/j.semcdb.2016.07.006

171 Sun, M., Durkin, P., Li, J., Toth, T. L. & He, X. Label-Free On-Chip Selective Extraction of Cell-Aggregate-Laden Microcapsules from Oil into Aqueous Solution with Optical Sensor and Dielectrophoresis. *ACS Sensors* **3**, 410-417 (2018). https://doi.org/10.1021/acssensors.7b00834
172 Wang, H. *et al.* Bioinspired One Cell Culture Isolates Highly Tumorigenic and Metastatic Cancer Stem Cells Capable of Multilineage Differentiation. *Advanced Science* **7**, 2000259-2000259 (2020). https://doi.org/10.1002/advs.202000259
173 Administration, U. S. F. a. D. GRAS Notification for Use of Mineral Oil as a Direct Additive in Food Products. (2000). <https://wayback.archive-it.org/7993/20171031054302/https://www.fda.gov/downloads/Food/IngredientsPackagingLabeling/GRAS/NoticeInventory/UCM266164.pdf>.
174 Schapiro, A. C., Rogers, T. T., Cordova, N. I., Turk-Browne, N. B. & Botvinick, M. M.
175 Huang, H. & He, X. Interfacial tension based on-chip extraction of microparticles confined in microfluidic Stokes flows. *Applied Physics Letters* **105** (2014). https://doi.org/10.1063/1.4898040
176 Linder, T., Dressler-Steinbach, I., Tura, A. & Gobl, C. New Developments, Challenges and Open Questions in Diagnosis and Treatment of Gestational Diabetes Mellitus. *J Clin Med* **11** (2022). https://doi.org/10.3390/jcm11237197
177 Kang, S. M., Lee, J. H., Huh, Y. S. & Takayama, S. Alginate Microencapsulation for Three-Dimensional In Vitro Cell Culture. *ACS Biomater Sci Eng* **7**, 2864-2879 (2021). https://doi.org/10.1021/acsbiomaterials.0c00457
178 Schrezenmeir, J. *et al.* The role of oxygen supply in islet transplantation. *Transplant Proc* **24**, 2925-2929 (1992).
179 Opara, A., Jost, A., Dagogo-Jack, S. & Opara, E. C. Islet cell encapsulation - Application in diabetes treatment. *Exp Biol Med (Maywood)* **246**, 2570-2578 (2021). https://doi.org/10.1177/15353702211040503
180 Krishnan, R., Alexander, M., Robles, L., Foster, C. E. & Lakey, J. R. T. Islet and stem cell encapsulation for clinical transplantation. *The review of diabetic studies : RDS* **11**, 84-101 (2014). https://doi.org/10.1900/RDS.2014.11.84
181 Jun, Y. *et al.* Microfluidics-generated pancreatic islet microfibers for enhanced immunoprotection. *Biomaterials* **34**, 8122-8130 (2013). https://doi.org/10.1016/j.biomaterials.2013.07.079
182 Kang, A. R., Park, J. S., Ju, J., Jeong, G. S. & Lee, S. H. Vol. 35 2651-2663 (Elsevier, 2014).
183 Basta, G., Montanucci, P. & Calafiore, R. Microencapsulation of cells and molecular therapy of type 1 diabetes mellitus: The actual state and future perspectives between promise and progress. *J Diabetes Investig* **12**, 301-309 (2021). https://doi.org/10.1111/jdi.13372
184 Van Deijnen, J. H., Van Suylichem, P. T., Wolters, G. H. & Van Schilfgaarde, R. Distribution of collagens type I, type III and type V in the pancreas of rat, dog, pig and man. *Cell Tissue Res* **277**, 115-121 (1994). https://doi.org/10.1007/BF00303087

185 Riopel, M. & Wang, R. Collagen matrix support of pancreatic islet survival and function. *Front Biosci (Landmark Ed)* **19**, 77-90 (2014). https://doi.org/10.2741/4196
186 Xu, Y. *et al.* Normative Pancreatic Stiffness Levels and Related Influences Established by Magnetic Resonance Elastography in Volunteers. *J Magn Reson Imaging* **52**, 448-458 (2020). https://doi.org/10.1002/jmri.27052
187 Shi, Y., Glaser, K. J., Venkatesh, S. K., Ben-Abraham, E. I. & Ehman, R. L. Feasibility of using 3D MR elastography to determine pancreatic stiffness in healthy volunteers. *J Magn Reson Imaging* **41**, 369-375 (2015). https://doi.org/10.1002/jmri.24572
188 Ledo, A. M., Vining, K. H., Alonso, M. J., Garcia-Fuentes, M. & Mooney, D. J. Extracellular matrix mechanics regulate transfection and SOX9-directed differentiation of mesenchymal stem cells. *Acta Biomater* **110**, 153-163 (2020). https://doi.org/10.1016/j.actbio.2020.04.027
189 Lv, H. *et al.* Biomaterial stiffness determines stem cell fate. *Life Sci* **178**, 42-48 (2017). https://doi.org/10.1016/j.lfs.2017.04.014
190 De Vos, P., De Haan, B. & Van Schilfgaarde, R. Effect of the alginate composition on the biocompatibility of alginate-polylysine microcapsules. *Biomaterials* **18**, 273-278 (1997). https://doi.org/10.1016/S0142-9612(96)00135-4
191 Xiao, Z. *et al.* Microfluidic Production of Zwitterion Coating Microcapsules with Low Foreign Body Reactions for Improved Islet Transplantation. *Small* **18**, e2202596 (2022). https://doi.org/10.1002/smll.202202596
192 Luo, Z. *et al.* A novel insulin delivery system by beta cells encapsulated in microcapsules. *Front Chem* **10**, 1104979 (2022). https://doi.org/10.3389/fchem.2022.1104979
193 Li, H. *et al.* A novel bioartificial pancreas fabricated via islets microencapsulation in anti-adhesive core-shell microgels and macroencapsulation in a hydrogel scaffold prevascularized in vivo. *Bioact Mater* **27**, 362-376 (2023). https://doi.org/10.1016/j.bioactmat.2023.04.011
194 Köllmer, M., Appel, A. A., Somo, S. I. & Brey, E. M. Long-term function of alginate-encapsulated islets. *Tissue Engineering Part B: Reviews* **22**, 34-46 (2016).
195 Samsonchi, Z. *et al.* Transplantation of Islet-Containing microcapsules modified with constitutional isomers of sulfated alginate in diabetic mice to mitigate fibrosis for Long-term glycemic control. *Chemical Engineering Journal* **432**, 134298 (2022).
196 van Schilfgaarde, R. & de Vos, P. Factors influencing the properties and performance of microcapsules for immunoprotection of pancreatic islets. *J Mol Med (Berl)* **77**, 199-205 (1999). https://doi.org/10.1007/s001090050336
197 Paredes Juarez, G. A., Spasojevic, M., Faas, M. M. & de Vos, P. Immunological and technical considerations in application of alginate-based microencapsulation systems. *Front Bioeng Biotechnol* **2**, 26 (2014). https://doi.org/10.3389/fbioe.2014.00026

198 Huang, L. *et al.* Regulation of Blood Glucose Using Islets Encapsulated in a Melanin-Modified Immune-Shielding Hydrogel. *ACS Appl Mater Interfaces* **13**, 12877-12887 (2021). https://doi.org/10.1021/acsami.0c23010
199 Wilcox, G. Insulin and insulin resistance. *Clin Biochem Rev* **26**, 19-39 (2005).
200 Janeway, C., Travers, P., Walport, M. & Shlomchik, M. J. *Immunobiology: the immune system in health and disease*. Vol. 2 (Garland Pub. New York, 2001).
201 Helmy, A. *et al.* Microdialysis of cytokines: methodological considerations, scanning electron microscopy, and determination of relative recovery. *J Neurotrauma* **26**, 549-561 (2009). https://doi.org/10.1089/neu.2008.0719
202 Ashimova, A., Yegorov, S., Negmetzhanov, B. & Hortelano, G. Cell Encapsulation Within Alginate Microcapsules: Immunological Challenges and Outlook. *Front Bioeng Biotechnol* **7**, 380 (2019). https://doi.org/10.3389/fbioe.2019.00380
203 Barkai, U., Rotem, A. & de Vos, P. Survival of encapsulated islets: More than a membrane story. *World J Transplant* **6**, 69-90 (2016). https://doi.org/10.5500/wjt.v6.i1.69
204 Szegedy, C. *et al.* 1-9.
205 Ren, S., He, K., Girshick, R. & Sun, J. 91-99.
206 Wu, X., Lin, M., Li, Y., Zhao, X. & Yan, F. Effects of DMEM and RPMI 1640 on the biological behavior of dog periosteum-derived cells. *Cytotechnology* **59**, 103-111 (2009). https://doi.org/10.1007/s10616-009-9200-5
207 Corbin, K. L. *et al.* A Practical Guide to Rodent Islet Isolation and Assessment Revisited. *Biol Proced Online* **23**, 7 (2021). https://doi.org/10.1186/s12575-021-00143-x
208 Williams, S. J. *et al.* Reduction of diffusion barriers in isolated rat islets improves survival, but not insulin secretion or transplantation outcome. *Organogenesis* **6**, 115-124 (2010). https://doi.org/10.4161/org.6.2.10373
209 Todorov, I. *et al.* Quantitative assessment of beta-cell apoptosis and cell composition of isolated, undisrupted human islets by laser scanning cytometry. *Transplantation* **90**, 836-842 (2010). https://doi.org/10.1097/TP.0b013e3181f1db5d
210 Lee, J. H. *et al.* Protection from beta-cell apoptosis by inhibition of TGF-beta/Smad3 signaling. *Cell Death Dis* **11**, 184 (2020). https://doi.org/10.1038/s41419-020-2365-8
211 Lakshmanan, I. & Batra, S. K. Protocol for apoptosis assay by flow cytometry using annexin V staining method. *Bio-protocol* **3**, e374-e374 (2013).
212 Stokes, R. A. *et al.* Transplantation sites for human and murine islets. *Diabetologia* **60**, 1961-1971 (2017).
213 Jaroch, D. B. *et al.* Mouse and human islets survive and function after coating by biosilicification. *American Journal of Physiology-Endocrinology and Metabolism* **305**, E1230-E1240 (2013).
214 Llacua, L. A., Hoek, A., de Haan, B. J. & de Vos, P. Collagen type VI interaction improves human islet survival in immunoisolating microcapsules

for treatment of diabetes. *Islets* **10**, 60-68 (2018). https://doi.org/10.1080/19382014.2017.1420449

215 Antoine, E. E., Vlachos, P. P. & Rylander, M. N. Review of collagen I hydrogels for bioengineered tissue microenvironments: characterization of mechanics, structure, and transport. *Tissue Engineering Part B: Reviews* **20**, 683-696 (2014).

216 Coradin, T., Wang, K., Law, T. & Trichet, L. Type I collagen-fibrin mixed hydrogels: preparation, properties and biomedical applications. *Gels* **6**, 36 (2020).

217 Hu, T. & Lo, A. C. Y. Collagen-Alginate Composite Hydrogel: Application in Tissue Engineering and Biomedical Sciences. *Polymers (Basel)* **13** (2021). https://doi.org/10.3390/polym13111852

218 Llacua, A., de Haan, B. J., Smink, S. A. & de Vos, P. Extracellular matrix components supporting human islet function in alginate-based immunoprotective microcapsules for treatment of diabetes. *J Biomed Mater Res A* **104**, 1788-1796 (2016). https://doi.org/10.1002/jbm.a.35706

219 O'Sullivan, E. S., Vegas, A., Anderson, D. G. & Weir, G. C. Islets transplanted in immunoisolation devices: a review of the progress and the challenges that remain. *Endocr Rev* **32**, 827-844 (2011). https://doi.org/10.1210/er.2010-0026

220 Zhang, D. *et al.* Dealing with the foreign-body response to implanted biomaterials: strategies and applications of new materials. *Advanced Functional Materials* **31**, 2007226 (2021).

221 Balabiyev, A. *et al.* Fibrin polymer on the surface of biomaterial implants drives the foreign body reaction. *Biomaterials* **277**, 121087 (2021). https://doi.org/10.1016/j.biomaterials.2021.121087

222 Ye, N. *et al.* A multi-omic approach reveals utility of CD45 expression in prognosis and novel target discovery. *Front Genet* **13**, 928328 (2022). https://doi.org/10.3389/fgene.2022.928328

223 Kruse, B. *et al.* CD4(+) T cell-induced inflammatory cell death controls immune-evasive tumours. *Nature* **618**, 1033-1040 (2023). https://doi.org/10.1038/s41586-023-06199-x

224 Komatsu, H., Kandeel, F. & Mullen, Y. Impact of Oxygen on Pancreatic Islet Survival. *Pancreas* **47**, 533-543 (2018). https://doi.org/10.1097/MPA.0000000000001050

225 Bottino, R. *et al.* Response of human islets to isolation stress and the effect of antioxidant treatment. *Diabetes* **53**, 2559-2568 (2004). https://doi.org/10.2337/diabetes.53.10.2559

226 Oh, J. Y. *et al.* The Outcomes and Quality of Pancreatic Islet Cells Isolated from Surgical Specimens for Research on Diabetes Mellitus. *Cells* **11** (2022). https://doi.org/10.3390/cells11152335

227 Eguchi, N. *et al.* Anti-Oxidative Therapy in Islet Cell Transplantation. *Antioxidants (Basel)* **11** (2022). https://doi.org/10.3390/antiox11061038

228 Kim, M. J., Lee, Y., Jon, S. & Lee, D. Y. PEGylated bilirubin nanoparticle as an anti-oxidative and anti-inflammatory demulcent in pancreatic islet

xenotransplantation. *Biomaterials* **133**, 242-252 (2017). https://doi.org/10.1016/J.BIOMATERIALS.2017.04.029

229 Adin, C. A. Bilirubin as a therapeutic molecule: challenges and opportunities. *Antioxidants* **10**, 1536 (2021).

230 Chen, Z. *et al.* Bilirubin Nanomedicines for the Treatment of Reactive Oxygen Species (ROS)-Mediated Diseases. *Mol Pharm* **17**, 2260-2274 (2020). https://doi.org/10.1021/acs.molpharmaceut.0c00337

231 Zhu, H. Q. *et al.* Pretreatment with bilirubin protects islet against oxidative injury during isolation and purification. *Transplant Proc* **43**, 1810-1814 (2011). https://doi.org/10.1016/j.transproceed.2010.12.058

232 Yao, Q. *et al.* Pharmacological actions and therapeutic potentials of bilirubin in islet transplantation for the treatment of diabetes. *Pharmacol Res* **145**, 104256 (2019). https://doi.org/10.1016/j.phrs.2019.104256

233 Srimal, R. & Dhawan, B. Pharmacology of diferuloyl methane (curcumin), a non-steroidal anti-inflammatory agent. *Journal of pharmacy and pharmacology* **25**, 447-452 (1973).

234 Amoli, M. M., Mousavizadeh, R., Sorouri, R., Rahmani, M. & Larijani, B. Curcumin inhibits in vitro MCP-1 release from mouse pancreatic islets. *Transplant Proc* **38**, 3035-3038 (2006). https://doi.org/10.1016/j.transproceed.2006.08.172

235 Kim, S., Jang, H., Oh, M., Lee, J. & Kang, K. in *Transplantation Proceedings.* 2847-2853 (Elsevier).

236 Kanitkar, M. & Bhonde, R. R. Curcumin treatment enhances islet recovery by induction of heat shock response proteins, Hsp70 and heme oxygenase-1, during cryopreservation. *Life Sci* **82**, 182-189 (2008). https://doi.org/10.1016/j.lfs.2007.10.026

237 Han, J., Oh, J., Ihm, S. H. & Lee, M. Peptide micelle-mediated curcumin delivery for protection of islet beta-cells under hypoxia. *J Drug Target* **24**, 618-623 (2016). https://doi.org/10.3109/1061186X.2015.1132220

238 Ganugula, R. *et al.* Nano-curcumin safely prevents streptozotocin-induced inflammation and apoptosis in pancreatic beta cells for effective management of Type 1 diabetes mellitus. *Br J Pharmacol* **174**, 2074-2084 (2017). https://doi.org/10.1111/bph.13816

239 Rocha, C. V., Goncalves, V., da Silva, M. C., Banobre-Lopez, M. & Gallo, J. PLGA-Based Composites for Various Biomedical Applications. *Int J Mol Sci* **23** (2022). https://doi.org/10.3390/ijms23042034

240 Alsaab, H. O. *et al.* PLGA-Based Nanomedicine: History of Advancement and Development in Clinical Applications of Multiple Diseases. *Pharmaceutics* **14** (2022). https://doi.org/10.3390/pharmaceutics14122728

241 Lü, J.-M. *et al.* Current advances in research and clinical applications of PLGA-based nanotechnology. *Expert review of molecular diagnostics* **9**, 325-341 (2009).

242 Budhian, A., Siegel, S. J. & Winey, K. I. Controlling the in vitro release profiles for a system of haloperidol-loaded PLGA nanoparticles. *Int J Pharm* **346**, 151-159 (2008). https://doi.org/10.1016/j.ijpharm.2007.06.011

243 Yu, J., Qiu, H., Yin, S., Wang, H. & Li, Y. Polymeric Drug Delivery System Based on Pluronics for Cancer Treatment. *Molecules* **26** (2021). https://doi.org/10.3390/molecules26123610
244 Russo, E. & Villa, C. Poloxamer Hydrogels for Biomedical Applications. *Pharmaceutics* **11** (2019). https://doi.org/10.3390/pharmaceutics11120671
245 Li, M. *et al.* Pluronic F127 coating performance on PLGA nanoparticles: Enhanced flocculation and instability. *Colloids Surf B Biointerfaces* **226**, 113328 (2023). https://doi.org/10.1016/j.colsurfb.2023.113328
246 Menon, J. U. *et al.* Effects of surfactants on the properties of PLGA nanoparticles. *J Biomed Mater Res A* **100**, 1998-2005 (2012). https://doi.org/10.1002/jbm.a.34040
247 Basak, R. & Bandyopadhyay, R. Encapsulation of hydrophobic drugs in Pluronic F127 micelles: effects of drug hydrophobicity, solution temperature, and pH. *Langmuir* **29**, 4350-4356 (2013). https://doi.org/10.1021/la304836e
248 Wang, H. *et al.* Hyaluronic acid-decorated dual responsive nanoparticles of Pluronic F127, PLGA, and chitosan for targeted co-delivery of doxorubicin and irinotecan to eliminate cancer stem-like cells. *Biomaterials* **72**, 74-89 (2015). https://doi.org/10.1016/j.biomaterials.2015.08.048
249 Wang, Y., Li, P. & Kong, L. Chitosan-modified PLGA nanoparticles with versatile surface for improved drug delivery. *AAPS PharmSciTech* **14**, 585-592 (2013). https://doi.org/10.1208/s12249-013-9943-3
250 Lu, B., Lv, X. & Le, Y. Chitosan-Modified PLGA Nanoparticles for Control-Released Drug Delivery. *Polymers (Basel)* **11** (2019). https://doi.org/10.3390/polym11020304
251 Aranaz, I. *et al.* Chitosan: An Overview of Its Properties and Applications. *Polymers (Basel)* **13** (2021). https://doi.org/10.3390/polym13193256
252 Wang, J. J. *et al.* Recent advances of chitosan nanoparticles as drug carriers. *International journal of nanomedicine* **6**, 765-774 (2011). https://doi.org/10.2147/IJN.S17296
253 McCall, R. L. & Sirianni, R. W. PLGA nanoparticles formed by single-or double-emulsion with vitamin E-TPGS. *JoVE (Journal of Visualized Experiments)*, e51015 (2013).
254 Aibani, N., Rai, R., Patel, P., Cuddihy, G. & Wasan, E. K. Chitosan Nanoparticles at the Biological Interface: Implications for Drug Delivery. *Pharmaceutics* **13** (2021). https://doi.org/10.3390/pharmaceutics13101686
255 Uragami, T. *Material science of chitin and chitosan*. (Springer, 2006).
256 Reed, R. G. Kinetics of bilirubin binding to bovine serum albumin and the effects of palmitate. *J Biol Chem* **252**, 7483-7487 (1977).
257 Lee, K.-S. & Gartner, L. M. Spectrophotometric Characteristics of Bilirubin. *Pediatric Research* **10**, 782-788 (1976). https://doi.org/10.1203/00006450-197609000-00004
258 Panyam, J., Zhou, W. Z., Prabha, S., Sahoo, S. K. & Labhasetwar, V. Rapid endo-lysosomal escape of poly (DL-lactide-coglycolide) nanoparticles: implications for drug and gene delivery. *The FASEB journal* **16**, 1217-1226 (2002).

259 Kim, S. M. *et al.* Co-Culture of α TC-6 Cells and β TC-1 Cells: Morphology and Function. *Endocrinology and Metabolism* **30**, 92-97 (2015).
260 Anastasiou, I. A. *et al.* Low concentrations of bisphenol A promote the activation of the mitochondrial apoptotic pathway on Beta-TC-6 cells via the generation of intracellular reactive oxygen species and mitochondrial superoxide. *Journal of Biochemical and Molecular Toxicology* **36**, e23099 (2022).
261 Yang, R. *et al.* Enhanced electrostatic interaction between chitosan-modified PLGA nanoparticle and tumor. *Int J Pharm* **371**, 142-147 (2009). https://doi.org/10.1016/j.ijpharm.2008.12.007
262 Lee, S. S., Lee, Y. B. & Oh, I. J. Cellular uptake of poly(dl-lactide-co-glycolide) nanoparticles: effects of drugs and surface characteristics of nanoparticles. *Journal of Pharmaceutical Investigation* **45**, 659-667 (2015). https://doi.org/10.1007/s40005-015-0221-0
263 He, H. *et al.* Speeding Up the Line-Scan Raman Imaging of Living Cells by Deep Convolutional Neural Network. *Anal Chem* **91**, 7070-7077 (2019). https://doi.org/10.1021/acs.analchem.8b05962
264 Cheng, X. *et al.* A novel integrated PCA and FLD method on hyperspectral image feature extraction for cucumber chilling damage inspection. *Transactions of the ASAE* **47**, 1313-1320 (2004).
265 Wang, D., Ali, M., Cobau, J. & Tao, Y. in *2021 ASABE Annual International Virtual Meeting.* 1 (American Society of Agricultural and Biological Engineers).
266 Choudhary, K. *et al.* Recent advances and applications of deep learning methods in materials science. *npj Computational Materials* **8**, 59 (2022).
267 Li, S. *et al.* An on-chip, multichannel droplet sorter using standing surface acoustic waves. *Anal Chem* **85**, 5468-5474 (2013). https://doi.org/10.1021/ac400548d
268 Ding, X. *et al.* On-chip manipulation of single microparticles, cells, and organisms using surface acoustic waves. *Proceedings of the National Academy of Sciences of the United States of America* **109**, 11105-11109 (2012). https://doi.org/10.1073/pnas.1209288109
269 Villa, C. *et al.* Effects of composition of alginate-polyethylene glycol microcapsules and transplant site on encapsulated islet graft outcomes in mice. *Transplantation* **101**, 1025 (2017).
270 Chen, X. *et al.* The epididymal fat pad as a transplant site for minimal islet mass. *Transplantation* **84**, 122-125 (2007).
271 Zhang, Q. *et al.* Islet Encapsulation: New Developments for the Treatment of Type 1 Diabetes. *Front Immunol* **13**, 869984 (2022). https://doi.org/10.3389/fimmu.2022.869984
272 Ding, Y., Bushell, A. & Wood, K. J. Mesenchymal stem-cell immunosuppressive capabilities: therapeutic implications in islet transplantation. *Transplantation* **89**, 270-273 (2010). https://doi.org/10.1097/TP.0b013e3181c6ffbe

273 Shrestha, M. *et al.* Immunomodulation effect of mesenchymal stem cells in islet transplantation. *Biomed Pharmacother* **142**, 112042 (2021). https://doi.org/10.1016/j.biopha.2021.112042
274 Sakata, N., Yoshimatsu, G. & Kodama, S. White adipose tissue as a site for islet transplantation. *Transplantology* **1**, 55-70 (2020).
275 Rahman, M. Magnetic Resonance Imaging and Iron-oxide Nanoparticles in the era of Personalized Medicine. *Nanotheranostics* **7**, 424-449 (2023). https://doi.org/10.7150/ntno.86467
276 Juang, J. H. *et al.* Magnetic resonance imaging of mouse islet grafts labeled with novel chitosan-coated superparamagnetic iron oxide nanoparticles. *PLoS One* **8**, e62626 (2013). https://doi.org/10.1371/journal.pone.0062626
277 Jung, M. J. *et al.* MRI of transplanted surface-labeled pancreatic islets with heparinized superparamagnetic iron oxide nanoparticles. *Biomaterials* **32**, 9391-9400 (2011). https://doi.org/10.1016/j.biomaterials.2011.08.070
278 Chen, W., Shu, Z., Gao, D. & Shen, A. Q. Sensing and Sensibility: Single-Islet-based Quality Control Assay of Cryopreserved Pancreatic Islets with Functionalized Hydrogel Microcapsules. *Advanced Healthcare Materials* **5**, 223-231 (2016). https://doi.org/10.1002/adhm.201500515
279 Zhang, W., Yang, G., Zhang, A., Xu, L. X. & He, X. Preferential vitrification of water in small alginate microcapsules significantly augments cell cryopreservation by vitrification. *Biomedical Microdevices* **12**, 89-96 (2010). https://doi.org/10.1007/s10544-009-9363-z
280 Huang, H. *et al.* Alginate Hydrogel Microencapsulation Inhibits Devitrification and Enables Large-Volume Low-CPA Cell Vitrification. *Advanced Functional Materials* **25**, 6839-6850 (2015). https://doi.org/10.1002/adfm.201503047